The chemical composition of the He-enriched sdO-star HD 127493

Bachelorarbeit aus der Physik

Vorgelegt von
Matti Dorsch
08. 08. 2017

Dr. Karl Remeis Sternwarte Bamberg
Friedrich-Alexander-Universität Erlangen-Nürnberg

Betreuer:
Prof. Dr. Ulrich Heber
Dr. Marilyn Latour

Abstract

Hot subluminous stars come in two flavors: sdO and sdB stars. All of them display peculiar helium abundances; they are either deficient or enriched in helium. The vast majority of sdB stars are helium deficient, while the helium enrichment of the small group of He-sdBs is mostly quite moderate, their atmospheres are of mixed H/He composition. A different pattern emerges for sdO stars. Their majority has atmospheres dominated by helium with hydrogen being a trace element only and, therefore, are termed He-sdO. Helium-poor sdOs exist too, though at lower numbers. Mixed composition objects, however, are rare among sdO stars. The bright sdO star HD 127493 is known to be of mixed H/He composition and excellent spectra at both optical and ultraviolet wavelengths are available. UV spectra play a key role as they give access to many chemical species that do not show spectral lines in the optical. This encouraged a quantitative spectral analysis of this prototypical mixed H/He composition sdO star, which was performed as a part of this work. Its abundance pattern will allow us to study a potential link between the He-deficient sdO stars and the strongly helium dominated ones (He-sdOs) as well as that between the mixed H/He composition He-sdOs and their analogs amongst the He-sdBs.

As a part of this work, atmospheric parameters for HD 127493 were determined in addition to the abundance of C, N, O, Si, S, Fe and Ni in the atmosphere. A comparison between the parallax distance measured by Hipparcos and the derived spectroscopic distance indicate that the measured atmospheric parameters are realistic. As a sideline, a number of different atmospheric models that were used for the spectroscopic analysis were compared and analyzed in detail.

Contents

1 Introduction

1.1 Motivation

So-called subdwarf stars are less luminous than main-sequence (MS) dwarf stars, like the Sun, for the same temperature. In a brightness-color diagram (Hertzsprung-Russell Diagram, see Fig. 1), they are located below the main sequence (hence the name).

There are two classes of subdwarfs: hot subdwarfs and cool subdwarfs. Cool subdwarfs have surface temperatures from $\sim 10\,000$ K down to ~ 1000 K, respectively corresponding to spectral types between G (like the Sun) and M. Like MS stars, these low-mass stars are burning hydrogen in their cores. However, their lower metallicitiy (abundance of elements heavier than helium) leads to less absorption lines. Hence, more continuum flux is radiated from deeper and hotter layers of stellar atmosphere and their spectrum falls closer overall to that of a blackbody, so these subdwarfs appear bluer than MS dwarfs (Jao et al. 2008). In a HRD, they are located left of the low-temperature MS. Being low-metallicity stars, they are classified as population II stars, which were formed at an earlier time in the universe, before metals were enriched by supernova explosions. Most of them are found in the galactic halo and globular clusters.

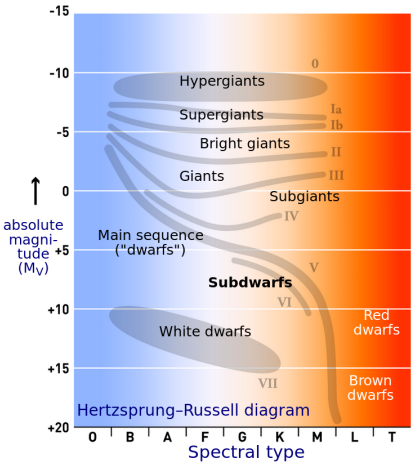

Figure 1. Hertzsprung-Russell diagram showing the classification of cool subdwarfs[1].

These stars have little in common with the subject of this work: hot subdwarfs. Hot subdwarf stars are of spectral classes O and B, with temperatures higher than 20 000 K, but masses typically below 1 $M_\odot$. In contrast to cool subdwarfs, hot subdwarfs are in a late evolutionary stage. They are helium core burning stars with a very thin hydrogen layer. Stars enter the red giant phase after hydrogen burning stops in the core. Helium from the hydrogen-burning shell accumulates in the core. At the tip of the red giant branch (RGB), their helium cores become hot and dense enough to ignite fusion in a flash, which causes them to leave the red giant phase, still having massive hydrogen envelopes that sustain H-shell burning. Hot subdwarf stars can be described as the cores of these red giant stars that have lost their hydrogen envelope. Although there are several proposed processes that can explain the removal of the hydrogen envelope and the creation of a hot subdwarf, the evolution of many types of hot subdwarf stars remains unclear.

Being a typical product of stellar evolution, subdwarf O - and B - stars (or short: sdOs and sdBs) play an important role in understanding the spectra of old stellar populations (like elliptical galaxies and globular clusters). Hot subdwarf stars have about the same brightness as the Sun in the visual but are $10 - 100$ times more luminous in total. Because of their high effective temperatures their flux maximum is in the UV range, making them bright stars in this spectral range. Normally, UV light is associated with young star forming regions that do not exist in old stellar populations, so the discovery of an excess in the UV spectrum of early-type galaxies below 2500 Å by Code & Welch (1979) came as a big surprise and lead to numerous speculations about its origin.

[1] `https://en.wikipedia.org/wiki/File:HR-diag-no-text-2.svg`, under CC BY-SA 3.0

Because of their high luminosity in the UV and number density in old stellar populations, subdwarf stars might be major contributors to this so-called UV-upturn (Yi & Yoon 2004). An improved understanding of hot subdwarf evolution will provide more precise predictions of their abundance in old stellar populations and in that way improve our understanding of these populations as well as galaxy evolution in general.

In addition, hot subdwarf stars in close orbits with massive white dwarfs are interesting as potential progenitors of thermonuclear supernovae of type Ia (Webbink 1984; Geier et al. 2016). A white dwarf explodes in a SN Ia after reaching a critical mass, which can be triggered by mass accretion from a close companion, e.g. a hot subdwarf. Because of their consistent peak luminosity, SN Ia are important as standard candles for long distance measurements and therefore also for cosmology.

1.2 Subdwarf O and B stars

1.2.1 Characteristics

A solar mass star evolves to a red giant after hydrogen has been converted to helium in the core of the star. During the ascent on the RGB, energy is produced by a H-burning shell and helium fusion ignites in electron-degenerate conditions, which leads to a flash. In the following helium core burning phase, the hydrogen burning in the shell slows down but does not stop completely. As a result, the star begins to contract as its surface reaches higher temperatures while maintaining a roughly constant bolometric luminosity: the horizontal branch phase (see Fig. 2). Before the blue end of the horizontal branch is reached (the BHB), the helium core is exhausted and the star evolves towards the asymptotic giant branch. In contrast to BHB - stars, the hydrogen shell of hot subdwarfs is too thin to sustain fusion after the RGB phase and they do not evolve towards another giant phase when their helium core is depleted. Instead, they evolve directly along the white-dwarf cooling sequence.

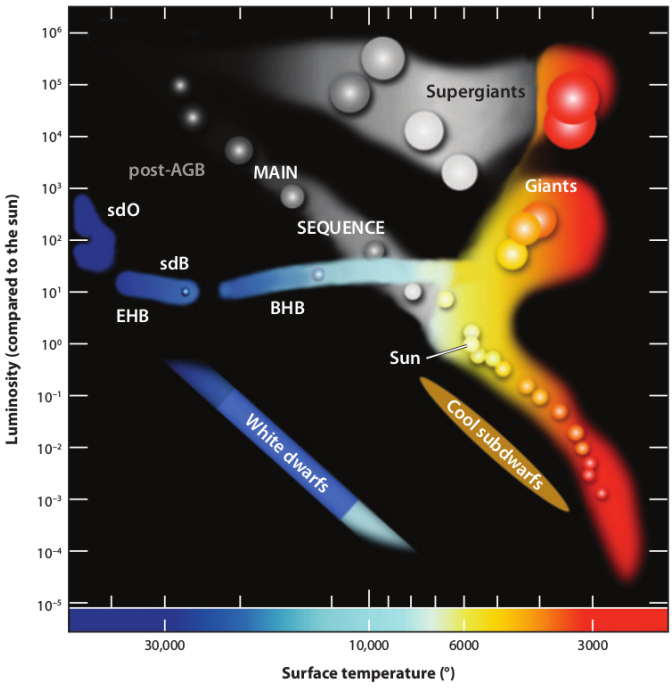

Figure 2. Hertzsprung-Russell diagram: Hot subdwarfs populate a region below the upper main-sequence O- and B-stars and above the white dwarf cooling sequence (Heber 2009).

According to their temperature, they are divided into two spectral types: hotter sdOs with surface temperatures above 40 000 K and cooler sdBs between 20 000 and 40 000 K. Although their name suggests otherwise, they have little in common with regular main-sequence O and B stars. While main-sequence O and B stars have masses of several 10s to 100s of Suns, these dwarf stars typically have a canonical mass of about $0.5\,M_{\odot}$. Their radius is also smaller than that of the Sun ($0.1 - 0.3\,R_{\odot}$), resulting in lower luminosities − they are dim compared to main-sequence O and B stars.

B-type subdwarf stars are located at higher temperatures than the blue end of the horizontal branch and form the so-called extreme horizontal branch (EHB). About half of them are found in close binary systems (Copperwheat et al. 2011) with mostly white dwarfs and low-mass main-sequence stars as companions (Geier et al. 2015). These binaries can be so close that they would fit inside a red giant star's envelope, specifically the sdB's red giant progenitor. When this happens while the progenitor has already evolved close to the tip of the red-giant branch (RGB), the orbital separation shrinks due to friction and enough energy is transferred to the hydrogen shell to eventually expel it (Han et al. 2002). This is called the common-envelope ejection scenario. A close binary consisting of a sdB (the core of the RGB-star) with a very thin hydrogen envelope and its companion is formed. Even though sdB stars are core helium burning, their thin atmosphere is usually dominated by hydrogen ($> 99\%$ by number fraction), and observed spectra show strong H Balmer lines. They form a spectroscopically homogeneous group, although some rare helium-rich sdB stars (He-sdBs) exist as well.

Most O-type subdwarf stars also occupy a small region in the HRD at higher temperatures and luminosities than sdB stars. However, there is significant variance in the abundance of helium and metals in their atmospheres. The spectra of most sdOs are dominated by helium. These stars cluster in a narrow region at temperatures between 40 000 K and 50 000 K and surface gravities between $\log g = 5.5$ and 6.0 in cgs units (Stroeer et al. 2007). Hydrogen-rich sdO stars with a chemical composition similar to sdB stars exist in a wide surface temperature range ($40 - 80$ kK). Intermediate He-sdOs with helium abundances by number between 10% and 90% form an even smaller group. From the observation of metal lines in the visual range, Stroeer et al. (2007) have identified sdO subclasses depending on the amount of carbon and nitrogen in the atmosphere. All helium-deficient sdOs in their sample were also deficient in carbon and nitrogen (type 0), while all He-sdOs were either enriched in only nitrogen (type N), carbon (type C), or both (type CN). Stars classified as sdOs are generally not as homogeneous as sdB-type stars and are believed to represent stages of several distinct post-RGB evolutionary paths. In addition, many sdO stars may have evolved beyond core helium burning.

1.2.2 Formation and Evolution

In contrast to sdB systems, less sdO stars reside in binary systems (Napiwotzki 2008). Common envelope ejection can therefore not be regarded as the only common origin. In the scope of this work, we will focus on possible He-sdO formation scenarios. Two of the most promising explanations are the late hot flasher scenario and the merger of two low-mass helium white dwarfs.

Late Hot Flasher In the standard stellar evolution, low-mass stars violently begin burning He in their core when they reach the end of the red giant branch. If the star has lost enough mass during the red giant phase (e.g. through strong stellar winds), this first He-flash occurs while the star's envelope is already less massive and more compact. The star will then deviate from the standard evolution. Miller Bertolami et al. (2008) have computed models for the stellar evolution starting from the tip of the RGB, where they artificially increased the mass-loss. From evolutionary models of sdB stars Lanz et al. (2004) have classified three cases of the hot-flasher scenario. In addition to a canonical (post-)RGB evolutionary sequence, the corresponding hot flasher evolutionary tracks are shown in a effective temperature − luminosity diagram in Fig. 3.

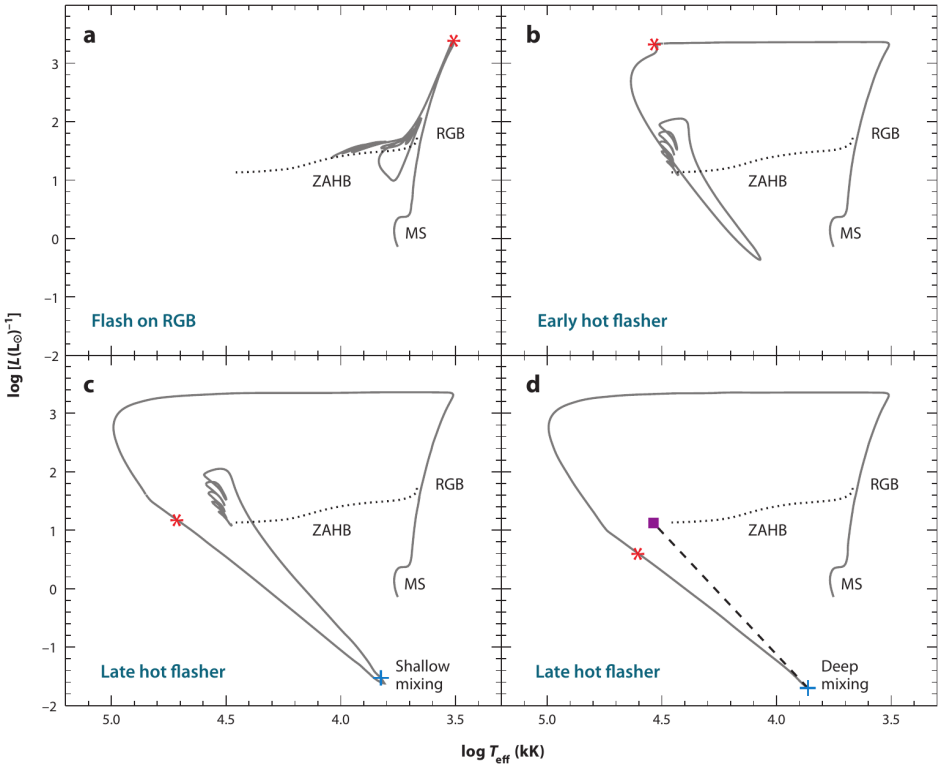

Figure 3. Hot flasher evolutionary tracks from Lanz et al. (2004). The evolution from the main sequence to the zero age horizontal branch (ZAHB) is shown for four cases of mass-loss on the RGB branch. The red asterisk indicates the position of the peak helium flash. The secondary hydrogen-flash, which occurs in the late flasher cases, is marked by a blue plus sign. The model calculations in panel (d) were stopped at the onset of deep mixing, and a ZAHB model (filled square) was then computed assuming a helium- and carbon-rich envelope composition. The evolution during this phase is shown schematically by the dashed line.

An early helium core-flash (Fig. 3b), when the post-RGB star is evolving to higher temperatures with constant luminosity (decreasing in radius) was proposed to be able to produce hot subdwarf B stars with standard H-rich envelopes. The first He-flash occurs off-center, but not close enough to the surface of the star to mix helium with the hydrogen envelope. Subsequent weaker helium-flashes then continue inward closer to the core ("loops" close to the ZAHB in Fig. 3b,c) and the convection zone never reaches the surface, which remains hydrogen-rich. The result of a later helium-flash, which happens when the post-RGB star is already descending on the white dwarf cooling sequence, strongly depends on the mixing strength of the hydrogen-shell with the helium core.

In a shallow-mixing case (Fig. 3c), a helium-rich surface could be achieved by mixing helium from the core into the envelope and atmosphere, as observed for example in He-sdBs. In a deep-mixing case (Fig. 3d), the hydrogen-envelope could reach deep into the convective core, where most of the hydrogen would be burned violently through the CNO-cycle (so-called secondary hydrogen-flash). In this process, most of the hydrogen would be lost and an extremely He-rich hot subdwarf B or O star can be created. Since the computation of these models is very complex and mixing effects in the interior of the star as well as in the atmosphere have to be considered, it is difficult to predict the exact chemical abundances on the surface of the modeled star. Miller Bertolami et al. (2008) have created models for both late-flasher cases for a set of starting metallicities and masses on the zero age main sequence (ZAMS), and provide theoretical prediction of the observable effective temperature, surface gravity and chemical abundances. They find that all considered hot flasher scenarios lead to a subdwarf with a carbon enriched surface.

White dwarf merger Hot subdwarfs can also be created as the result of the merger of two low-mass helium white dwarfs (He-WD). White dwarfs in a close binary lose orbital angular momentum due to the emission of gravitational waves. When the Roche limit is reached, they merge into a single core He-burning star. The initial distance between both stars as well as their masses determine the subsequent evolution. Zhang & Jeffery (2012) showed that these mergers can reproduce the observed distribution of He-rich sdO-stars. They modeled the merging processes of two helium white dwarfs with equal masses, ranging from 0.25 to 0.4 $M_{\odot}$. This represents an extreme case, since in reality one star is more massive and mass is transferred from the less massive (and therefore bigger) secondary WD to the more massive one. Three cases with fixed accretion rates were considered. In a slow accretion case, the material from the less massive WD is accreted in a cold disk in the order of million years. If the mass transfer is faster (within minutes), no disk is created and the secondary WD forms a hot corona around the primary WD instead. They also computed models for a composite merger, where most mass is transferred instantly via a corona, but 10% are left to form a cold accretion disk. All of the models can create He-rich subdwarfs. In the slow-merger case, the post-merger surface convection zone is not deep enough to dredge up material from fusion in deeper shells and the surface chemical abundances are the same as the accreted secondary WD. For that reason, carbon from the 3α He-burning process is not enriched, while nitrogen from the RGB CNO-cycle H-burning is enriched (C and O are depleted accordingly). For all fast-merger cases, the envelope is fully convective at the end of the merger and the surface is enriched in carbon, oxygen and neon but depleted in nitrogen. The composite merger scenario predicts that the stars are N-rich if the final mass is $\leq 0.65\,M_{\odot}$, but C-rich stars if it is larger. The most important part of the evolutionary tracks of all three cases is shown in a effective surface temperature ($T_{\rm eff}$) − surface gravity ($\log g$) diagram in Fig. 4. The loops in the tracks are a result of subsequent helium-flashes after the first He-flash.

Two He-WDs are not the only merger combination that can create hot subdwarfs. Zhang et al. (2017) have found that the merger of a He-WD with a low-mass main-sequence star can result in the formation of a star with an intermediately helium-rich surface (like HD 127493). In this case, the immediate result of the merger resembles a RGB-type star with H-shell burning but a somewhat cooler core. Similar to the hot flasher scenarios, this star will undergo a He-flash if its core is massive (and hot) enough. Here, the main difference to the hot flasher scenarios is that no artificial mass-loss is required to remove the envelope of the RGB star since it is already thinner.

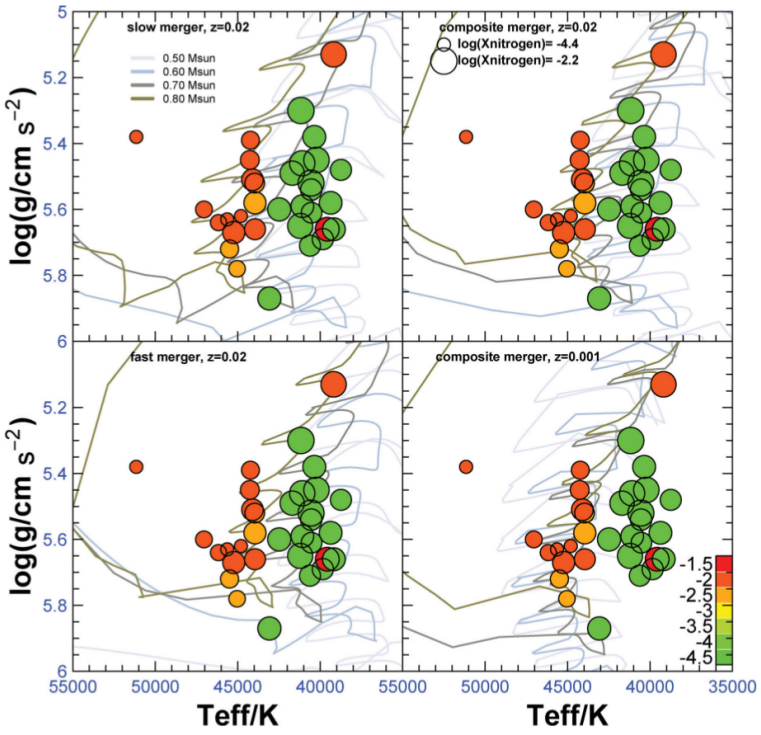

Figure 4. Double He-WD merger tracks from Zhang & Jeffery (2012). The color of the tracks corresponds to masses of $0.5 - 0.8\,M_\odot$ from grey to dark. The colored circles are He-sdOs from Hirsch (2009), including HD 127493 at $\log g = 5.60$ and $T_{\rm eff} = 42484\,$K. The abundance of carbon is indicated by the circle color, red being higher than green. The nitrogen abundance is higher for bigger circles.

Another big difference to the hot flasher scenario is that the first off-center He-flash occurs closer to the surface of the star. Therefore, early hot flasher HeWD+MS merger remnants can mix helium to the surface. From this stage, the helium abundance at the surface may decrease again as heavier elements diffuse downwards. In this way, the He-rich subdwarfs could evolve to become intermediately He-rich and eventually reach the helium-burning main sequence with an atmosphere dominated by hydrogen in short timescales of about 5 Myr (Zhang et al. 2017, Fig. 5).

Evolutionary tracks for post-RGB stars can be computed with stellar evolution codes like `MESA` (Paxton et al. 2011; Schindler et al. 2015). To date, these codes do not fully consider the very thin atmosphere of the modeled star that is responsible for the observed spectrum. In addition, diffusion and mixing processes in the atmosphere have a big impact on the measured element abundance. This is also hard to model, since the timescales for the evolution in the interior of the star (e.g. the convective core and the envelope) are much longer than the mixing timescales. An important diffusion process in the atmosphere is **gravitational settling**: heavy elements sink to the bottom of the photosphere while hydrogen rises to the top. This effect is very important since it can change the observed spectrum on short timescales from helium- to hydrogen-rich. Another important effect is **radiative levitation**, which mostly affects the heavier metals (like iron and nickel). Heavy metals have many absorption lines in the UV range, where the flux of hot subdwarfs is high. Therefore, they gain momentum and rise to the upper layers of the atmosphere, opposing gravitational settling, where they contribute absorption lines to the observed spectrum. Both of these effects are suppressed in the presence of rapid rotation or strong stellar wind. However, the star considered in this work, HD 127493, is a slow rotator, so both of these effects may be important as an explanation for the observed chemical composition.

In addition, Groth et al. (1985) have found a thin **surface convection zone** due to the partial ionization of helium in He-sdOs that, according to Unglaub (2010), may also affect the abundance of chemical elements on the surface. Due to the complexity of these mixing processes, reliable quantitative predictions of surface abundances are presently not possible (Miller Bertolami et al. 2008).

1.2.3 HD 127493

HD 127493 is a bright He-sdO star without any known companion. It was among the first hot subdwarfs to be discovered (Münch & Greenstein 1955, p. 11). Its parallax was measured as 5.43 ± 1.21 mas by the Hipparcos satellite (van Leeuwen 2007), which corresponds to a distance of 184^{+53}_{-34} pc. Because of its brightness, it has been analyzed multiple times. Simon (1982) found it to have an effective surface temperature of $T_{\rm eff} = 42\,500$ K, a surface gravity of $\log g = 5.25$ and a moderately enriched helium abundance of $\log N({\rm He})/N({\rm H}) = 0.60$. These measurements were redone by Hirsch (2009), who not only confirmed these results, but also found the star's atmosphere to be nitrogen enhanced while only showing weak signs of carbon. This implies that large amounts of nitrogen from the CNO cycle have reached the surface whereas only little carbon is seen (Bauer & Husfeld 1995). Most hot subdwarf stars are either He-rich or He-weak while few show a N(He)/N(H) ratio around one (Fontaine et al. 2014; Heber 2016, Fig. 4). Combined with its brightness and CNO abundances, this makes HD 127493 an interesting target for a more detailed analysis. This analysis would help understanding the potential link between He-enriched and -deficient sdO stars, as well as to sdB stars with a similar helium abundance. In order to link the measured abundances to the evolution of the star, predicted element abundances from improved evolutionary calculations are required. These models can then be tested using the measured rotation, atmospheric parameters and element abundances. The aim of this work is to derive the chemical abundance of all relevant metals (like carbon, nitrogen, oxygen, silicon, sulfur, iron and nickel) in the star's photosphere, as well as to revisit the atmospheric parameters measured by Hirsch (2009) and Simon (1982) with more sophisticated model atmospheres. To this end, archived high quality UV spectra of HD 127493 taken with the HST GHRS instrument will be analyzed for the first time.

1.3 Model Atmospheres

Atmospheric parameters, as well as chemical abundances can not be derived directly from observed spectra. In order to determine atmospheric parameters and chemical abundances from a spectrum, is has to be compared with synthetic spectra for which these parameters have been specified. For this, an extensive grid (= library) of synthetic spectra is required. Synthetic spectra first require realistic models of the stellar atmosphere, that is the temperature and density stratification close to the surface of the star. A single model is calculated for a given effective temperature and surface gravity. The third important atmospheric parameter is the helium abundance, which has a considerable impact on the temperature and density stratification. Therefore, the grids of atmospheric models have to vary in three parameters ("3-D"). Additional chemical elements are then included in order to derive their abundance in the atmosphere.

In the following section, only the basic concepts of model atmosphere computation will be discussed. It is largely based on chapters 4 in Hirsch (2009) and Irrgang (2014), as well as Haas (1997).

Photons from the stellar core transport energy towards the outer layers of the star over the course of many interactions until they reach the thin stellar atmosphere close to the surface. Since temperatures in the atmosphere are considerably lower than in deeper regions of the star, collisional processes with electrons dominate over radiative processes. Consequently, the populations of energy levels and ionization stages of atoms are coupled to the density and temperature of the local plasma. In this case, it is safe to assume local thermal equilibrium (LTE), meaning that in any small volume element, atomic processes occur at the same rate as their inverse process (e.g. absorption and emission of photons). This allows computing the energy level occupation numbers using the Boltzmann excitation formula and ionization fractions using the Saha ionization equation directly from the local electron density and temperature. Since the ionization equilibrium strongly depends on the temperature, the relative strength of He II to He I or hydrogen lines can be used to measure the temperature. For more details on these LTE equations see for example Irrgang (2014). The particle velocity distribution can be assumed to be Maxwellian even without the LTE approximation, since the mean free path for electrons is considerably shorter than for photons.

There are four main processes through which photons interact with the plasma (Carroll & Ostlie 2007, pp. 244). They determine the rough shape of the observed spectrum by deviations from black-body radiation, either by additional continuum or line opacity. At high electron densities and high temperatures, the scattering by free electrons, which results only in a change of direction, is a dominant process. This process is an important source of continuum opacity in O- and early (= hot) B-type stars (Gray 2005, p. 163). Another process that contributes to the continuum opacity is free-free absorption: when a free electron passes close to an ion, it may absorb (or emit) a photon and gain (or loose) kinetic energy. If the photon energy is higher than the binding energy of bound electrons, they can also ionize atoms (photo-ionization). Photons are absorbed continuously according to the photo-ionization cross section, thus adding to the continuum opacity. Spectral lines are created by bound-bound interactions. Photons excite shell electrons to higher energy levels. Excited electrons can then return to a lower energy level ("relax"), emitting a photon with the energy difference between both levels in the process. This interaction is only possible if the energy of the initial photon matches the energy difference between two levels. Most spectral lines visible in observed spectra are absorption lines created by this process. Since the energy difference between energy levels in a given atom is different depending on the available energy levels and electrons in the shell, these lines are characteristic for each element and ionization stage.

The shape of these lines is influenced by a number of broadening effects, which in turn depend on the temperature and density of the local plasma. Therefore, the line profile can be used to measure atmospheric parameters in addition to element abundance. There are three basic types of broadening effects of importance for hot stars: natural broadening, pressure broadening and thermal Doppler broadening (Gray 2005, p. 231). They will be briefly addressed in the following.

Exited electrons in an atom de-excite on short timescales Δt, which according to Heisenberg's uncertainty principle results in an uncertainty in the energy of $\Delta E \gtrsim \hbar/\Delta t$. This natural broadening is very small compared to other broadening effects since the typical de-excitation time $\Delta t \approx 10^{-8}\,\mathrm{s}$ corresponds to only $\Delta\lambda \approx 10^{-4}\,\text{Å}$ (Carroll & Ostlie 2007, p. 268).

Collisions of excited atoms with other particles can perturb the emission process in numerous ways (which can not be discussed comprehensively as a part of this *short*

introduction). For example, they can change the atomic level energies due to their electric fields (Stark effect) or reduce the characteristic emission time to a scale where natural broadening becomes important. Depending on the pressure in the plasma, these interactions occur more or less often. As a result, spectral lines are broadened by a Lorentzian profile. Hydrogen and helium II lines are strongly broadened by the linear Stark effect and are thus very useful for measuring the density in line-forming regions, which is closely related to the star's surface gravity.

Because of thermal motion with respect to the observer, photon wavelengths are blue- or redshifted due to the Doppler effect. The cumulative broadening from this is given by the Maxwell velocity distribution, which is Gaussian and depends on the local temperature. Spectral lines are consequently shaped to resemble a Gaussian profile.

There are also some non-thermal Doppler broadening effects. The most important effect in this context is stellar rotation: spectral lines created by material rotating towards the observer are blue-shifted. We observe the spectrum averaged over the stellar disk and therefore the line profiles are smeared. This allows determining the projected rotational velocity ($v_{\mathrm{rot}} \sin i$) of the star's surface from line broadening additional to the broadening included in the model atmosphere. To determine the true rotational velocity, the inclination of the rotational axis i with respect to the observer has to be known (e.g. from an eclipsing binary system). In the atmospheric model codes there is usually also a fixed parameter that adds Gaussian broadening to account for micro-turbulent velocity.

To model the observed spectral lines, all of the mentioned effects have to be convolved with the instrumental profile of the instrument used for observation. This results in a so-called Voigt line profile, the combination of a Lorentzian and Gaussian profile.

All in all, the calculation of a model atmosphere is a very complex problem. In order to limit computation time, approximations have to be made. For example, it can be assumed that every volume element in the atmosphere emits just as much flux as it absorbs ("radiative equilibrium"). Other important approximations are the homogeneous abundance of chemical elements in the atmosphere and plane geometry. The latter is valid since the star's radius is much bigger than the extension of the atmosphere. This allows treating the atmosphere as parallel layers at discrete depth points. The atmosphere is also assumed to be static in time: its weight and gas (and radiative) pressure cancel out ("hydrostatic equilibrium").

For hot sdO stars, like HD 127493, atomic processes such as excitation and ionization in atoms is not only determined by the local parameters of the plasma, but also by the non-local radiation field. At high temperatures and moderate surface gravities, the mean free path for photons is long enough that photons from deep layers of the star can disturb the local thermal equilibrium (LTE). In this case the atmosphere can no longer be treated as consisting of independent local volume elements, and the influence of the radiation field has to be considered. Models that include these computationally expensive deviations from the local thermal equilibrium are termed non-LTE models. Napiwotzki (1997) have shown that non-LTE effects become important very quickly in sdB stars when their temperature approaches 40 000 K. Since sdO stars like HD 127493 are not only hotter but some also have lower surface gravities, non-LTE effects become even more pronounced. The LTE approximation is then replaced by the more general assumption of statistical equilibrium, where the population of all energy levels is assumed to be constant in time. In this case the detailed rate equations follow and have to be calculated instead of using the Maxwell, Boltzmann and Saha equations (again see Irrgang (2014) for more details).

2 Methods

2.1 Observations

2.1.1 Optical spectroscopy

FEROS FEROS is an echelle spectrograph mounted at the MPG/ESO-2.20m telescope operated by the European Southern Observatory (ESO) in La Silla. It features a high resolution of R $\approx$ 48000 (Kaufer et al. 1999). Its spectral range from $\sim$3600 Å to $\sim$9200 Å includes all Balmer lines as well as many He I, He II and metal lines. For more detailed information on FEROS, see Kaufer et al. (1999). The three available spectra of HD 127493 were co-added to achieve a high signal-to-noise ratio (S/N) of $\gtrsim$100 in the 4000 − 6000 Å range. Towards both ends of the spectral range, the S/N decreases drastically, reaching a value of S/N $\sim$ 15 at 8000 Å. The range above 7000 Å is also affected by strong telluric lines (from earth's atmosphere), rendering it almost useless for quantitative spectral analysis.

2.1.2 UV spectroscopy

Observations of the UV spectral range are very useful for HD 127493, since this is the range where the star's flux is highest. Spectra in this range can also be used to determine the abundance of many metals, since there are strong resonance lines as well as a large number of iron and nickel lines. There is some contamination by strong interstellar absorption but only at short wavelengths. These interstellar lines are rather well known because they are frequently seen in the UV spectra and since they are also usually formed by low ionization stages, they could be easily identified and ignored. All UV spectra used are listed in Table 1.

Telescope	Dataset	Wavelength Range (Å)	Exp. Time (s)	Obs. Date
HST GHRS	Z2H60107T	1222.6 − 1258.8	462	19/01/96
	Z2H60109T	1254.9 − 1291.0	462	19/01/96
	Z2H6010BT	1285.6 − 1321.6	462	19/01/96
	Z2H6010DT	1317.7 − 1353.6	462	19/01/96
	Z2H6010FT	1349.7 − 1385.5	516	19/01/96
	Z2H6010HT	1383.0 − 1418.8	598	19/01/96
	Z2H6010JT	1414.9 − 1450.5	516	19/01/96
	Z2H6010LT	1532.5 − 1567.7	652	19/01/96
	Z2H6010OT	1623.2 − 1658.1	462	19/01/96
	Z2H6010QT	1713.0 − 1747.6	462	19/01/96
IUE	SWP04860	1150.0 − 1980.0	3000	05/04/79
	SWP07695	1150.0 − 1980.0	4500	19/01/80
	SWP08276	1150.0 − 1980.0	3930	16/03/80

Table 1. UV sprectra retrieved from the MAST archive[2].

IUE Three archival spectra from the International Ultraviolet Explorer (IUE) were stacked to increase the S/N ratio. They continuously cover the range from 1150 to 1980 Å with a resolution of about 0.15 Å. This range includes additional C III resonance and N III lines that are important for the abundance analysis.

GHRS HD 127493 has been observed with the Goddard High-Resolution Spectrograph (GHRS) mounted on the Hubble Space Telescope (HST). The publicly available spectra cover a range from 1225 to 1745 Å with a resolution of about 0.06 Å (medium resolution mode, R ≈ 25000). The signal to noise ratio is very good, especially around the center of the covered range. However, it is hard to measure since all wavelength ranges are crowded with metal lines. The quality of this spectrum is much higher than that from IUE with respect to both S/N and spectral resolution.

2.2 TLUSTY/SYNSPEC

The model atmospheres used in this work were computed using the public codes TLUSTY and SYNSPEC developed by Hubeny (1988). Over the last decades TLUSTY has been extended by Hubeny & Lanz (1995) to include new iteration methods as well as more options for the treatment of iron and nickel (amongst many other changes). A detailed description is given in the form of a user manual, see Hubeny & Lanz (2006).

TLUSTY computes model atmospheres for a specified effective temperature and surface gravity (in the form of $\log g$). For each chemical element included in non-LTE, a model atom for each ionization stage has to be provided. These model atoms consist of many energy levels, allowing many different transitions and therefore many absorption lines. To ensure convergence of the models, additional elements where included in the model atmosphere one at a time. It is important to note that TLUSTY assumes homogeneous chemical composition, that is does not include any stratification of element abundance in the atmosphere, unlike predicted by some evolutionary models (Miller Bertolami et al. 2008, their Fig. 7).

The code is capable of computing both LTE and non-LTE models. While deviations from LTE do not affect every line equally, it is still necessary to include the populations of all elements in non-LTE.

Line-blanketing describes the effect that metals, most importantly iron and nickel because of their huge number of line transitions, absorb photons in the UV range, strongly affecting the temperature stratification in the atmosphere. In order to include iron and nickel in non-LTE, TLUSTY uses the opacity sampling (OS) method in which the line opacity is sampled on a grid of wavelength points for each included element.

The output model atmosphere consists of the population of each energy level as well as the atmosphere's temperature and density structure. This model is then used as an input for SYNSPEC, which computes the final synthetic spectrum for a given model.

SYNSPEC is a general spectrum synthesis program for calculating the emergent spectrum from a model atmosphere. In addition to the input atmospheric model it uses a line list to find lines that contribute to the total opacity. It then solves the radiative transfer equation for wavelengths in a given range. For an in-depth description of SYNSPEC see Hubeny & Lanz (2000).

2.3 SPAS

SPAS (**S**pectrum **P**lotting and **A**nalysing **S**uite) was used for fitting the observed spectra with the synthetic grid computed with TLUSTY and SYNSPEC by means of χ^2 minimization. It was developed by Hirsch (2009) and is largely based on the FITSB2 code (Napiwotzki et al. 2004).

[2]Mikulski Archive for Space Telescopes, https://archive.stsci.edu/index.html

Possible fitting parameters are the effective temperature ($T_{\rm eff}$), the surface gravity ($\log g$), the abundance of one element ($\log y$) as well as the star's radial velocity ($v_{\rm rad}$) and rotational velocity ($v_{\rm rot}$). Fitting the effective temperature, $\log g$ and $\log y$ ("3D-fit") is only possible when the grid of models includes models with different values for each of these parameters. In order to get meaningful results, the best-fit values for each considered line have to be included in the range of the model grid values. Therefore, many models are required for fitting in three dimensions.

3 Results

3.1 Radial and Rotational Velocity

The radial velocity of HD 127493 was previously determined by Hirsch (2009) to be about -16 km/s using the same FEROS spectra as used in this work. This velocity is consistent with most metal and H/He-lines in the FEROS spectra as well as most metal lines in the GHRS UV spectra. The IUE spectra show a slight systematic wavelength shift between the red and blue ends of the spectrum, and a generally higher radial velocity of about -23 km/s. Because of this, lines in the IUE spectra could not be used to further improve the radial velocity determination. In addition, many lines at all wavelength ranges show a complex structure (including blends) and can therefore not be used for fitting radial velocity in `SPAS`.

The rotational velocity of the star is also important for comparing it to evolutionary models. Stars with slower rotation than the core of the progenitor RGB star must have lost angular momentum during their evolution. This is especially hard to explain in merger scenarios. Hirsch (2009) determined the surface rotational velocity of HD 127493 to be below 10 km/s, which is again consistent with values derived in this work. This remarkably slow rotation corresponds to a rotational period of more than one day, assuming a radius of $R = 0.2\,R_\odot$. While this is a rough estimate, it should be enough to estimate the rotation timescale.

We did not find evidence for stellar wind or micro-turbulence from the available spectra and, therefore, both were not required in the atmospheric models.

3.2 Atmospheric parameters

Previous spectral analysis of HD 127493 were based on different and less sophisticated model atmospheres and synthetic spectra. For that reason it was necessary to re-determine the atmospheric parameters before embarking on the metal line spectrum. To this end, two new 3D grids were computed. Both grids include effective temperatures of 35 000, 40 000 and 45 000 K, as well as surface gravities of $\log g = 4.7$, 5.4 and 6.1. For each of these combinations, models with a helium abundance of $\log N({\rm He})/N({\rm H}) = -0.3$, $+0.3$ and $+0.9$ were computed[3].

The first grid includes nitrogen (constant mass fraction) in addition to hydrogen and helium, while a second grid was computed to include carbon and silicon as well. Abundances for these metals were derived beforehand using one-dimensional grids assuming the effective temperature and $\log g$ from Hirsch (2009).

[3]This grid is coarse and it can not be excluded that interpolation is not accurate enough. The grid would need to be extended to rule out interpolation issues (see p. 15).

Both grids were used to fit the optical FEROS spectrum, which includes many H, He I and He II lines. Since the radial velocity determined by Hirsch (2009) using the same FEROS spectra was fitting well, it was not changed. As expected, some lines were not reproduced well in the models and could consequently not be used for fitting. The selection of all lines used, as well as the global best-fit line can be seen in Figures 9 and 10. The results from a global fit of all selected lines for both grids are shown in Table 2.

	H+He+N	H+He+C+N+Si	H+He+N (Hirsch 2009)
$T_{\rm eff}$ (K)	$41\,850 \pm 70$	$41\,900 \pm 70$	$42\,484 \pm 250$
$\log g$	5.562 ± 0.016	5.561 ± 0.017	5.60 ± 0.05
$\log N({\rm He})/N({\rm H})$	0.439 ± 0.011	0.435 ± 0.010	0.62 ± 0.30
χ^2	9542.4	9351.37	

Table 2. Results from 3D-fits with purely statistical errors compared to the results of Hirsch (2009) with error estimations from spectrum-to-spectrum variations.

Both grids yield almost the same results. The determined effective temperature and $\log g$ are slightly lower ($\Delta T_{\rm eff} \approx -550$ K and $\Delta \log g \approx -0.04$) than derived by Hirsch (2009). The difference in helium abundance is larger (~ -0.2 dex), but still well within the uncertainty given by Hirsch (2009) (0.3 dex). Systematic differences between `TMAP` (the atmospheric model code used by Hirsch (2009)) and `TLUSTY` are discussed in section 3.6.2.

The model grid including also C+Si gives very similar results for every line used for determining the helium abundance. As expected, only the hydrogen and helium lines that are blended with Si lines show significant differences. For example H δ 4101.73 Å (see Fig. 5), which is blended with two strong Si IV and two N III lines, as well as He II 4686 Å (blended with N III, Si III) show differences. He I 6678 Å is also blended with two Si lines. Although all H Balmer lines are blended with He II lines, they will be referenced only by their Balmer series nomenclature since the H line component is always significantly stronger in HD 127493.

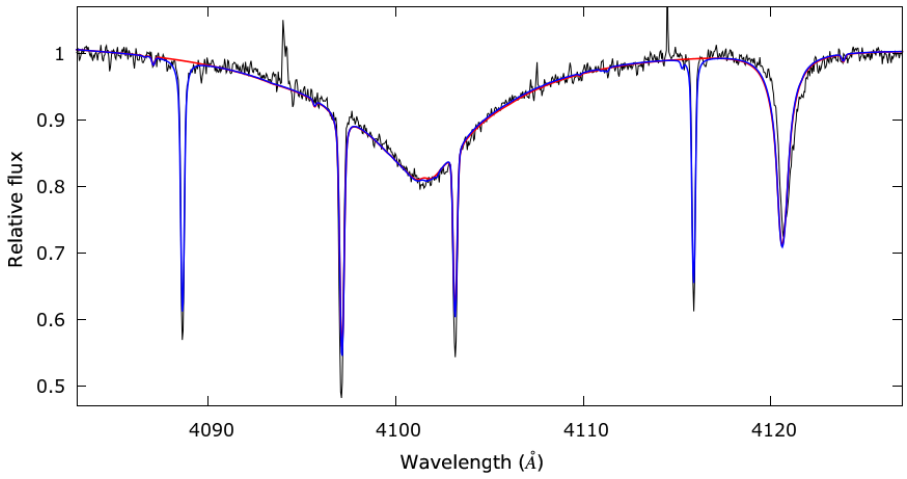

Figure 5. A detailed view of H δ and He I 4121 Å is shown: in blue the fit using models with only He+N, in red with models including also C+Si. The fit results in a helium abundance of $\log N({\rm He})/N({\rm H}) = 0.74$, which is higher than derived from most lines, $T_{\rm eff} = 41\,812$ K, and $\log g = 5.26$.

The χ^2 for both fits are mostly useful for a comparison of fit qualities and hold little information about the absolute quality of the fit, since they are not reduced and therefore strongly depend on the size of the selected range. The fit using the second grid yields a lower χ^2, indicating a somewhat better fit. This is mostly due to silicon blends in H δ, that are missing in the model only including nitrogen (as opposed to differences in temperature stratification). Because of its low abundance and very weak lines in the optical, carbon has no significant effect on the fit.

The statistical errors for these results are determined by `SPAS` using the bootstrapping method. However, the true uncertainty is dominated by systematic errors. Here, the problems and limits of the `TLUSTY` models will be discussed in addition to the equally important inaccuracies in the fitting process.

Poor Fits By fitting single lines one at time, it is possible to classify poorly fitting lines in multiple categories.

- He II lines and lines blended with He II are too weak in both model grids, while He I lines are too strong. This is a known problem in models that do not include iron and nickel. Even though no iron or nickel lines are visible in the FEROS spectra, both elements are important for modeling absorption lines even when they originate from other elements. This can be explained in part by the "line-blanketing" - effect. Iron and nickel have many strong absorption lines in the UV range and thereby reduce the outgoing UV flux. Because of flux conservation, this flux has to be re-emitted again in a more transparent region of the electromagnetic spectrum, and adds to the flux continuum level at longer wavelengths. This also affects the atmospheric temperature stratification and, therefore, the ionization balance. This effect is discussed in more detail in section 3.6.1. Of course, the ionization fraction of He II is also influenced by the effective temperature, which may be somewhat too low.

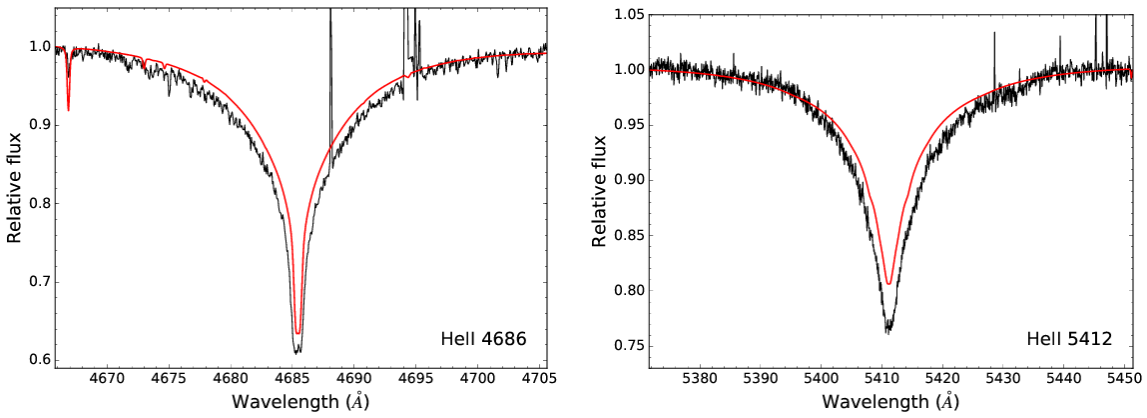

Figure 6. Detailed view of He II 4686 Å and He II 5412 Å: in red the best fit to the full set of hydrogen and helium lines is shown.

For example, He II 5412 Å and He II 4542 Å are too weak in the model (Fig. 6). Fitting these lines individually results in very high temperatures (around 50 000 K, which is outside of the range of the computed grid) and a high surface gravity.

- Some lines have insufficient broadening data, especially for the forbidden components of He I lines (see Fig. 7). This is a well-known issue (Bauer & Husfeld 1995) but since it only affects a small part of the lines, the effect on the global fit is not too large to use them for the determination of atmospheric parameters.

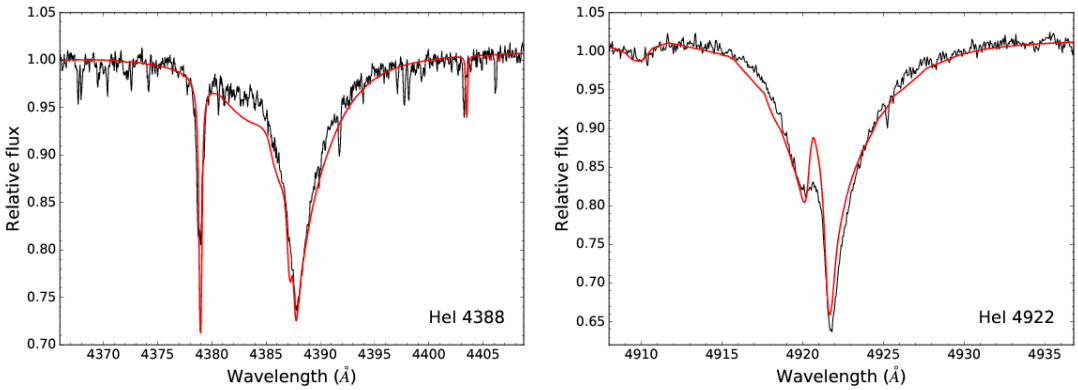

Figure 7. Detailed view of He I 4388 Å and He I 4922 Å: the forbidden components of He I 4388 Å and 4922 Å in both left wings are not reproduced well by the model spectra.

- Interpolation between model spectra in the grid can also lead to issues if the grid is too coarse. To get an arbitrary set of parameters within the grid, the flux for every wavelength point has to be interpolated between given model spectra for all parameters. In `SPAS`, this is done by fitting a function to the flux values at every single wavelength point first for all $\log N(\mathrm{He})/N(\mathrm{H})$, then all $\log g$, and finally all T_{eff} within the grid. In general, line strengths do not scale linearly with the abundance of helium, the effective temperature or $\log g$. Therefore, the fitting function is not simply linear, but a more complex so-called natural cubic spline function. This function is defined piece-wise by cubic polynomials, so that the first and second derivatives of each part-function are zero at the endpoints of the interval of interpolation.

  Since the 3D-grid only has three points each for $\log N(\mathrm{He})/N(\mathrm{H})$, $\log g$, and T_{eff}, interpolation problems are to be expected. This was tested by fitting a single synthetic model spectrum computed with the atmospheric parameters derived by Hirsch (2009) with the 3D-grid. Since the same code and settings were used for this model as for the grid, an almost perfect global fit should result in the initial parameters if the grid were fine enough.

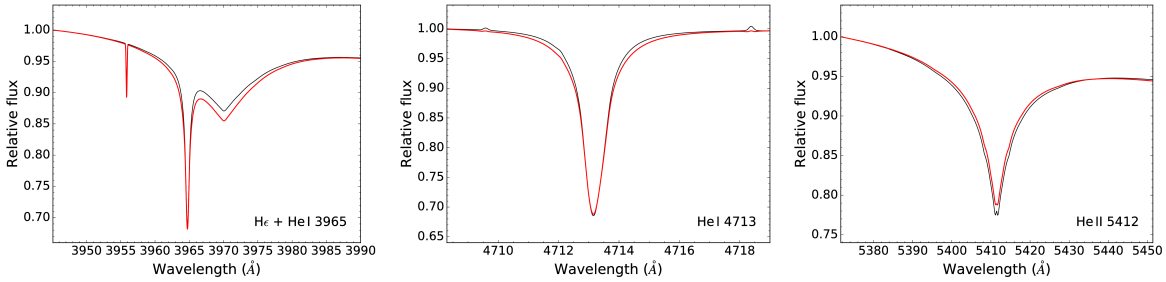

Figure 8. Detailed view of H ϵ, He I 4713 Å and He II 5412 Å showing the 3D-grid fixed (red) to the parameters of a single synthetic spectrum (black). Parameters are $T_{\mathrm{eff}} = 42484$ K, $\log g = 5.6$ and $\log N(\mathrm{He})/N(\mathrm{H}) = 0.62$. He I lines are too strong in the grid interpolation, He II lines are too weak and H ϵ lines are too strong.

Instead, there are systematic differences between H, He I and He II lines (see Fig. 8). As a result, the global fit parameters are not the same as the initial parameters used to create the synthetic spectrum. Of course, this also applies when fitting the observed spectra, so for all results derived using this coarse grid, the interpolation problem should be kept in mind. The difference in H, He I and He II line strengths in the observed spectra is a combination of this effect and the line-blanketing effect. Hence, in a next step of the analysis the grid should be extended.

Fitting process Unlike bad fitting lines, errors introduced by subjective fitting can not be simply excluded.

- In order to match the synthetic and measured spectrum, both continua have to be aligned. While this is performed automatically in `SPAS`, it often happens that the continuum location has to be adjusted manually. Especially in regions with many blends or overlapping hydrogen and helium lines, this can be very difficult and may result in large abundance changes for a single line. For example, if the continuum is placed too high, the derived abundance will also be too high. In the UV range, this is even more difficult, since there is no "true" continuum range because of line crowding.

- For each line, the wavelength range (window) has to be specified. Changing the window may affect abundance results even if the fit looks similar (even for lines without blends, e.g. He I 4471 Å, He I 4026 Å). In part, this can be explained by the importance of the spectral line wings. If a spectral line is very strong, changes in abundance will not affect the core depth but the shape of the line's wings. If these wings are cut off in the fit (for example to avoid poorly fitting metal blends), the measured abundance will change. Changing the range for very weak or badly fitting lines will also change the measured abundance since adding more points to the fit reduces the importance of the actual line to the overall χ^2 of the fit. This is especially problematic when fitting metal lines in the UV range (often to the point where even a strong line can not be used for fitting), since a certain window size is required to estimate the continuum location, but increasing it too much reduces the importance of the targeted line and includes additional poorly fitting lines. Here, one has to compromise between continuum accuracy and line strength accuracy.

- Finally, the selection of lines used for determining the helium abundance is also not fully objective. Which lines are too weak to be included in the fit? Which lines are fitting too poorly? These are choices that can not be avoided, but are of course always subjective and a matter of the experience of the scientist. This is not considered in the statistical error!

In conclusion, systematical errors certainly outweigh the statistical errors. However, it is difficult to estimate these errors and the standard deviation of individual fits can be seen as only a rough approximation for systematical errors. Stroeer et al. (2007) have estimated the size of the "true" errors by independently fitting two UVES spectra for each star in their SPY sdO sample. They find find the 1-σ-value (sample standard deviation) of this distribution of relative errors between sets of two spectra to yield global relative errors of $\Delta T_{\rm eff}/T_{\rm eff} = 0.026$, $\Delta g/g = 0.25$, and $\Delta y/y = 0.30$. Since HD 127493 is similar to some stars in this sample, it might be reasonable to adopt these numbers for HD 127493 as well.

For the atmospheric parameters found in this work, assuming these relative error would result in absolute errors: $\Delta T_{\rm eff} = 1090\,{\rm K}$, $\Delta \log g = 0.097$, and $\Delta \log y = 0.11$.
Since the derived atmospherically parameters are very similar the ones found by Simon (1982) and Hirsch (2009), it is safe to assume that the "true" values are not far off.

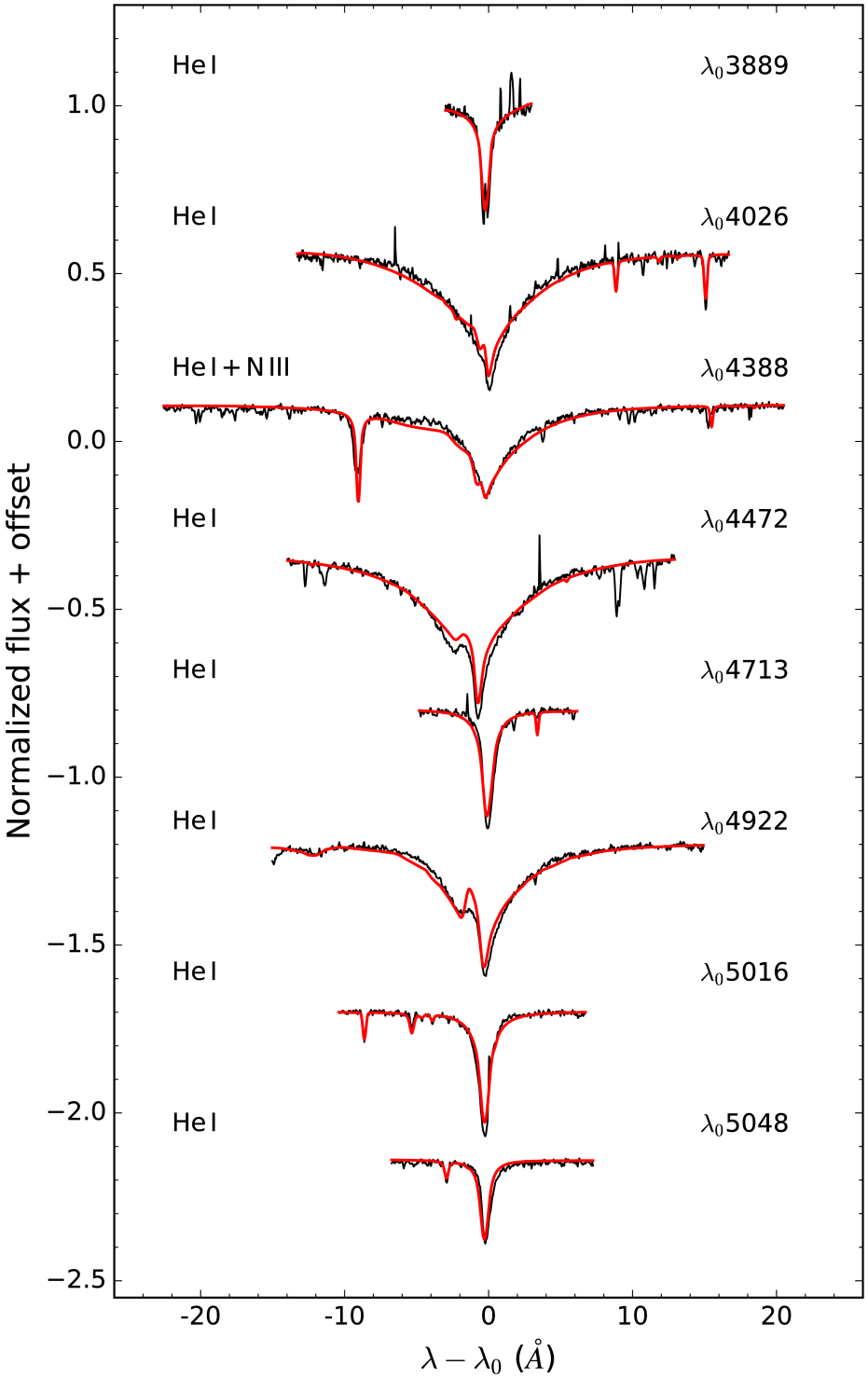

Figure 9. All lines used for fitting $\log N({\rm He})/N({\rm H})$, $\log g$, and $T_{\rm eff}$ (part 1).

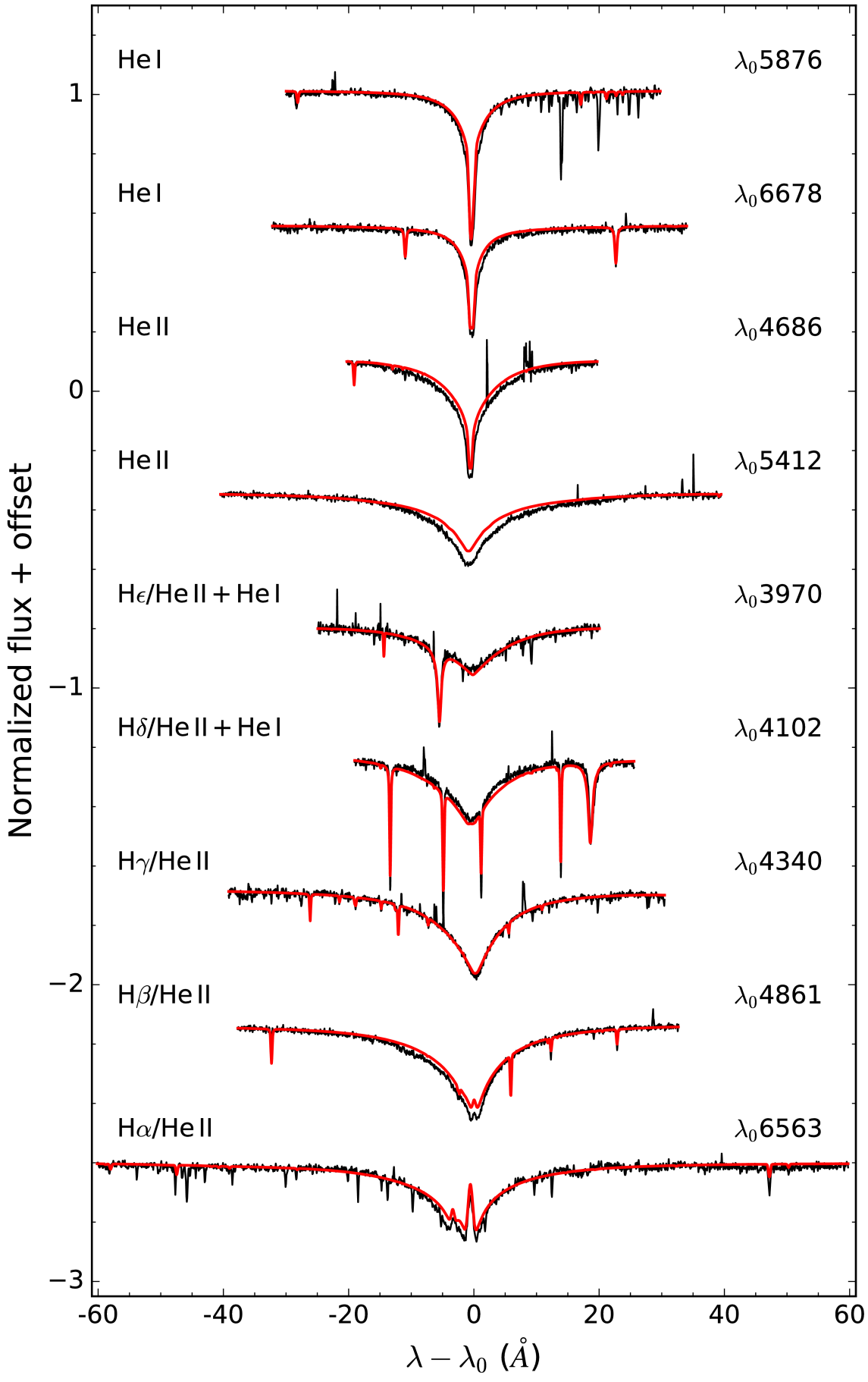

Figure 10. All lines used for fitting $\log N(\mathrm{He})/N(\mathrm{H})$, $\log g$, and T_{eff} (part 2).

3.3 Chemical Composition

The abundance of metals in the atmosphere of HD 127493 was determined using one-dimensional grids with fixed effective temperature and surface gravity for each chemical element. Since many lines are weak or display shifts in radial velocity, it was necessary to fit each line individually. The abundance of metals was determined before fitting the atmospheric parameters with a 3D-grid. Therefore, the effective temperature, surface gravity, and helium abundance were adopted from Hirsch (2009). This is a good approximation for metal lines that are not blended with hydrogen or helium lines. Most lines are consistent with a rotational velocity below 10 km/s, many even fit best with a rotational velocity of zero.

The optical FEROS spectrum is rich in nitrogen and silicon lines, most of which could be used for fitting. For fitting lines of most other elements, one has to turn to the UV range. Although this spectral range is dominated by strong iron and nickel lines, it is also very useful for determining the abundance of light metals. This is because carbon, nitrogen and silicon all have resonance lines in this range. These strong lines are created by a transition from the ground state.

In order to achieve good fits in the UV, but also for optical metal lines, fully line-blanketed non-LTE models were used. The final model includes the following ions in non-LTE: H, He I-II, C III-IV, N II-V, O II-V, Si III-IV, S III-V, Fe III-V, Ni IV-V. The most detailed model atoms available on the `TLUSTY` website[4] were used, including 877 energy levels overall. Starting from a pure H/He model, more metals were added to the model one at a time to ensure convergence. The abundance of each newly added element was determined using a fine grid of about ten models with fixed temperature and surface gravity. For the elements that have lines in the UV range only (C, O, S), iron and nickel were included first since most lines are blended with lines from these two elements. This increased the computation time of a single model to a maximum of about eight hours, so multiple models were computed in parallel. The results from this analysis are described in the next paragraphs. Errors are generally provided as standard deviation between single-line fits.

Carbon While carbon lines are barely visible in the FEROS spectra, the C IV resonance doublet at 1548 Å and 1551 Å covered by GHRS and the C III sextuplet lines at 1175 Å covered by IUE enable a robust determination of the C abundance to about 1/100th solar, consistently from lines of both ionization stages.

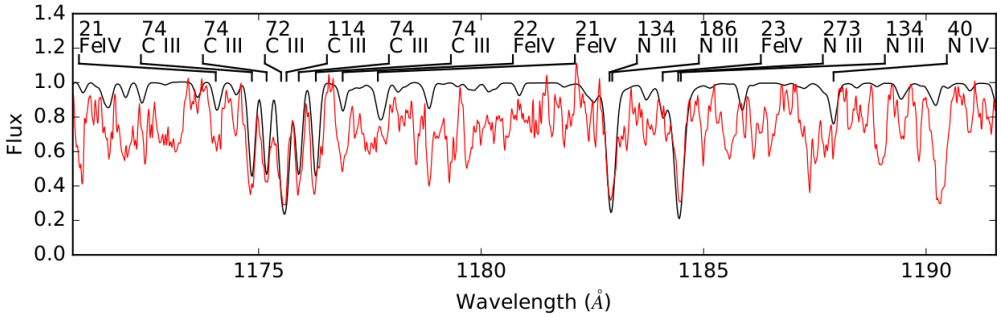

Figure 11. Best-fit model spectrum (black) compared to the IUE spectrum in red showing the C III sextuplet and N III lines. Some opacity in this short-wavelength range is missing. The line at 1190.3 Å is likely a mix of interstellar C I and Si II.

[4] `http://nova.astro.umd.edu/Tlusty2002/tlusty-frames-data.html`

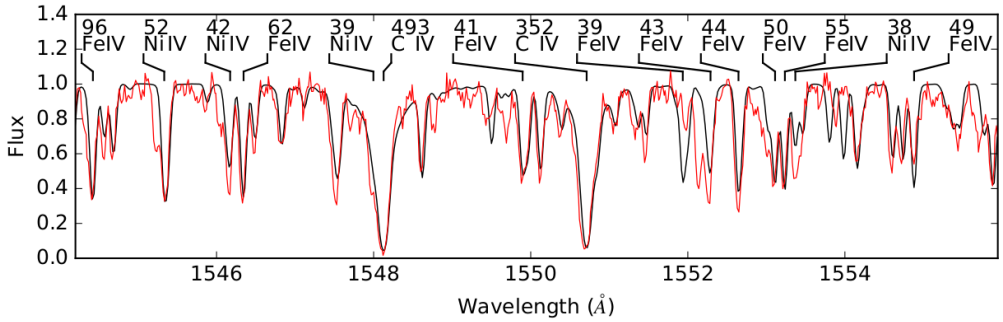

Figure 12. Best-fit model spectrum (black) compared to the GHRS spectrum in red

Figure 11 and 12 show the fully line-blanketed best-fit model in the range of the C III sextuplet and the C IV resonance doublet, respectively. The number above the line labels corresponds to the estimated line equivalent width in mÅ.

Nitrogen For the nitrogen abundance fits, many lines in the UV spectra could be used, including N V resonance lines ($\lambda\lambda 1238.8, 1242.8$), a strong N IV line ($\lambda 1718$, see Fig. 13), as well as a number of N III lines. All ionizion stages in the UV give a consistent abundance of about 7.0 ($\pm$ 2.8) times solar.

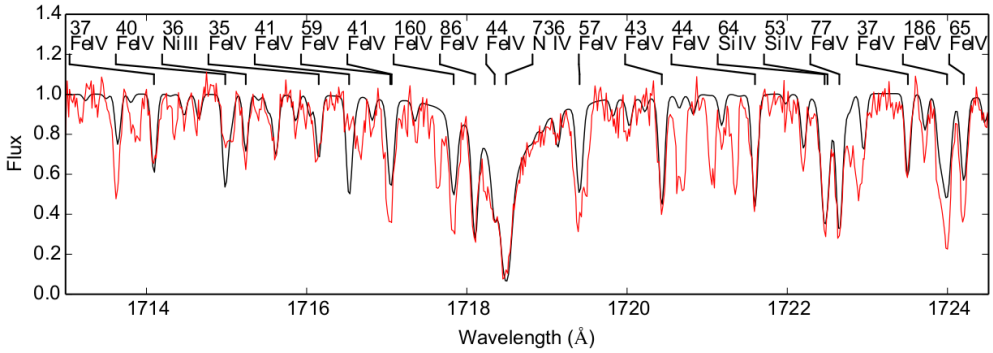

Figure 13. Best-fit model spectrum (black) compared to the GHRS spectrum (red) featuring a strong N IV line which is blended by many Fe IV lines.

The optical spectrum shows a large number of strong N III lines that could be used for fitting. N IV and II ionization stages are also present but fewer and weak in comparison (with the notable exception of N IV 4058 Å, see Fig. 14b), some of which could be used for fitting[5]. Like in the UV range, all ionization stages give a consistent abundance. This indicates that the selected model effective temperature $T_{\rm eff} = 42484$ K is reliable.

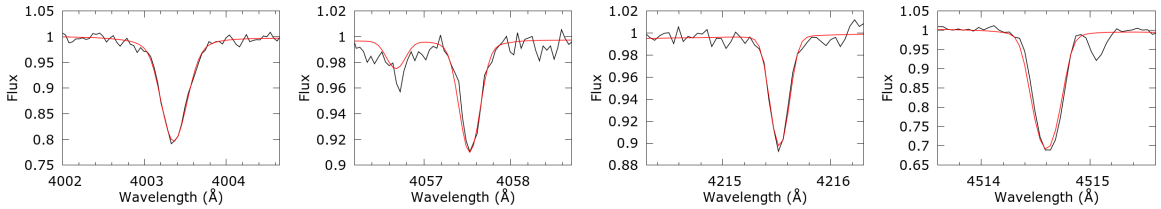

(a) N III λ4004 (b) N IV λ4058 (c) N III λ4216 (d) N III λ4515

Figure 14. Example individual fits (red) compared to the FEROS spectrum (black).

[5]Several weak N II lines could not be used for fitting, since they appear in emission in the models but are clearly in absorption in the observed spectra.

Although no iron or nickel lines are visible in the optical, it is still important to include their UV line-blanketing effect in the models. As discussed in section 3.5 and 3.6.1, line-blanketing strongly affects the atmospheric structure. For example, N II 5680 Å is weaker in models including line blanketing, while N III 4004 Å is stronger (see Fig. 15).

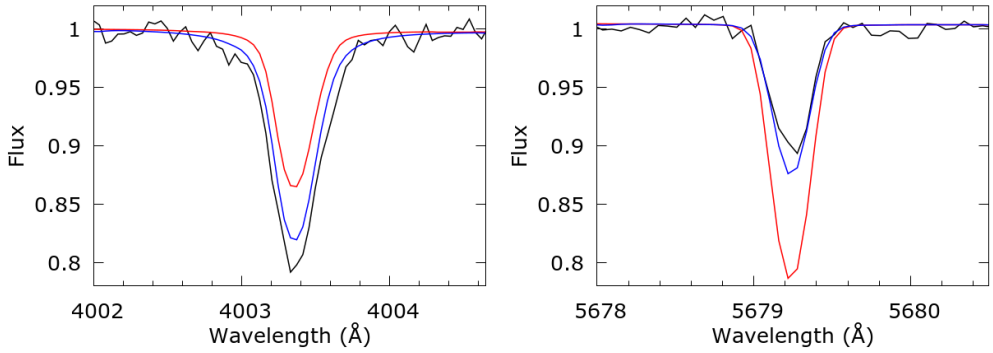

(a) N III 4004 Å (b) N II 5680 Å

Figure 15. Models with a fixed nitrogen abundance of $\log N(\mathrm{N})/N(\mathrm{H}) = -2.2$ without (red) and with line-blanketing (blue) compared to the FEROS spectrum (black).

Oxygen Both UV and visual spectra show very weak oxygen lines, which allows estimating an upper abundance limit of about $\log N(\mathrm{O})/N(\mathrm{H})) \sim -4.6$ dex, corresponding to about 1/200th of the solar value.

Silicon Like nitrogen, strong silicon lines can be seen in both UV and visual spectra. However, emission lines are not a problem. Three lines in the UV (including the Si IV resonance doublet $\lambda\lambda$1394, 1403, see Fig. 16) could be used for fitting in addition to four lines from the optical range. Both UV and optical lines give a consistent abundance of 0.8 ($\pm$ 0.3) times solar.

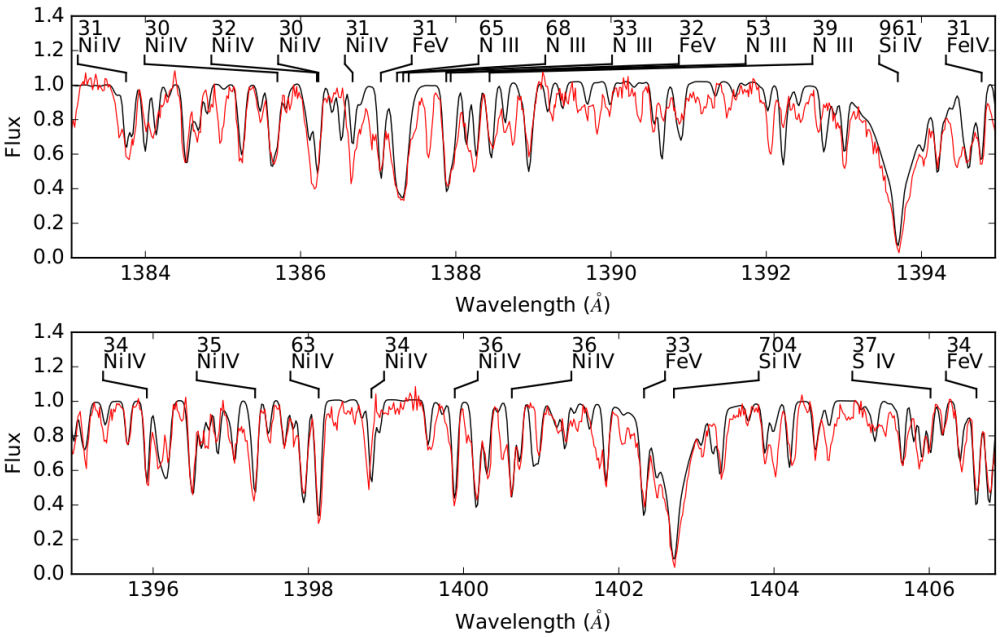

Figure 16. Best-fit model spectrum (black) compared to the GHRS spectrum (red) around the Si IV doublet. A variety of Ni IV, Fe IV and Fe V lines are indicated.

Sulfur Sulfur lines are less frequent and weaker, but using three lines in the IUE spectrum (most importantly S V 1502 Å) it was possible to derive an abundance of 0.8 (± 0.5) times solar.

Iron & Nickel The iron and nickel abundances were determined by fitting several ranges in the UV, spanning 10 to 20 Å, that show mostly iron or nickel lines. An example range used for fitting iron is shown in Fig. 17. Together, all ranges yield an average abundance of 2.4 (± 1.1) times solar for iron and 7.6 (± 2.1) times solar for nickel. While nickel also shows many strong lines in the UV (e.g. in the range below 1400 Å, see Fig. 16), it is harder to find ranges that show only nickel and no iron. The majority of nickel lines is found at wavelengths below 1450 Å, where three ranges where selected for fitting the nickel abundance (because of this, the standard deviation error on this abundance in Table 3 is likely underestimated).

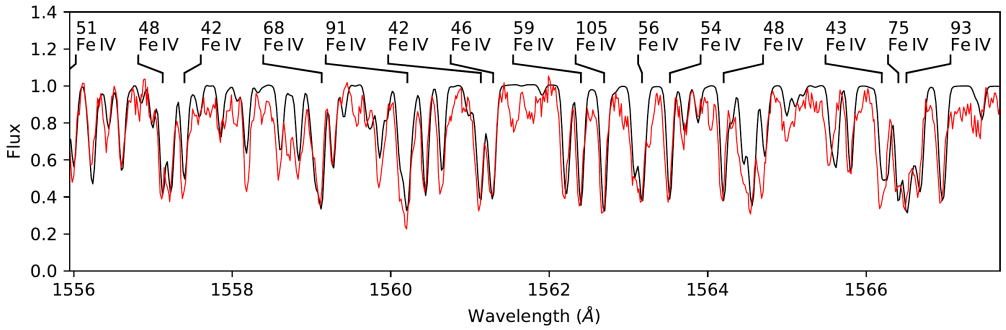

Figure 17. Section of the GHRS spectrum (red) dominated by iron lines.

Additional elements The abundance of other metals was tested by including them in LTE. The abundance of Mg, Ne and Ti seems to be low, since no additional lines in either the UV or optical range could be identified with confidence. In the UV range, no Na and Th lines could found in a quick search. The same holds for Al, Ar and Ca in the optical range. A more thorough analysis would be required to reliably constrain the abundance of these elements or even set upper limits. In addition, it might still be interesting to search for exotic elements like zirconium, strontium, yttrium or even lead, especially since some lines in the optical range are still unidentified. Jeffery et al. (2015) have found these chemical elements to be strongly enriched (compared to the Sun) in stars quite similar to HD 127493.

The results on the abundance of all metals considered are shown in Table 3. Note that the abundance *by number* ($\log \epsilon$) is always relative to the hydrogen abundance. Since the helium abundance derived by Hirsch (2009) was used to determine metal abundances, all metal abundances had to be scaled to get the same mass fraction when using the new helium abundance determined using the 3D-grids, since `TLUSTY` uses the ratio by number $N(X)/N(\mathrm{H})$ as input for the abundance of any element. Therefore, abundances of all chemical elements X are also given in mass fraction $\beta_X := \frac{N(X)\cdot A(X)}{\sum_i N(X_i)\cdot A(X_i)}$ (where A is the atomic mass number).

	H	He	C	N	O	Si	S	Fe	Ni
$\log \epsilon$	0	$+0.44^{+0.10}_{-0.12}$	$-4.62^{+0.07}_{-0.08}$	$-2.38^{+0.13}_{-0.18}$	≤ -4.62	$-3.63^{+0.12}_{-0.16}$	$-4.01^{+0.19}_{-0.34}$	$-3.20^{+0.14}_{-0.21}$	$-3.97^{+0.06}_{-0.07}$
$\log \beta_X$	$-1.08^{+0.09}_{-0.11}$	$-0.04^{+0.13}_{-0.18}$	$-4.62^{+0.11}_{-0.15}$	$-2.32^{+0.15}_{-0.23}$	≤ -4.50	$-3.26^{+0.14}_{-0.21}$	$-3.59^{+0.20}_{-0.39}$	$-2.54^{+0.16}_{-0.25}$	$-3.29^{+0.11}_{-0.14}$

Table 3. Abundance results by number $\log \epsilon := \log N_X/N_\mathrm{H}$ and mass fraction β_X.

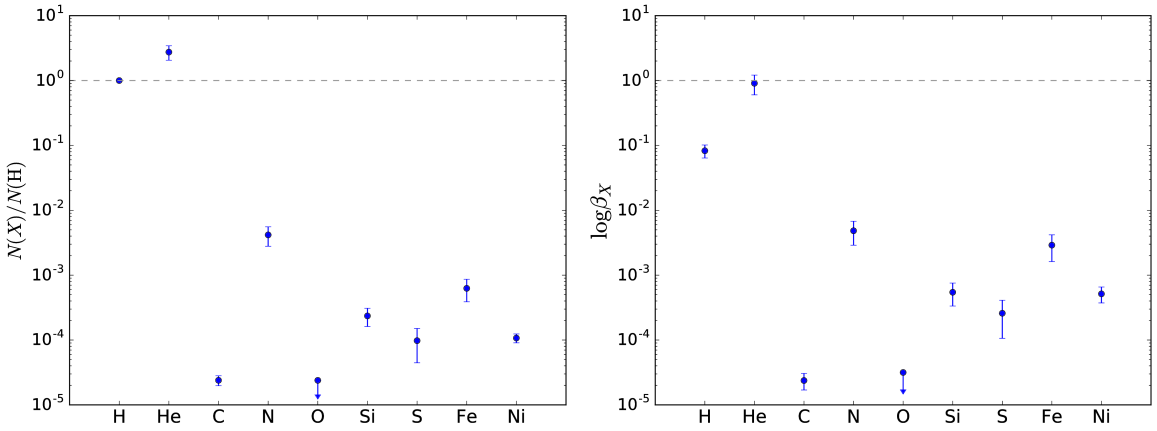

Figure 18. The chemical composition of HD 127493 by number (left) and in mass fraction (right).

As seen in the right-hand panel of Figure 18, almost 100% of the atmospheric mass of HD 127493 is given by hydrogen and helium. The errors in mass fraction are larger, since the uncertainty of the helium abundance has to be taken into account for normalization and therefore the abundance of all other elements. From the comparison to solar values (Fig. 19), HD 127493 can be categorized as an intermediate He-sdO of the N-type. Carbon and oxygen are very weak, as expected from CNO-processed material. Silicon and sulfur abundances are close to solar. Iron is enriched to about 1.5 to 3.5 times solar, while nickel is enriched to about 5 to 10 times solar. Values for the solar abundances were adopted from Asplund et al. (2009) and Scott et al. (2015b,a) for elements heavier than Ca.

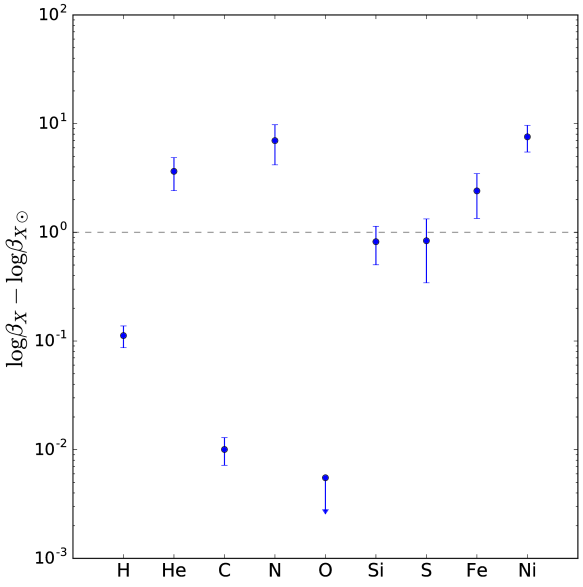

Figure 19. Metal abundance by mass fraction compared to solar values.

3.4 Parallax and specroscopic distance

Since Hipparcos parallax (and therefore distance) measurements are available for HD 127493, it is interesting to compare this value to the spectroscopic distance. The absolute $V-$magnitude (M_V) derived from a model atmosphere can be combined with the apparent $V-$magnitude (m_V) of the star to measure its distance. First, the apparent magnitude has to be corrected for interstellar dust reddening, so that it can be compared to the theoretical unreddened magnitude. Interstellar dust, containing large amounts of metals, scatters and absorbs light especially in the ultraviolet through infrared and emits photons thermally in the far-infrared (Fitzpatrick 1999). Since the dust extinction is stronger for shorter wavelengths, this leads to a reddening effect, which can be described by the difference between the observed and intrinsic color index of a star (usually the $B-V$ color): $E_{B-V} = (B-V)_{\text{observed}} - (B-V)_{\text{intrinsic}}$. The overall reddening along the line-of-sight in the direction of HD 127493 is listed in the Infrared Science Archive[6] using data from Schlafly & Finkbeiner (2011) as $E_{B-V} = 0.0801 \pm 0.0006$. This can be seen as an upper limit on the reddening.

The theoretical $V-$flux (at 5454 Å) was obtained from interpolation between synthetic non-LTE spectra to match the effective temperature and surface gravity determined from the spectral analysis of HD 127493. To compute the absolute magnitude of the star from the theoretical model flux, the flux has to be scaled with the star's radius, which can be calculated from the surface gravity g and mass M: $R = \sqrt{GM/g}$, where G is the gravitational constant. The surface gravity was obtained from the spectroscopic analysis and a canonical subdwarf mass was assumed ($0.48\,M_\odot$). After correcting the apparent magnitude for reddening, the distance can be calculated by simply using the distance modulus: $d_{\text{spectroscopic}} = 10^{1+(m_V-M_V)/5}$.

When the total line-of-sight reddening is assumed, the spectroscopic distance was computed to be $d_{\text{spectroscopic}} = 178 \pm 32\,\text{pc}$, which can be seen as a lower limit for the spectroscopic distance. If reddening is disregarded entirely, the computed distance increases to $d_{\text{spectroscopic}} = 202 \pm 36\,\text{pc}$. Both values agree reasonably well with the parallax distance $d_{\text{parallax}} = 184^{+53}_{-34}\,\text{pc}$, indicating that both the assumption of mass as well as the determined surface gravity are not too far off.

3.5 Atmospheric Structure

The temperature stratification in a model atmosphere has a strong influence on the emergent synthetic spectra for different models. It is influenced by the effective temperature, surface gravity and the abundances of all included elements. In the following, some of these effects will be discussed by comparing the temperature stratification in different models included in the nitrogen 3D-grid. The abundance of nitrogen in mass fraction is the same in all models. The effective temperature and surface gravity are the same for all models ($T_{\text{eff}} = 40000\,\text{K}$ and $\log g = 5.40$), except of course for those where the effect of T_{eff} and $\log g$ was tested.

Changing the effective temperature will obviously also modify the temperature stratification. However, shifting the effective temperature by a certain amount does not simply lead to the same shift in the temperature stratification (see Fig. 20a). Instead, the shift in temperature is different for each column mass. Higher column densities correspond to deeper regions in the atmosphere. This is because the effective temperature also influences the population of energy levels of all atoms included, which in turn affects the temperature.

[6] `https://irsa.ipac.caltech.edu/applications/DUST/`

For example, increasing the temperature from 40 000 K to 45 000 K leads to a higher population of N IV ions compared to N III (see section 3.5.1).

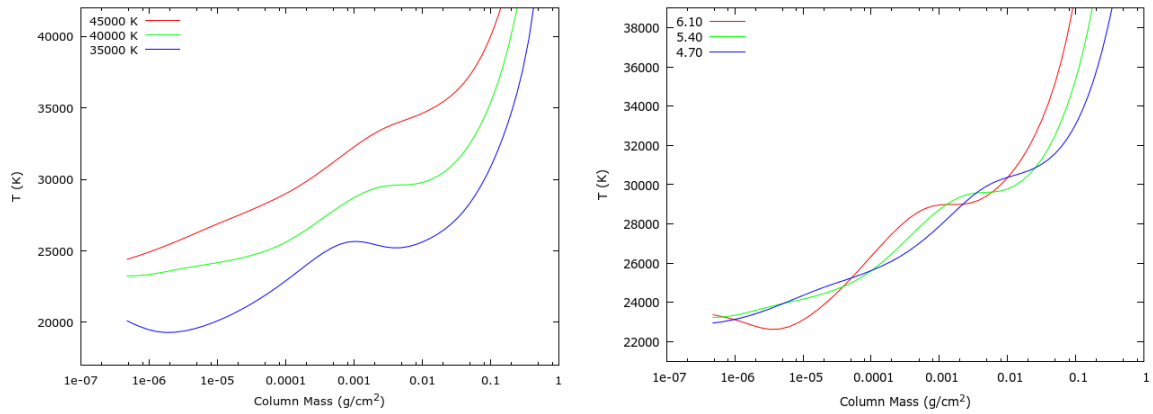

(a) Changing the effective temperature

(b) Changing the surface gravity

Figure 20. Temperature stratification for models with $T_{\rm eff} = 40\,000$ K, $\log g = 5.40$ (unless varied) and $\log N({\rm He})/N({\rm H}) = 0.3$.

The surface gravity is a measure for the density in the atmosphere. Therefore, the temperature stratification curve gets shifted towards the surface when the surface gravity is increased (see Fig. 20b). Even though the effective temperature is the same for all models, the temperature at higher column densities increases for higher surface gravities.

An increased helium abundance also leads to lower temperatures at every depth (Fig. 21a). For higher helium abundance, the curve is additionally shifted towards the surface. Since helium is heavier than hydrogen, this minor effect might be explained by a higher overall density in the atmosphere for higher helium abundances.

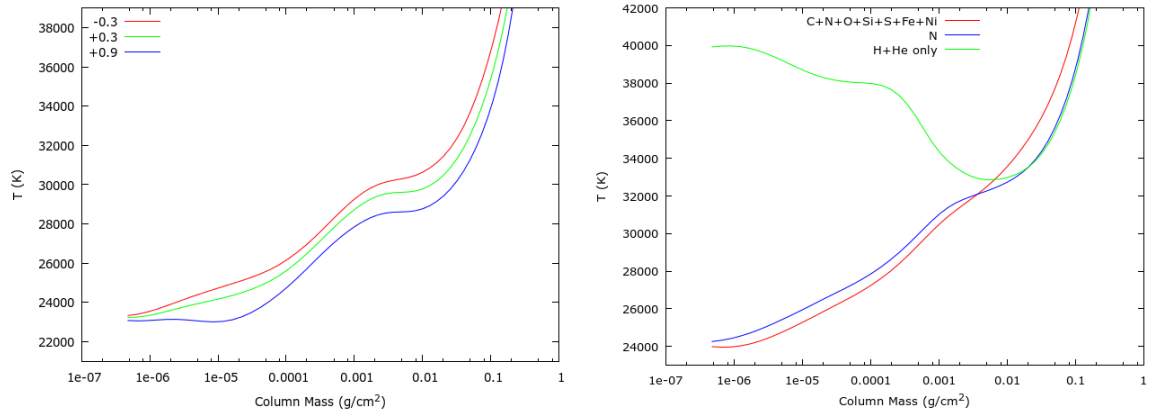

(a) Changing He abundance

(b) With line-blanketing from Fe and Ni (red) and without (blue+green)

Figure 21. Temperature stratification with $T_{\rm eff} = 40\,000$ K and $\log g = 5.40$ shown in the left-hand panel (a) as well as $T_{\rm eff} = 42\,484$ K, $\log g = 5.60$ and $\log N({\rm He})/N({\rm H}) = 0.62$ shown in panel (b).

When including additional chemical elements, mostly the outer layers of the atmosphere are affected by the increased opacity created by absorption lines in the UV

range (see Fig. 22, left-hand panel). This additional opacity blocks outgoing flux, so the continuum flux has to rise in order to ensure flux conservation. According to Haas (1997), this requires a steeper temperature gradient in the region where the continuum originates, leading to higher temperatures (the so-called back-warming effect). At the same time, the temperature is lowered in the outer atmosphere, where metal lines add opacity ("Surface Cooling"). Because this region is optically thin in comparison, photons emitted as a result of inelastic collision excitation are likely to leave the atmosphere without further interaction, actively cooling the plasma. Both effects become apparent in Fig. 21b when comparing the model with nitrogen only (blue) to the fully line-blanketed one (red): including additional elements to the model lowers the temperature at column masses below $\sim 0.01\,\mathrm{g/cm^2}$ while deeper regions are heated. Even adding only one additional chemical element to a H-He only model results in a large temperature difference below $10^{-3}\,\mathrm{g/cm^2}$ due to the "Surface Cooling" effect.

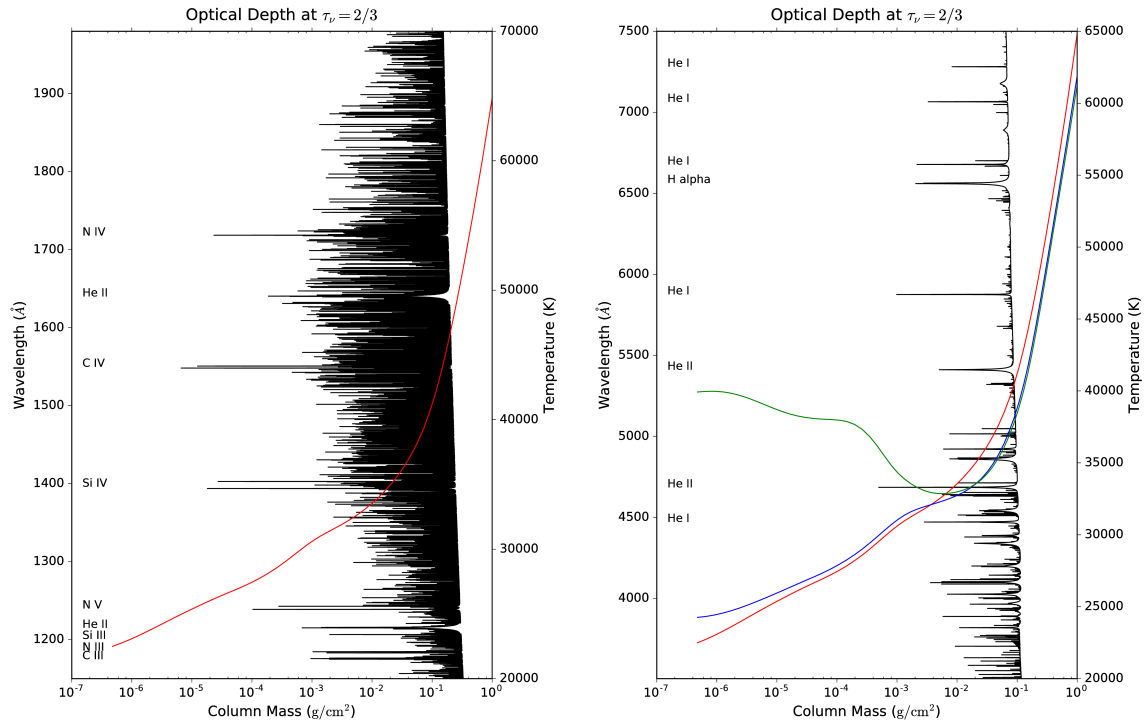

(a) UV range (b) Visual range

Figure 22. Temperature stratification and monochromatic optical depth $\tau_\nu = 2/3$ as functions of column mass density for the final fully line-blanketed model defined by $T_{\mathrm{eff}} = 42\,484\,\mathrm{K}$, $\log g = 5.6$, and $\log N(He)/N(H) = 0.62$. Like in Fig. 21, the temperature stratification for models including H+He only (green), N (blue) and a fully line-blanketed model (red) is shown in the optical range. All depths at which lines are formed are included in all models.

Fig. 22 shows at which column densities in the atmosphere the monochromatic optical depth $\tau_\nu = 2/3$ is reached (i. e. where about half of the photons escape the photosphere). In combination with the temperature stratification profile, this makes it possible to analyze how single lines are affected by or affect the temperature at a certain column density. Many metal lines in the UV range form at low column densities close to the surface. Lines in the optical range, most importantly many helium and hydrogen lines, are created deeper in the atmosphere, between 10^{-1} and $10^{-2}\,\mathrm{g/cm^2}$.

It is this region which is affected the most by the back-warming effect: the temperature is $\sim 1000\,\mathrm{K}$ higher at $10^{-2}\,\mathrm{g/cm^2}$ and $\sim 2000\,\mathrm{K}$ at $10^{-1}\,\mathrm{g/cm^2}$ compared to a model only including nitrogen as a metal.

In which way this can affect hydrogen and helium line profiles will be discussed in section 3.6.1.

3.5.1 Ionization stratification

Since the metal ionization fractions as a function of depth depend strongly on the effective surface temperature, observing multiple ionization stages for every element is useful to constrain the effective surface temperature. The ionization equilibria for N II-VI in two model atmospheres are shown in Fig. 23.

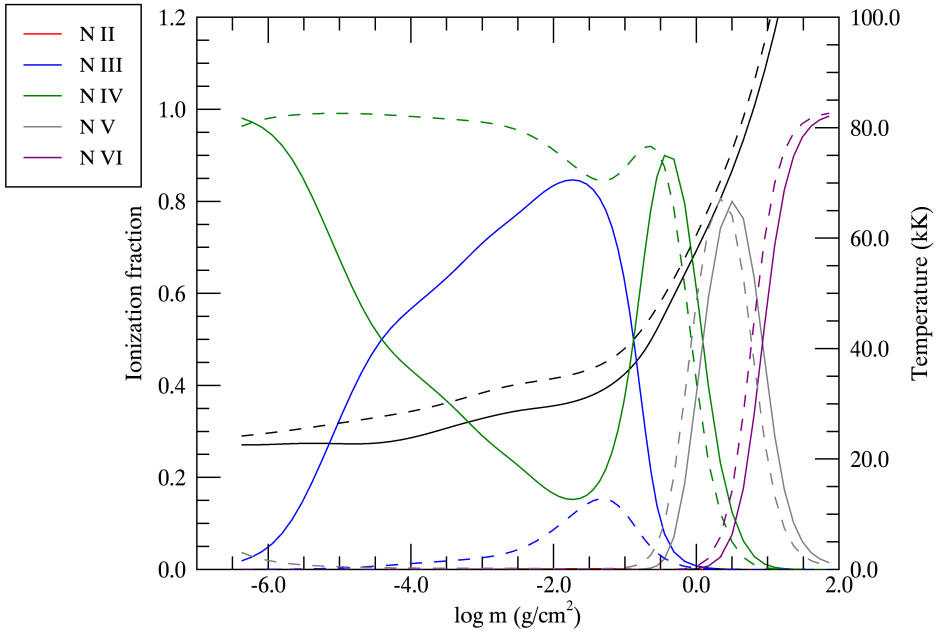

Figure 23. Ionization fractions of nitrogen as functions of depth, where m is the column density, in models with $T_{\mathrm{eff}} = 40\,000\,\mathrm{K}$ (solid lines) and $45\,000\,\mathrm{K}$ (dashed lines), $\log g = 5.4$, and $\log N(\mathrm{He})/N(\mathrm{H}) = 0.3$. The black curves show the temperature stratification of the two models.

As seen in Fig. 22, the line forming region for nitrogen extends from densities just above $10^{-1}\,\mathrm{g/cm^2}$ to about $10^{-5}\,\mathrm{g/cm^2}$. In the model at $40\,000\,\mathrm{K}$, a large part of this region is dominated by N III while N IV dominates only at very low or high densities. However, when the temperature is raised to $45\,000\,\mathrm{K}$, almost all nitrogen in the line forming region is in the N IV ionization stage. N V and N VI ionization stages are less dependent on the temperature in this regime. In both models, N VI becomes prevalent only in the hotter, deeper layers of the star that are too opaque to form lines in the observed UV and optical spectra. Interestingly, the ionization fraction of N V is also low at the densities where the core of the N V resonance doublet lines is formed ($10^{-5} - 10^{-4}\,\mathrm{g/cm^2}$). Because of the strength of this transition, the doublet is visible regardless. In both models, only a very small fraction of nitrogen atoms is in the N II ionization stage (see Fig. 25 for visibility of N II in a similar model). This might be a reason for the problems with N II emission lines in the `TLUSTY/SYNSPEC` synthetic spectra.

The ionization profile for some models that were used to determine metal abundances is shown in Fig. 24. It displays the effect of line-blanketing on the ionization structure of nitrogen by comparing a nitrogen-only model atmosphere to the fully line-blanketed one. The number of nitrogen atoms in each ionization stage for the fully line-blanketed model is shown in Fig. 25 on a logarithmic scale to make the N II population visible.

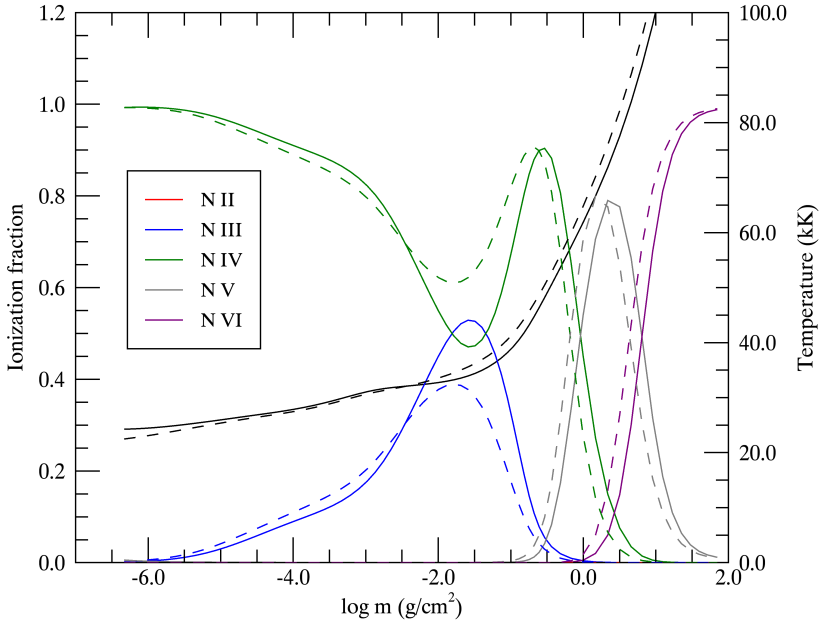

Figure 24. Ionization fractions of nitrogen as function of depth in models including nitrogen only (solid lines) and C+N+O+Si+S+Fe+Ni (dashed lines) with atmospheric parameters $T_{\rm eff} = 42\,484$ K, $\log g = 5.6$, and $\log N({\rm He})/N({\rm H}) = 0.62$. The black curves show the temperature profiles of the two models.

As expected from the change in temperature stratification, the population of N IV-VI is increased in the line-blanketed model for high column densities, while it is lowered towards the surface. The reverse effect is seen for N III. Since the differences can be quite large, especially in line-forming regions, this underlines the importance of using line-blanketed models for fitting metal lines even in the optical range.

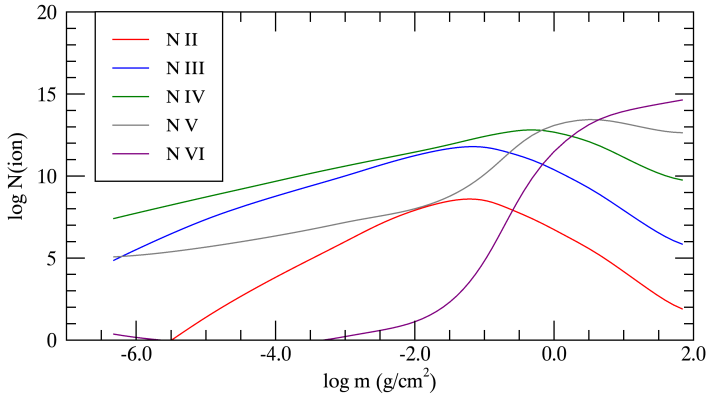

Figure 25. Population of nitrogen atoms in a given ionization stage for the same fully line-blanketed model as shown in Fig. 24. Even though only a small fraction of nitrogen atoms is in the N II ionization stage, some N II lines are visible in the optical spectrum.

3.6 Comparing models

3.6.1 Line-blanketing

Some of the poorly fitting lines can be explained by the missing line-blanketing in the 3D-grids. In order to test which lines are affected, a fully line-blanketed synthetic spectrum, most importantly including iron and nickel in non-LTE, was fitted with the C+N+Si 3D-grid (see Table 4). As expected from the difference in temperature stratification induced by the back-warming and surface cooling effects, He I lines become weaker and He II lines become stronger when line-blanketing is taken into account (see Fig. 26 and 27).

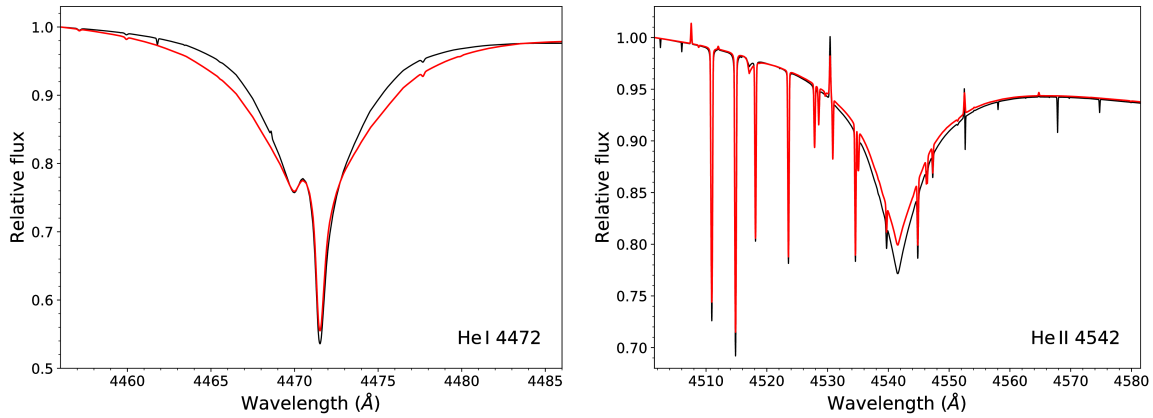

Figure 26. Close-up on He I 4472 Å and He II 4542 Å, where the black curve is the synthetic line-blanketed model spectrum and the red curve is a model spectrum including nitrogen only, computed for the same parameters as used in the line-blanketed model. He I 4472 Å is clearly weaker in the line-blanketed model (especially the wings). The emission features are N II lines which are not properly modeled.

He II 4542 Å, He II 5412 Å and He II 4686 Å are strongly influenced by line-blanketing. Fitting these lines with models that do not include Fe+Ni would result in a higher temperature. A fit of all lines that were used to determine the atmospheric parameters in section 3.2 with both 3-D grids gives temperatures that are about 2000 K too high (again, with purely statistical uncertainties):

	$T_{\rm eff}$ (K)	$\log g$	$\log N({\rm He})/N({\rm H})$
Full model (Input)	42484	5.6	0.62
3D-grid fit with N	44294.5 ± 30.5	5.6 ± 0.0	0.5 ± 0.0
3D-grid fit with C+N+Si	44407.9 ± 32.1	5.6 ± 0.0	0.5 ± 0.0

Table 4. Results from fitting 13 H, He I, and He II lines in the synthetic fully line-blanketed spectrum simultaneously using the 3D-grids as described in section 3.2. The statistical errors on $\log g$ and $\log N({\rm He})/N({\rm H})$ are too small to be shown.

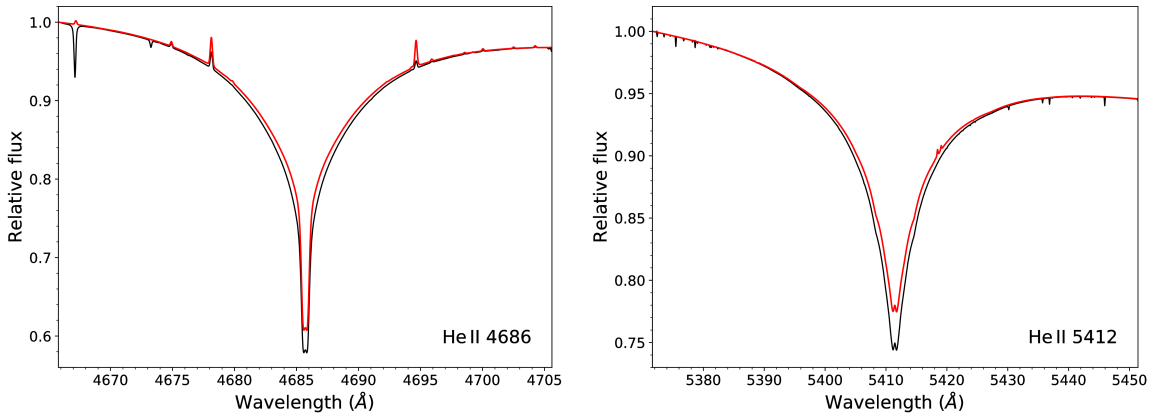

Figure 27. Close-up on He II 5412 Å, where the black curve is the synthetic fully line-blanketed spectrum and the red curve is a synthetic spectrum including nitrogen only, computed for the same parameters as used in the fully line-blanketed model. Both lines are clearly much stronger in the fully line-blanketed model and should be treated with caution when fitting with models that do not include line-blanketing. Most other He II lines are less sensitive to line-blanketing.

3.6.2 `TMAP` and `TLUSTY`

The helium abundance and atmospheric parameters determined in section 3.2 show differences to values determined by Hirsch (2009) even though the same FEROS spectra were used. So where does this difference come from? Hirsch (2009) used the `TMAP` (**T**übingen NLTE **M**odel-**A**tmosphere **P**ackage) code to compute an extensive grid of model atmospheres to derive atmospheric parameters. Like in one of the 3D-grids used in this work, only nitrogen was included. In order to check for differences between both model codes, one model from the `TMAP` grid is compared with a `TLUSTY` model computed for the same parameters: $T_{\rm eff} = 40\,000$ K, $\log g = 5.4$, and $\log N({\rm He})/N({\rm H}) = 0$.

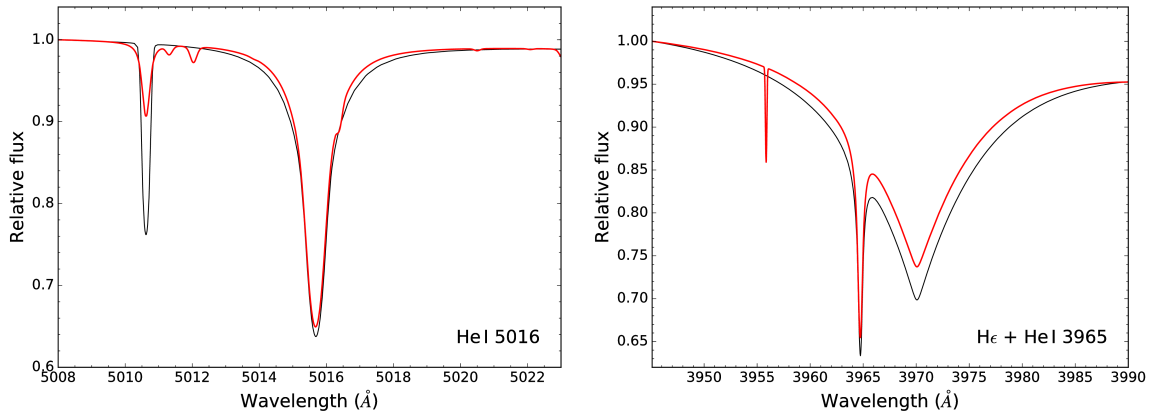

Figure 28. Close-up on H ϵ and He I 5016 Å, where the black curve is a synthetic `TMAP` model and the red curve is a new `TLUSTY` model computed for the same parameters as used in the `TMAP` model. Like all H Balmer lines, H ϵ is stronger in `TMAP`.

Judging by this simple comparison, the differences in model codes seem to be quite large. Indeed all hydrogen and He II lines considered are stronger in the `TMAP` model (see Fig. 29). Most H I lines are of similar strength on both models (Fig. 28). Considering these large differences in models, it seems remarkable that the results for the atmospheric parameters derived by both grids are still similar.

	$T_{\rm eff}$ (K)	$\log g$	$\log N({\rm He})/N({\rm H})$
TMAP	40000	5.40	0.0
TLUSTY fit	41260 ± 110	5.487 ± 0.020	0.0548 ± 0.022

Table 5. Results from fitting a synthetic TMAP spectrum in the same manner as performed in section 3.2.

However, a global fit of the TMAP synthetic spectrum with a TLUSTY 3D-grid like in section 3.2 (neglecting H α though) shows no serious deviations (Table 5). This can most likely be explained by two counteracting effects that cancel out: He II lines require a high effective temperature ($\sim$ 45 000 K) while the hydrogen Balmer lines fit better for lower temperatures ($\sim$ 35 000 K). He I lines fit best with a temperature around 40 000 K. The surface gravity seems to be similar for all lines in both model codes. Since the number of selected He I and He II lines is about equal, this may explain the similar results derived by both model grids. More testing is required in order to find the reason for this discrepancy.

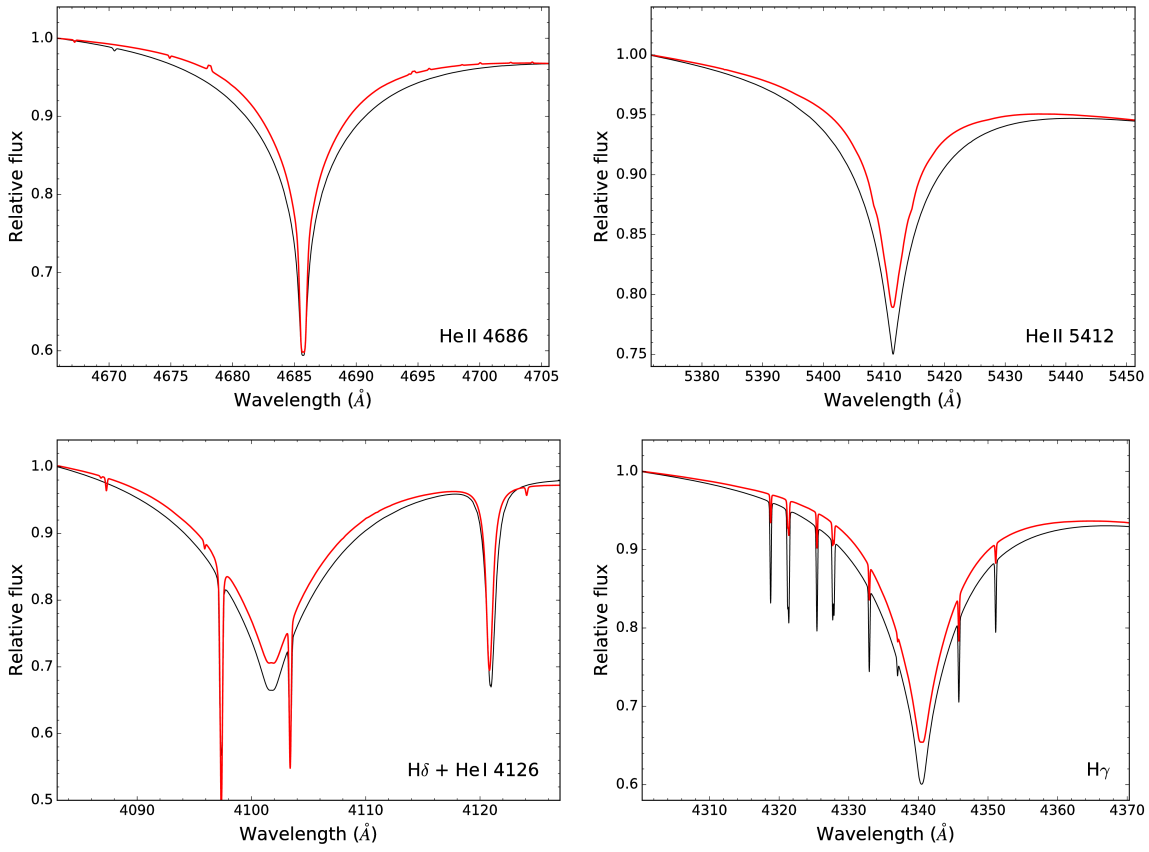

Figure 29. Close-up on He II and H Balmer lines, where the black curve is the synthetic TMAP model and the red curve is a new TLUSTY model computed for the same parameters. All lines are stronger and the two He II lines give better fits to observed FEROS spectra with TMAP.

4 Conclusion

The atmospheric parameters for HD 127493 were revisited using a small new grid of models and synthetic spectra computed with `TLUSTY/SYNSPEC`. Although the results are slightly different from those found by Hirsch (2009), they agree well within the range of realistic uncertainties. Some systematic errors to the new values might be caused by the interpolation of model atmospheres since the grid is very coarse. Considering the derived surface gravity and canonical mass, the spectroscopic distance matches the Hipparcos parallax distance very well. As the main part of this work, metal abundances in the atmosphere of HD 127493 were determined, including iron and nickel. They were obtained by fitting a large number of metal lines in high-resolution optical and UV spectra. The HST-GHRS spectra in the UV range turned out to be especially useful for determining reliable metal abundances and could be reproduced well in the final synthetic spectrum. The results from this analysis are consistent with the nitrogen abundance found by Hirsch (2009). The atmosphere of HD 127493 is enriched in nitrogen but depleted in carbon while the abundances of silicon and sulfur are similar to that of the Sun. Interestingly, both iron and nickel are enriched compared to solar values, most notably for nickel.

Based on these results, a hot flasher origin for HD 127493 can be considered unlikely. Models by Miller Bertolami et al. (2008) fail to explain He-sdOs depleted in carbon but enriched in nitrogen. They also rely on an enhanced mass-loss at the top of the RGB, which is hard to explain in a single-star system. Merger scenarios seem to be more promising. The slow- and low-mass composite-merger scenarios of two He-WD presented by Zhang & Jeffery (2012) are able to produce He-rich sdOs with a high abundance of nitrogen. The merger of a He-WD with a M-dwarf main-sequence star could potentially produce a similar result (Zhang et al. 2017). However, both of those papers do not consider a rotational velocity for the merger product. The rotational velocity of a He-WD+He-WD merger product would be orders of magnitude higher than the observed $v_{\rm rot}$ below 10 km/s, if no angular momentum were lost (Gourgouliatos & Jeffery 2006). They also do not consider semi-convective or rotational mixing, which could strongly influence the element abundance in the atmosphere. The same is the case for the strength of gravitational settling and radiative levitation, which might be able to explain the enrichment in iron and nickel in HD 127493. Another problem is the evolution timescale: while evolutionary tracks from merger scenarios (see Fig. 4) cover a wide temperature/surface gravity range, this evolution is predicted to be very fast until the last minor He-flash close to the EHB. In a $T_{\rm eff} - \log g$ diagram, HD 127493 is located above the EHB, where the evolution is predicted to be very fast.

As a sideline, the effect of line-blanketing on hydrogen and helium lines was tested and a comparison between `TLUSTY` and `TMAP` models was performed. In HD 127493, He II 4542 Å, He II 5412 Å and He II 4686 Å among others are strongly influenced by line-blanketing, so fits for atmospheric parameters should be performed using line-blanketed atmospheres in order to achieve the best accuracy.

From a superficial comparison between `TLUSTY` and `TMAP`, the differences seem to be quite large. To verify this discrepancy, a detailed analysis would require the computation of new models with both codes and comparison between temperature stratification.

Overall, the riddle of the origin of HD 127493, but also intermediate He-sdOs in general, is still not solved. More detailed evolutionary simulations, including a more complete treatment of the atmosphere, are needed. These could then be compared with detailed analysis of the abundance of chemical elements from high-quality UV spectra.

5 Bibliography

Asplund, M., Grevesse, N., Sauval, A. J., & Scott, P. 2009, Annual Review of Astronomy and Astrophysics, 47, 481

Bauer, F. & Husfeld, D. 1995, Astronomy & Astrophysics, 300, 481

Carroll, B. W. & Ostlie, D. A. 2007, Introduction to Modern Astrophysics (Pearson Addison-Wesley)

Code, A. D. & Welch, G. A. 1979, The Astrophysical Journal, 228, 95

Copperwheat, C. M., Morales-Rueda, L., Marsh, T. R., Maxted, P. F. L., & Heber, U. 2011, Monthly Notices of the Royal Astronomical Society, 415, 1381

Fitzpatrick, E. L. 1999, Publications of the Astronomical Society of the Pacific, 111, 63

Fontaine, G., Green, E., Brassard, P., Latour, M., & Chayer, P. 2014, in Astronomical Society of the Pacific Conference Series, Vol. 481, 6th Meeting on Hot Subdwarf Stars and Related Objects, ed. V. van Grootel, E. Green, G. Fontaine, & S. Charpinet, 83

Geier, S., Kupfer, T., Heber, U., et al. 2015, in Astronomical Society of the Pacific Conference Series, Vol. 493, 19th European Workshop on White Dwarfs, ed. P. Dufour, P. Bergeron, & G. Fontaine, 475

Geier, S., Kupfer, T., Ziegerer, E., et al. 2016, Journal of Physics: Conference Series, 728, 072017

Gourgouliatos, K. N. & Jeffery, C. S. 2006, Monthly Notices of the Royal Astronomical Society, 371, 1381

Gray, D. F. 2005, The Observation and Analysis of Stellar Photospheres (Cambridge University Press)

Groth, H. G., Kudritzki, R. P., & Heber, U. 1985, Astronomy and Astrophysics, 152, 107

Haas, S. 1997, PhD thesis, Friedrich-Alexander University Erlangen-Nürnberg

Han, Z., Podsiadlowski, P., Maxted, P. F. L., Marsh, T. R., & Ivanova, N. 2002, Monthly Notices of the Royal Astronomical Society, 336, 449

Heber, U. 2009, Annual Review of Astronomy and Astrophysics, 47, 211

Heber, U. 2016, Publications of the Astronomical Society of the Pacific, 128, 082001

Hirsch, H. A. 2009, PhD thesis, Friedrich-Alexander University Erlangen-Nürnberg

Hubeny, I. 1988, Computer Physics Communications, 52, 103

Hubeny, I. & Lanz, T. 1995, The Astrophysical Journal, 439, 875

Hubeny, I. & Lanz, T. 2000, SYNSPEC - A User's Guide

Hubeny, I. & Lanz, T. 2006, TLUSTY - A User's Guide

Irrgang, A. 2014, PhD thesis, Friedrich-Alexander University Erlangen-Nürnberg

Jao, W.-C., Henry, T. J., Beaulieu, T. D., & Subasavage, J. P. 2008, The Astronomical Journal, 136, 840

Jeffery, S., Naslim, N., Behara, N., & Hibbert, A. 2015, Astronomy and Geophysics, 56, 2.32

Kaufer, A., Stahl, O., Tubbesing, S., et al. 1999, The Messenger, 95, 8

Kramida, A., Yu. Ralchenko, Reader, J., & and NIST ASD Team. 2015, NIST Atomic Spectra Database (ver. 5.3), [Online]. Available: `http://physics.nist.gov/asd` [2017, July 29]. National Institute of Standards and Technology, Gaithersburg, MD.

Lanz, T., Brown, T. M., Sweigart, A. V., Hubeny, I., & Landsman, W. B. 2004, The Astrophysical Journal, 602, 342

Miller Bertolami, M. M., Althaus, L. G., Unglaub, K., & Weiss, A. 2008, Astronomy & Astrophysics, 491, 253

Münch, G. & Greenstein, J. L. 1955, in Carnegie Institution Year Books, ed. D. R. Swift, Vol. 54

Napiwotzki, R. 1997, Astronomy & Astrophysics, 322, 256

Napiwotzki, R. 2008, in Astronomical Society of the Pacific Conference Series, Vol. 391, Hydrogen-Deficient Stars, ed. A. Werner & T. Rauch, 257

Napiwotzki, R., Yungelson, L., Nelemans, G., et al. 2004, in Astronomical Society of the Pacific Conference Series, Vol. 318, Spectroscopically and Spatially Resolving the Components of the Close Binary Stars, ed. R. W. Hilditch, H. Hensberge, & K. Pavlovski, 402–410

Paxton, B., Bildsten, L., Dotter, A., et al. 2011, The Astrophysical Journal Supplement, 192, 3

Schindler, J.-T., Green, E. M., & Arnett, W. D. 2015, The Astrophysical Journal, 806, 178

Schlafly, E. F. & Finkbeiner, D. P. 2011, The Astrophysical Journal, 737, 103

Scott, P., Asplund, M., Grevesse, N., Bergemann, M., & Sauval, A. J. 2015a, Astronomy and Astrophysics, 573, A26

Scott, P., Grevesse, N., Asplund, M., et al. 2015b, Astronomy and Astrophysics, 573, A25

Simon, K. P. 1982, Astronomy & Astrophysics, 107, 313

Stroeer, A., Heber, U., Lisker, T., et al. 2007, Astronomy and Astrophysics, 462, 269

Unglaub, K. 2010, in American Institute of Physics Conference Series, Vol. 1273, American Institute of Physics Conference Series, ed. K. Werner & T. Rauch, 251–254

van Leeuwen, F. 2007, Astronomy and Astrophysics, 474, 653

Webbink, R. F. 1984, The Astrophysical Journal, 277, 355

Yi, S. K. & Yoon, S.-J. 2004, Astrophysics and Space Science, 291, 205

Zhang, X., Hall, P. D., Jeffery, C. S., & Bi, S. 2017, The Astrophysical Journal, 835, 242

Zhang, X. & Jeffery, C. S. 2012, Monthly Notices of the Royal Astronomical Society, 419, 452

Appendices

A GHRS spectra

The complete GHRS spectral range (red) of HD 127493 compared with the fully line-blanketed synthetic spectrum using $T_{\rm eff} = 42484\,{\rm K}$, $\log g = 5.6$ and $\log N({\rm He})/N({\rm H}) = 0.62$, as well as a radial velocity of $-16\,{\rm km/s}$.

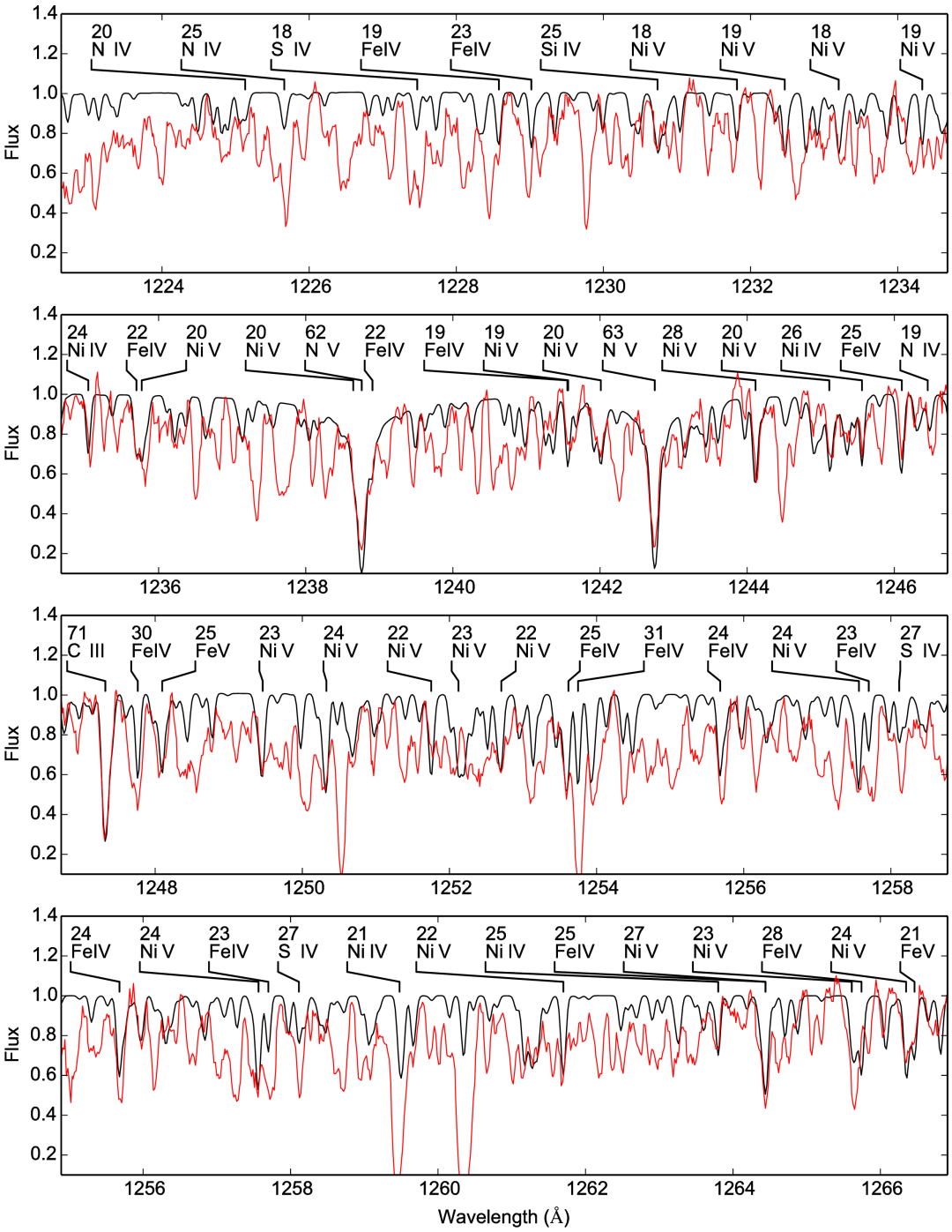

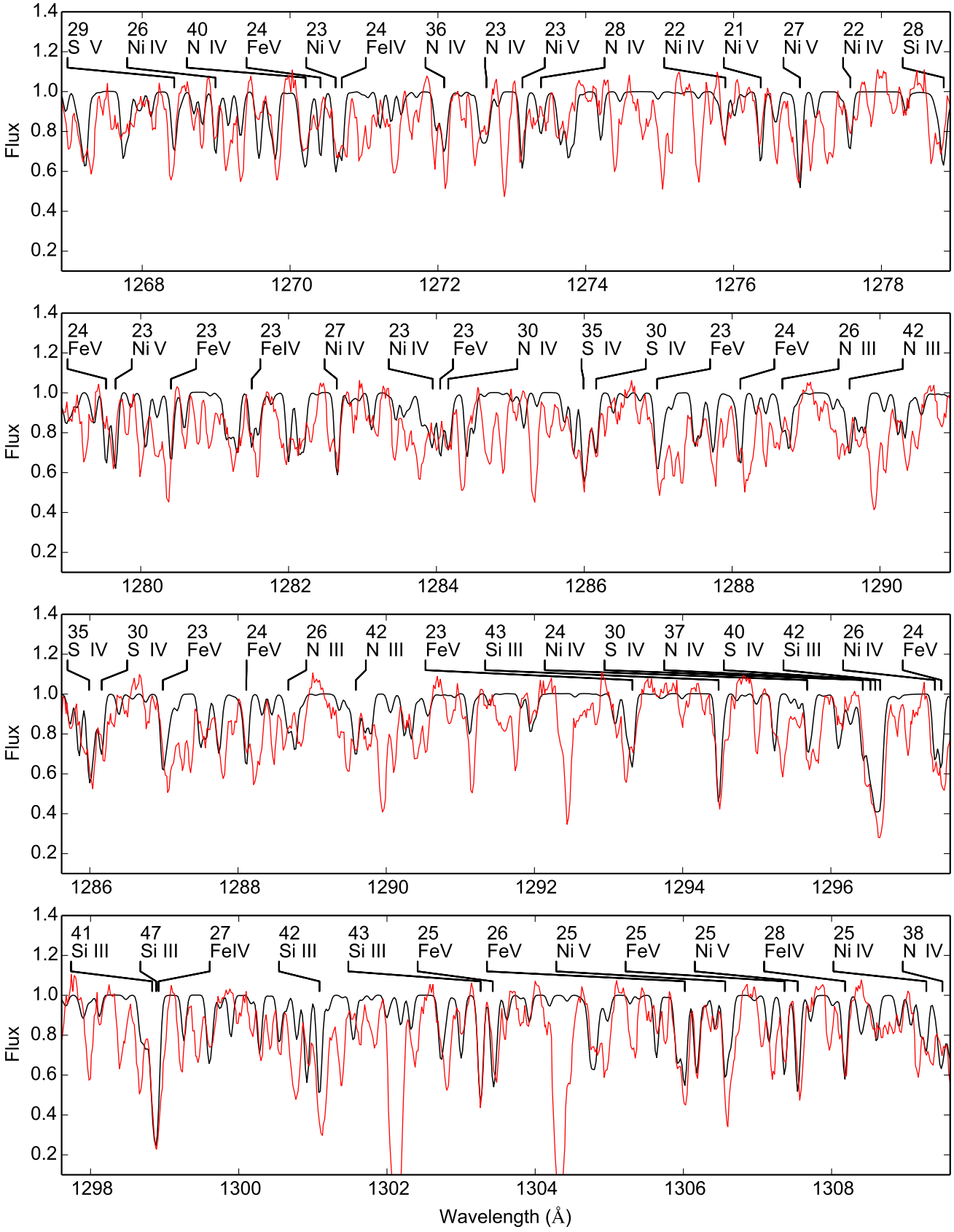
29 S V
26 Ni IV
40 N IV
24 FeV
23 Ni V
24 FeIV
36 N IV
23 N IV
23 Ni V
28 N IV
22 Ni IV
21 Ni V
27 Ni V
22 Ni IV
28 Si IV
24 FeV
23 Ni V
23 FeV
23 FeIV
27 Ni IV
23 Ni IV
23 FeV
30 N IV
35 S IV
30 S IV
23 FeV
24 FeV
26 N III
42 N III
35 S IV
30 S IV
23 FeV
24 FeV
26 N III
42 N III
23 FeV
43 Si III
24 Ni IV
30 S IV
37 N IV
40 S IV
42 Si III
26 Ni IV
24 FeV
41 Si III
47 Si III
27 FeIV
42 Si III
43 Si III
25 FeV
26 FeV
25 Ni V
25 FeV
25 Ni V
28 FeIV
25 Ni IV
38 N IV
Flux
Wavelength (Å)

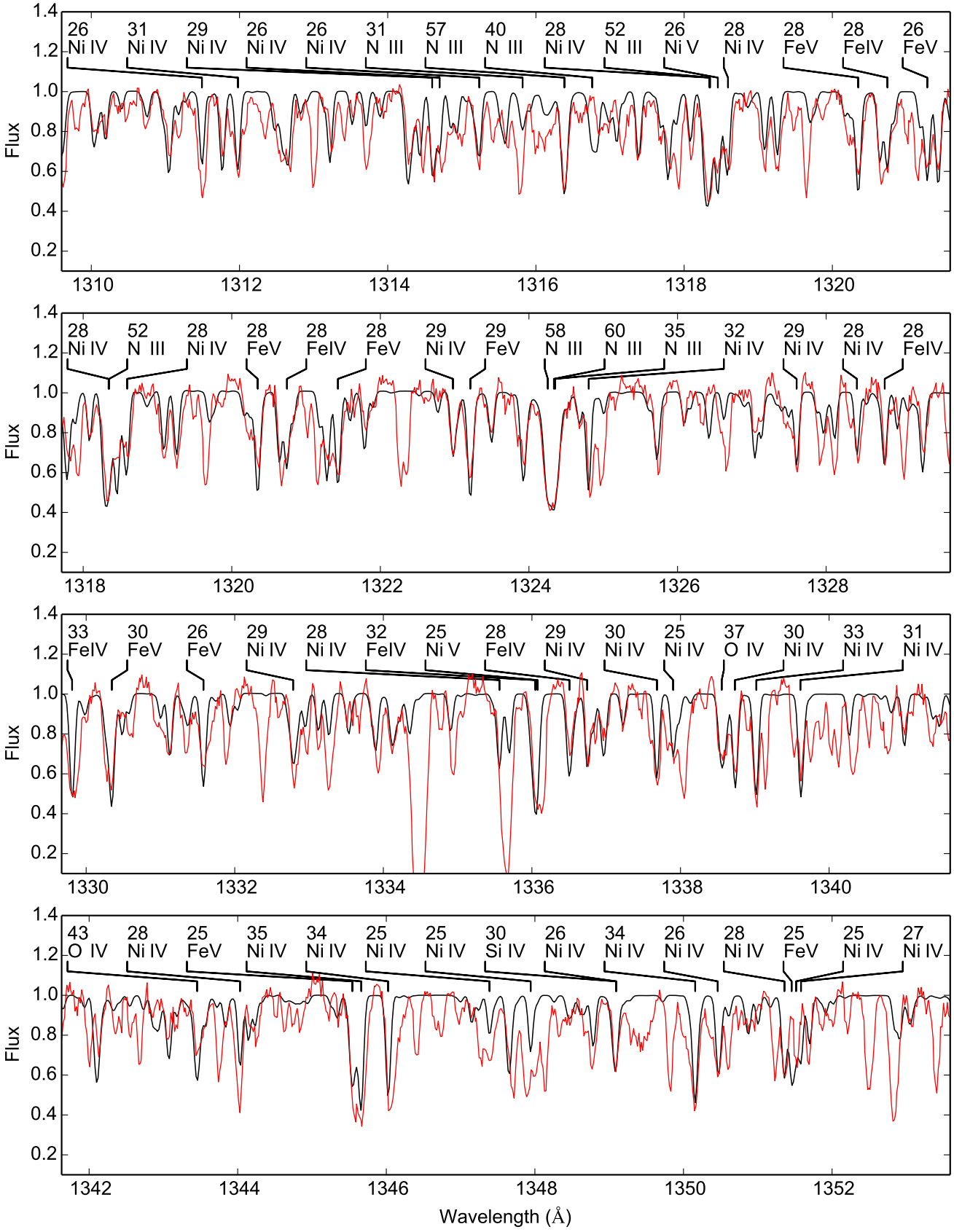
26 Ni IV
31 Ni IV
29 Ni IV
26 Ni IV
26 Ni IV
31 N III
57 N III
40 N III
28 Ni IV
52 N III
26 Ni V
28 Ni IV
28 FeV
28 FeIV
26 FeV
28 Ni IV
52 N III
28 Ni IV
28 FeV
28 FeIV
28 FeV
29 Ni IV
29 FeV
58 N III
60 N III
35 N III
32 Ni IV
29 Ni IV
28 Ni IV
28 FeIV
33 FeIV
30 FeV
26 FeV
29 Ni IV
28 Ni IV
32 FeIV
25 Ni V
28 FeIV
29 Ni IV
30 Ni IV
25 Ni IV
37 O IV
30 Ni IV
33 Ni IV
31 Ni IV
43 O IV
28 Ni IV
25 FeV
35 Ni IV
34 Ni IV
25 Ni IV
25 Ni IV
30 Si IV
26 Ni IV
34 Ni IV
26 Ni IV
28 Ni IV
25 FeV
25 Ni IV
27 Ni IV
Flux
Wavelength (Å)

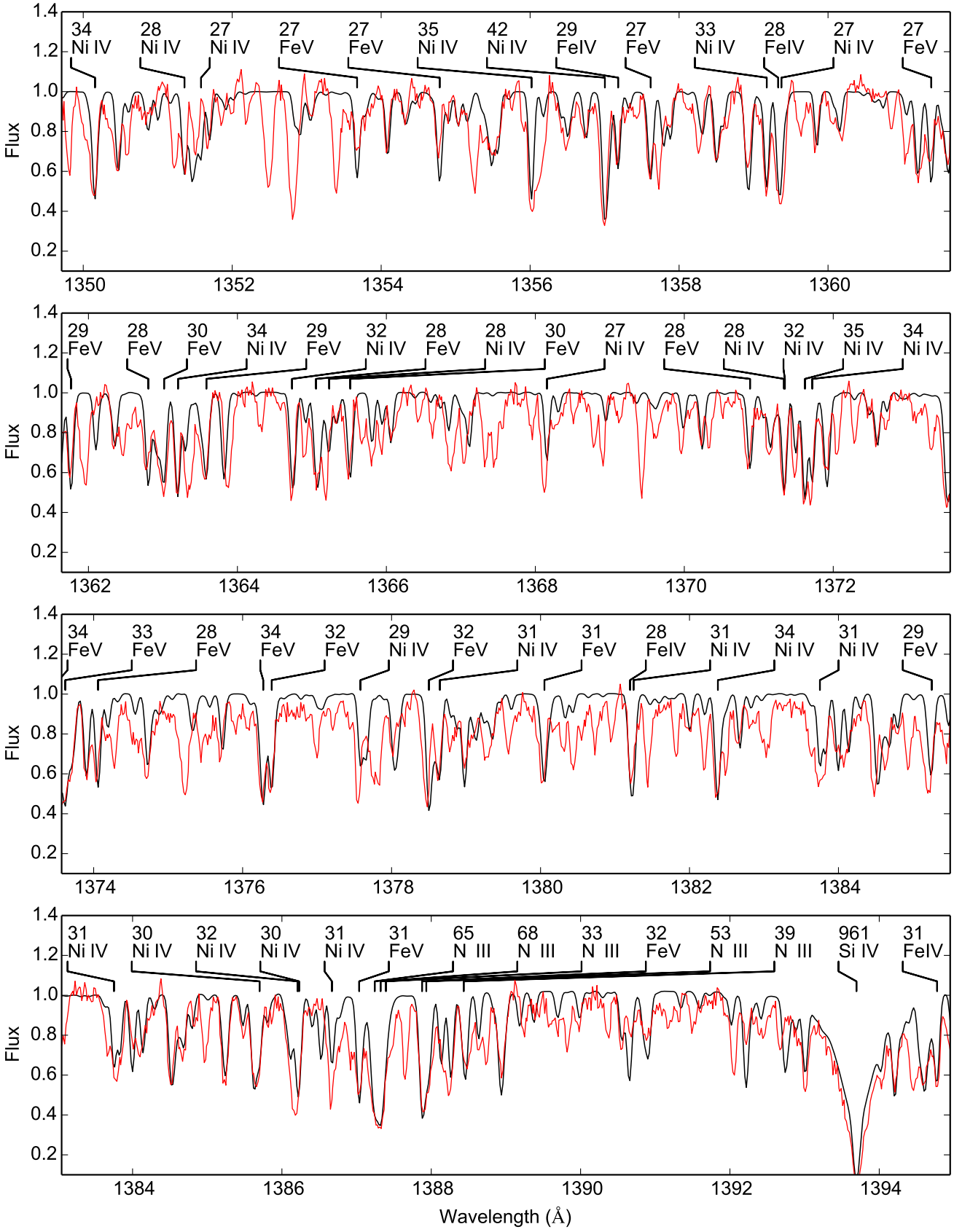
34 Ni IV
28 Ni IV
27 Ni IV
27 FeV
27 FeV
35 Ni IV
42 Ni IV
29 FeIV
27 FeV
33 Ni IV
28 FeIV
27 Ni IV
27 FeV
29 FeV
28 FeV
30 FeV
34 Ni IV
29 FeV
32 Ni IV
28 FeV
28 Ni IV
30 FeV
27 Ni IV
28 FeV
28 Ni IV
32 Ni IV
35 Ni IV
34 Ni IV
34 FeV
33 FeV
28 FeV
34 FeV
32 FeV
29 Ni IV
32 FeV
31 Ni IV
31 FeV
28 FeIV
31 Ni IV
34 Ni IV
31 Ni IV
29 FeV
31 Ni IV
30 Ni IV
32 Ni IV
30 Ni IV
31 Ni IV
31 FeV
65 N III
68 N III
33 N III
32 FeV
53 N III
39 N III
961 Si IV
31 FeIV
Flux
Wavelength (Å)

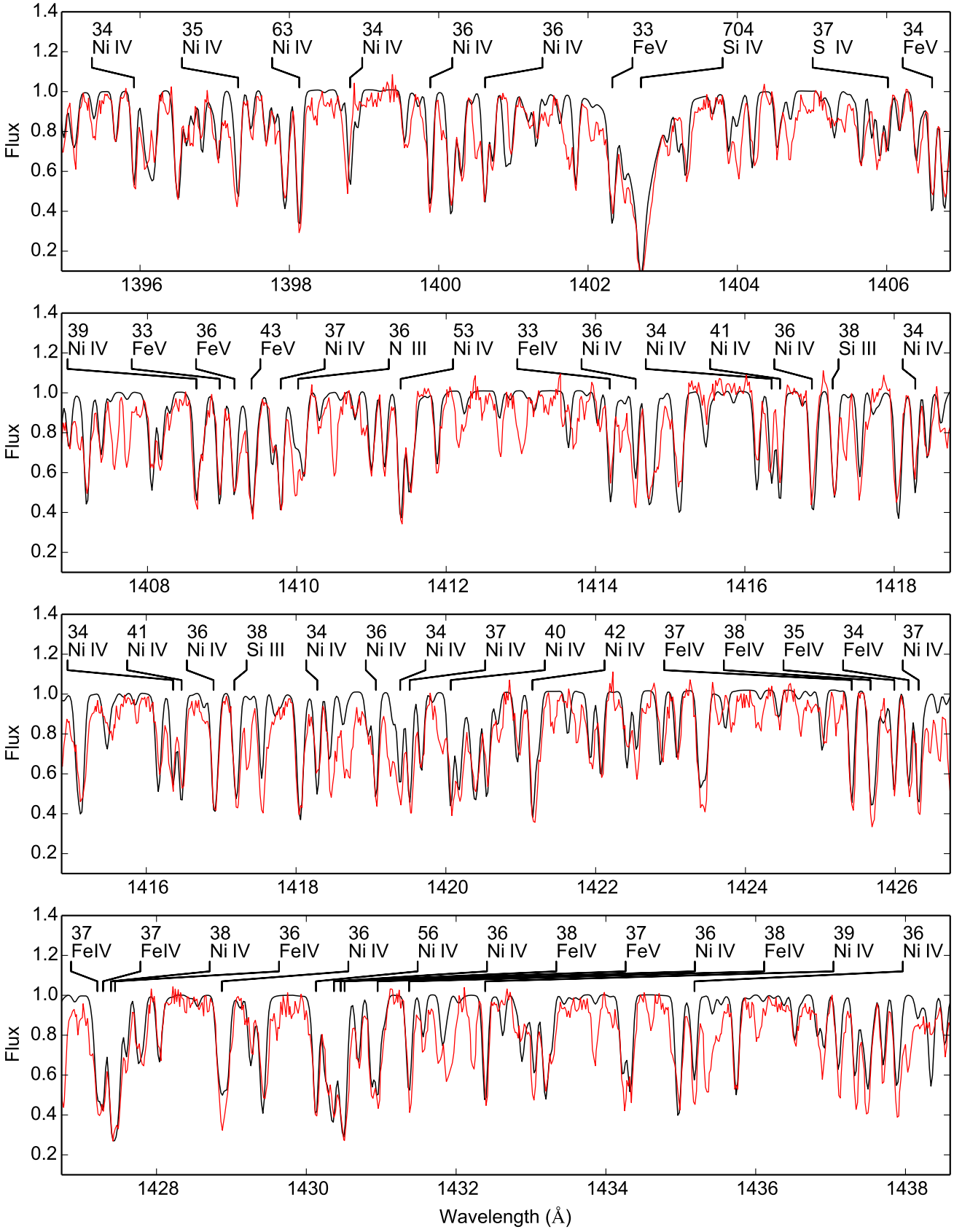
34 Ni IV
35 Ni IV
63 Ni IV
34 Ni IV
36 Ni IV
36 Ni IV
33 FeV
704 Si IV
37 S IV
34 FeV
39 Ni IV
33 FeV
36 FeV
43 FeV
37 Ni IV
36 N III
53 Ni IV
33 FeIV
36 Ni IV
34 Ni IV
41 Ni IV
36 Ni IV
38 Si III
34 Ni IV
34 Ni IV
41 Ni IV
36 Ni IV
38 Si III
34 Ni IV
36 Ni IV
34 Ni IV
37 Ni IV
40 Ni IV
42 Ni IV
37 FeIV
38 FeIV
35 FeIV
34 FeIV
37 Ni IV
37 FeIV
37 FeIV
38 Ni IV
36 FeIV
36 Ni IV
56 Ni IV
36 Ni IV
38 FeIV
37 FeV
36 Ni IV
38 FeIV
39 Ni IV
36 Ni IV
Flux
Wavelength (Å)

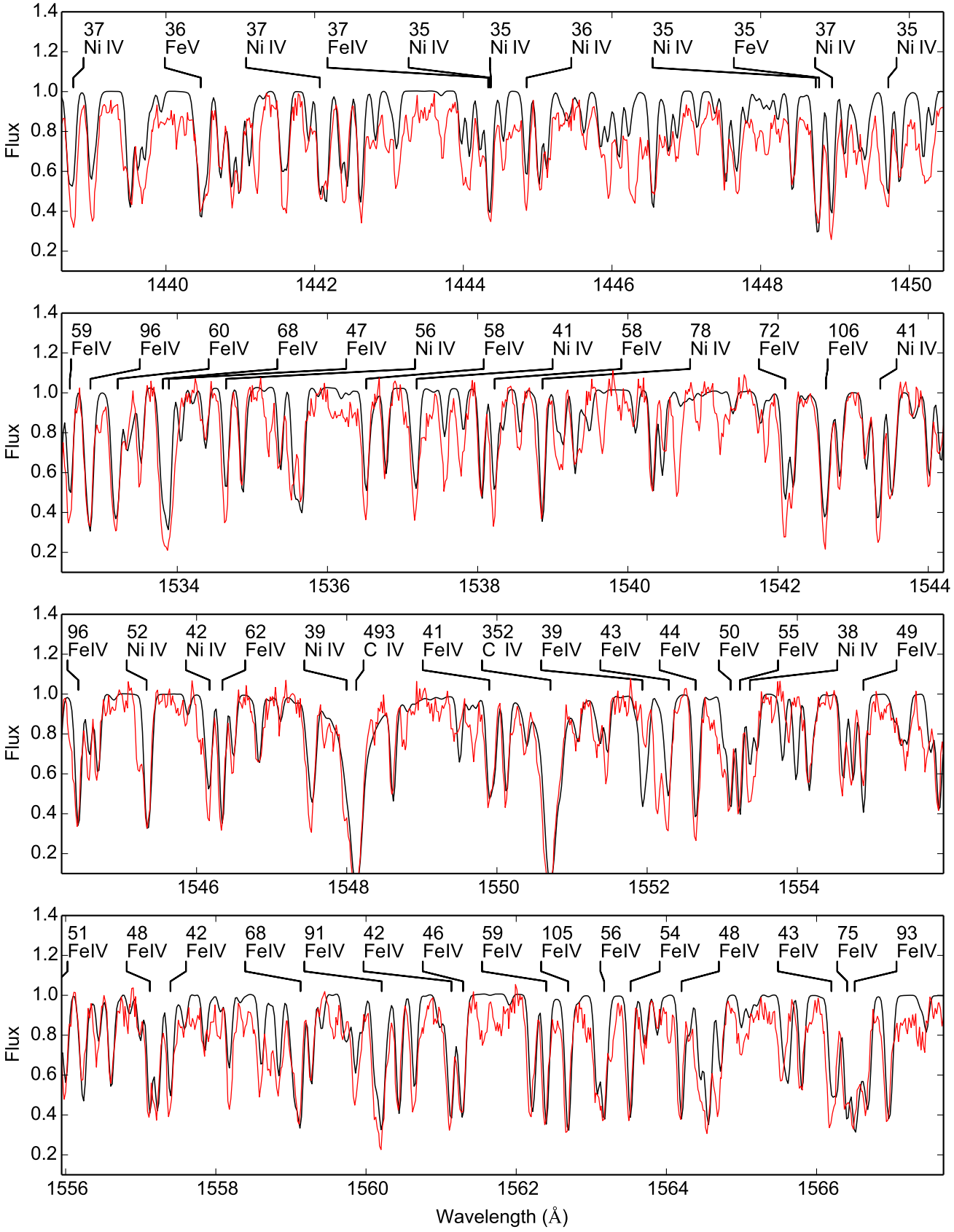
37 Ni IV
36 FeV
37 Ni IV
37 FeIV
35 Ni IV
35 Ni IV
36 Ni IV
35 Ni IV
35 FeV
37 Ni IV
35 Ni IV
59 FeIV
96 FeIV
60 FeIV
68 FeIV
47 FeIV
56 Ni IV
58 FeIV
41 Ni IV
58 FeIV
78 Ni IV
72 FeIV
106 FeIV
41 Ni IV
96 FeIV
52 Ni IV
42 Ni IV
62 FeIV
39 Ni IV
493 C IV
41 FeIV
352 C IV
39 FeIV
43 FeIV
44 FeIV
50 FeIV
55 FeIV
38 Ni IV
49 FeIV
51 FeIV
48 FeIV
42 FeIV
68 FeIV
91 FeIV
42 FeIV
46 FeIV
59 FeIV
105 FeIV
56 FeIV
54 FeIV
48 FeIV
43 FeIV
75 FeIV
93 FeIV
Flux
Wavelength (Å)

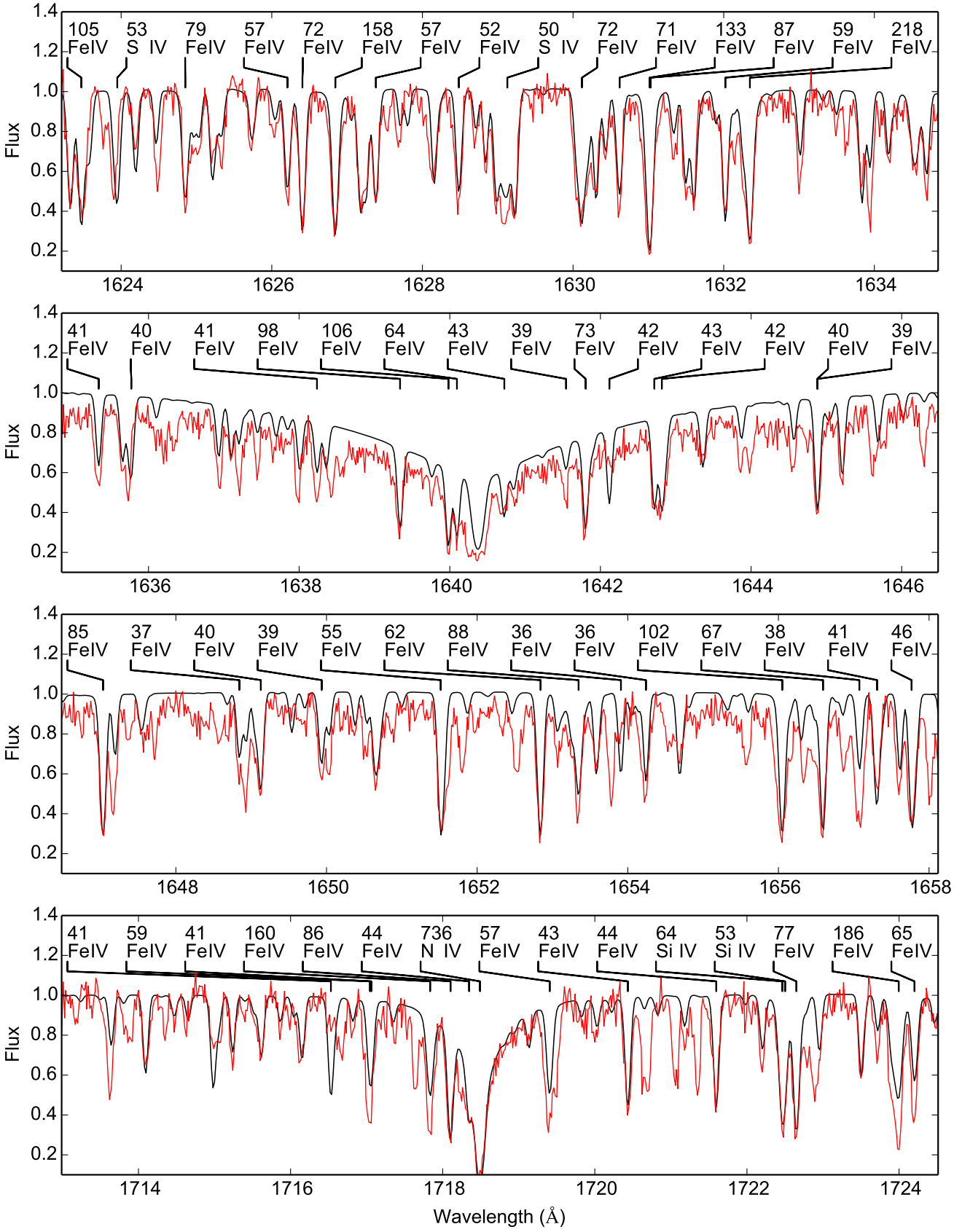
105 FeIV
53 S IV
79 FeIV
57 FeIV
72 FeIV
158 FeIV
57 FeIV
52 FeIV
50 S IV
72 FeIV
71 FeIV
133 FeIV
87 FeIV
59 FeIV
218 FeIV
41 FeIV
40 FeIV
41 FeIV
98 FeIV
106 FeIV
64 FeIV
43 FeIV
39 FeIV
73 FeIV
42 FeIV
43 FeIV
42 FeIV
40 FeIV
39 FeIV
85 FeIV
37 FeIV
40 FeIV
39 FeIV
55 FeIV
62 FeIV
88 FeIV
36 FeIV
36 FeIV
102 FeIV
67 FeIV
38 FeIV
41 FeIV
46 FeIV
41 FeIV
59 FeIV
41 FeIV
160 FeIV
86 FeIV
44 FeIV
736 N IV
57 FeIV
43 FeIV
44 FeIV
64 Si IV
53 Si IV
77 FeIV
186 FeIV
65 FeIV
Flux
Wavelength (Å)

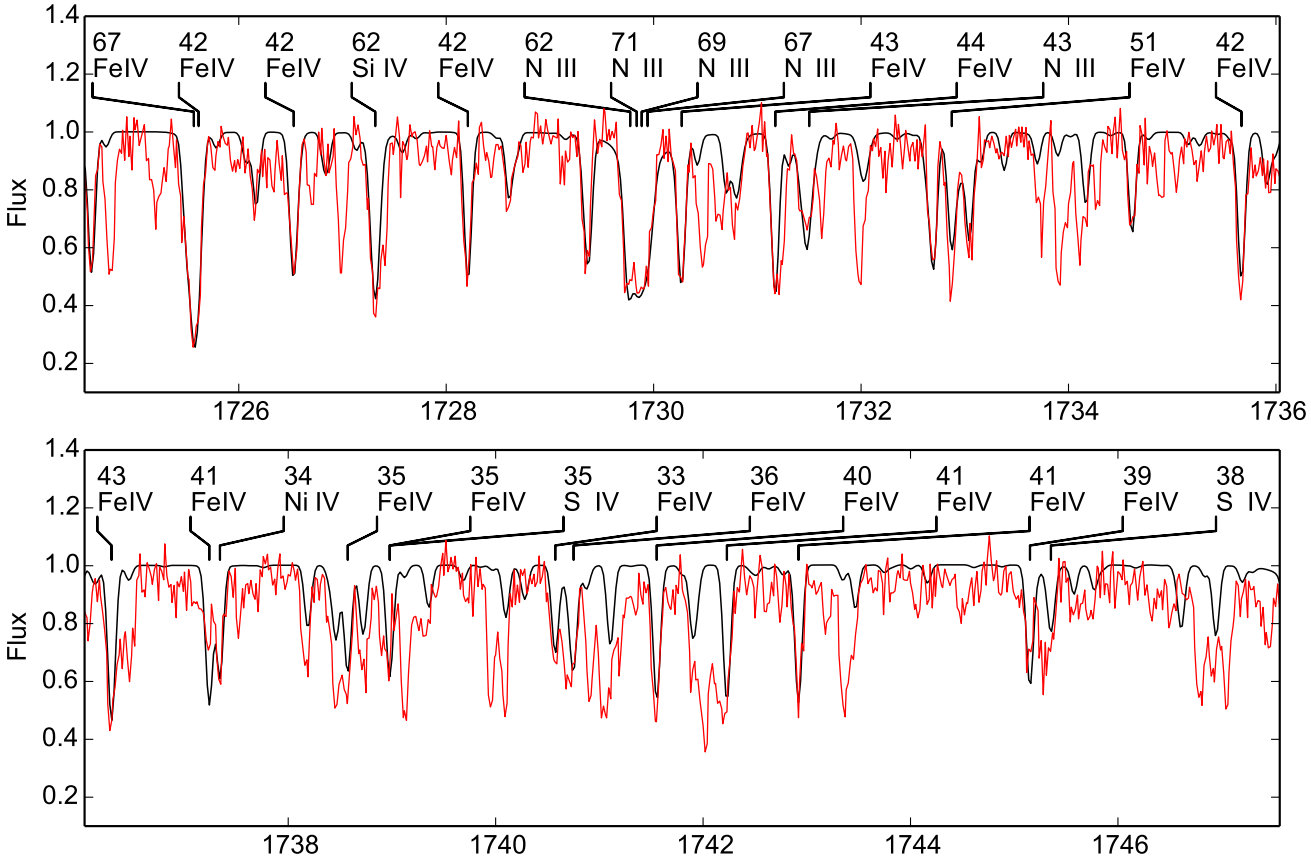
67 FeIV
42 FeIV
42 FeIV
62 Si IV
42 FeIV
62 N III
71 N III
69 N III
67 N III
43 FeIV
44 FeIV
43 N III
51 FeIV
42 FeIV
Flux
1.4
1.2
1.0
0.8
0.6
0.4
0.2
1726
1728
1730
1732
1734
1736
43 FeIV
41 FeIV
34 Ni IV
35 FeIV
35 FeIV
35 S IV
33 FeIV
36 FeIV
40 FeIV
41 FeIV
41 FeIV
39 FeIV
38 S IV
Flux
1.4
1.2
1.0
0.8
0.6
0.4
0.2
1738
1740
1742
1744
1746

B IUE spectra

The complete IUE spectral range (red) of HD 127493 compared with the fully line-blanketed synthetic spectrum using $T_{\rm eff} = 42484\,{\rm K}$, $\log g = 5.6$ and $\log N({\rm He})/N({\rm H}) = 0.62$, as well as a radial velocity of $-21\,{\rm km/s}$.

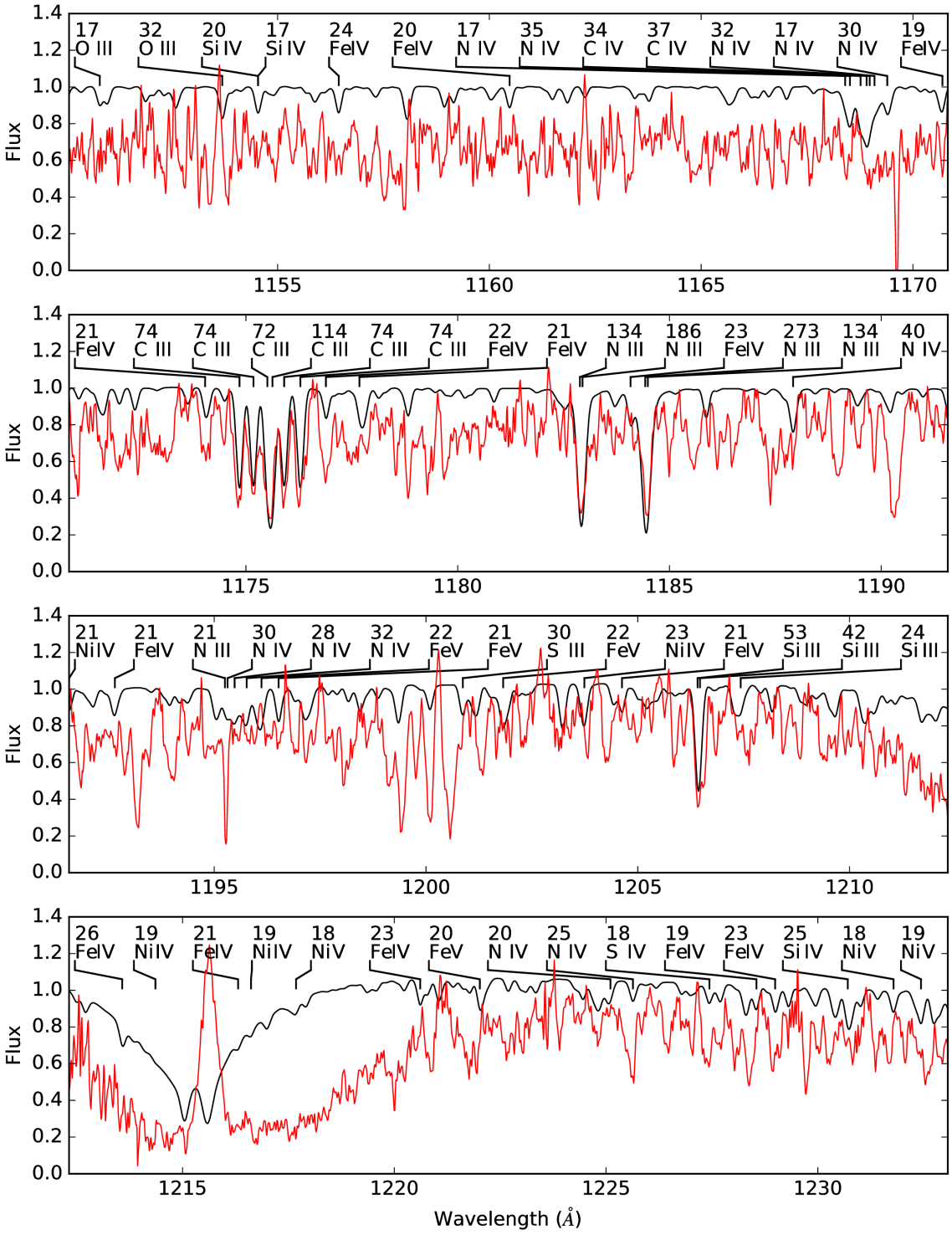

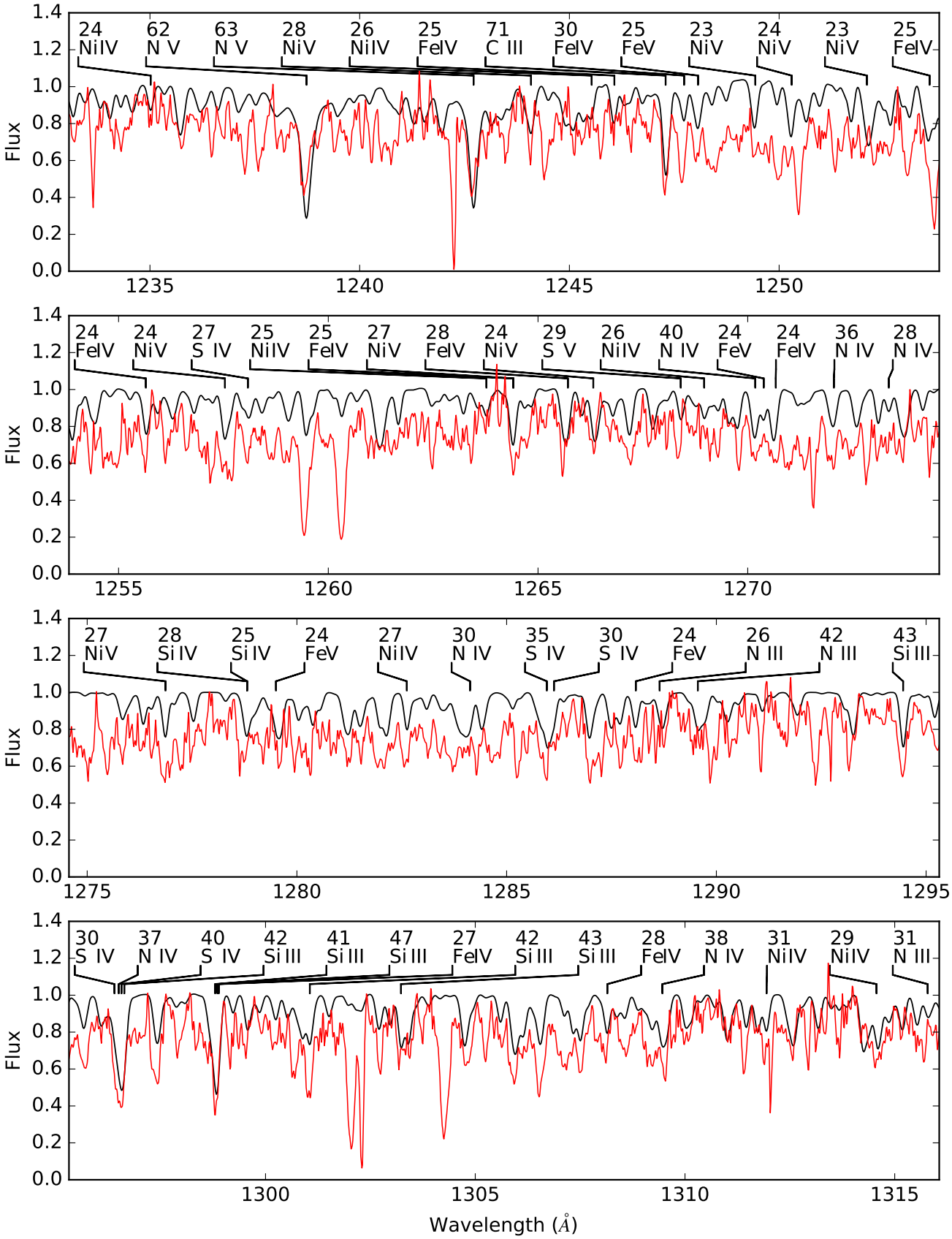
24 NiIV
62 N V
63 N V
28 NiV
26 NiIV
25 FeIV
71 C III
30 FeIV
25 FeV
23 NiV
24 NiV
23 NiV
25 FeIV
24 FeIV
24 NiV
27 S IV
25 NiIV
25 FeIV
27 NiV
28 FeIV
24 NiV
29 S V
26 NiIV
40 N IV
24 FeV
24 FeIV
36 N IV
28 N IV
27 NiV
28 Si IV
25 Si IV
24 FeV
27 NiIV
30 N IV
35 S IV
30 S IV
24 FeV
26 N III
42 N III
43 Si III
30 S IV
37 N IV
40 S IV
42 Si III
41 Si III
47 Si III
27 FeIV
42 Si III
43 Si III
28 FeIV
38 N IV
31 NiIV
29 NiIV
31 N III
Flux
Wavelength (Å)

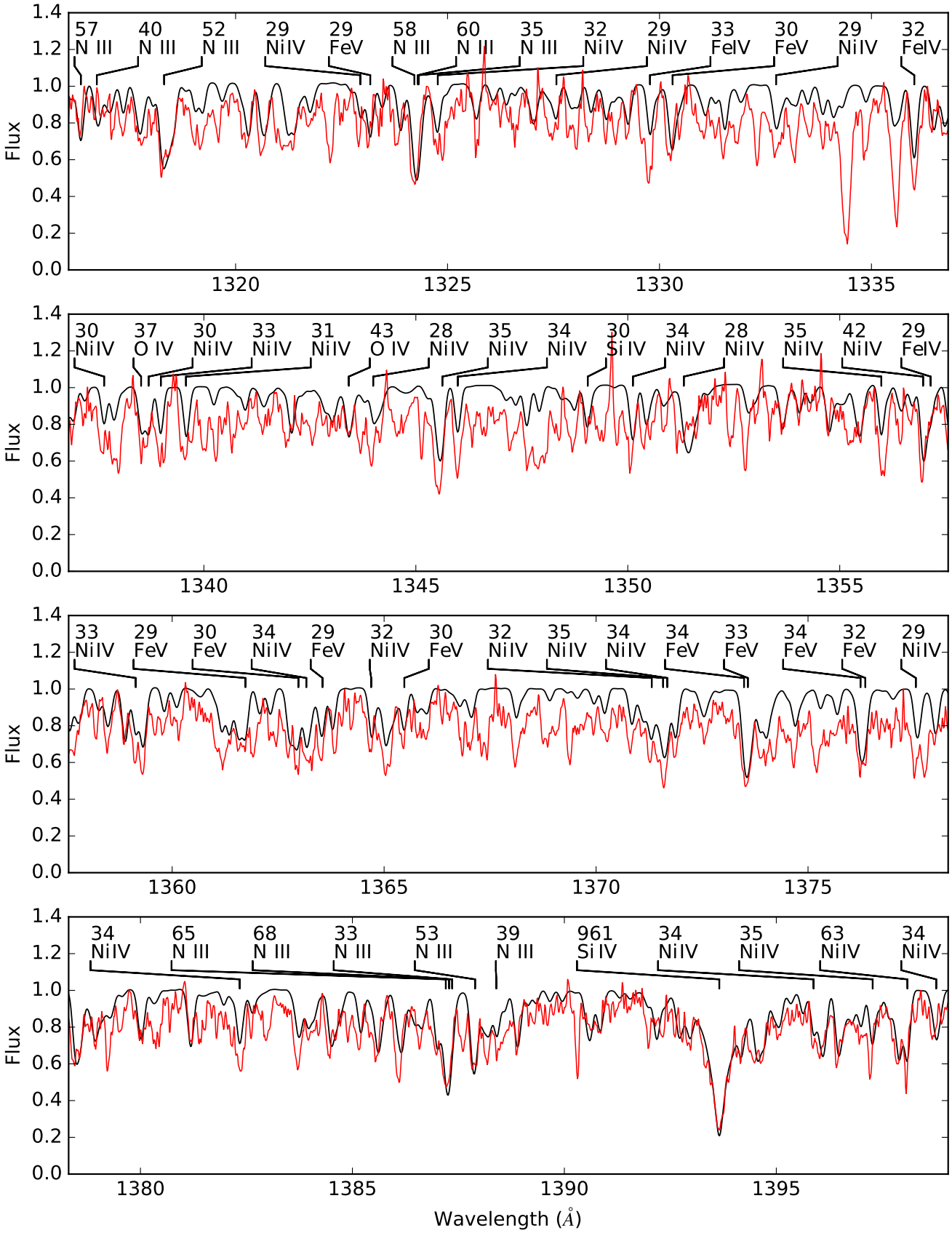
57 N III
40 N III
52 N III
29 NiIV
29 FeV
58 N III
60 N III
35 N III
32 NiIV
29 NiIV
33 FeIV
30 FeV
29 NiIV
32 FeIV
30 NiIV
37 O IV
30 NiIV
33 NiIV
31 NiIV
43 O IV
28 NiIV
35 NiIV
34 NiIV
30 SiIV
34 NiIV
28 NiIV
35 NiIV
42 NiIV
29 FeIV
33 NiIV
29 FeV
30 FeV
34 NiIV
29 FeV
32 NiIV
30 FeV
32 NiIV
35 NiIV
34 NiIV
34 FeV
33 FeV
34 FeV
32 FeV
29 NiIV
34 NiIV
65 N III
68 N III
33 N III
53 N III
39 N III
961 SiIV
34 NiIV
35 NiIV
63 NiIV
34 NiIV
Flux
Wavelength (Å)

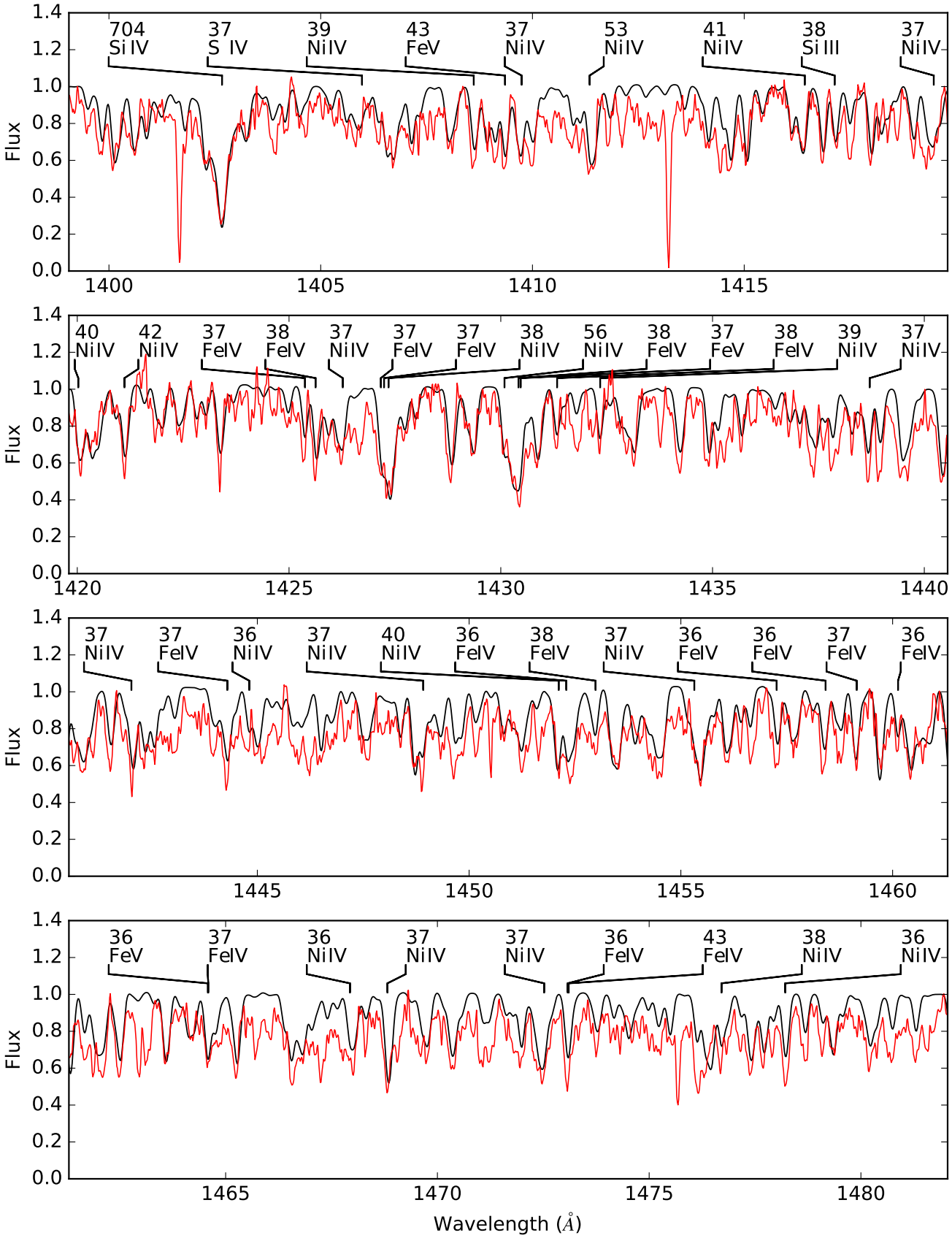
704 Si IV
37 S IV
39 Ni IV
43 Fe V
37 Ni IV
53 Ni IV
41 Ni IV
38 Si III
37 Ni IV
40 Ni IV
42 Ni IV
37 Fe IV
38 Fe IV
37 Ni IV
37 Fe IV
37 Fe IV
38 Ni IV
56 Ni IV
38 Fe IV
37 Fe V
38 Fe IV
39 Ni IV
37 Ni IV
37 Ni IV
37 Fe IV
36 Ni IV
37 Ni IV
40 Ni IV
36 Fe IV
38 Fe IV
37 Ni IV
36 Fe IV
36 Fe IV
37 Fe IV
36 Fe IV
36 Fe V
37 Fe IV
36 Ni IV
37 Ni IV
37 Ni IV
36 Fe IV
43 Fe IV
38 Ni IV
36 Ni IV
Flux
Wavelength (Å)

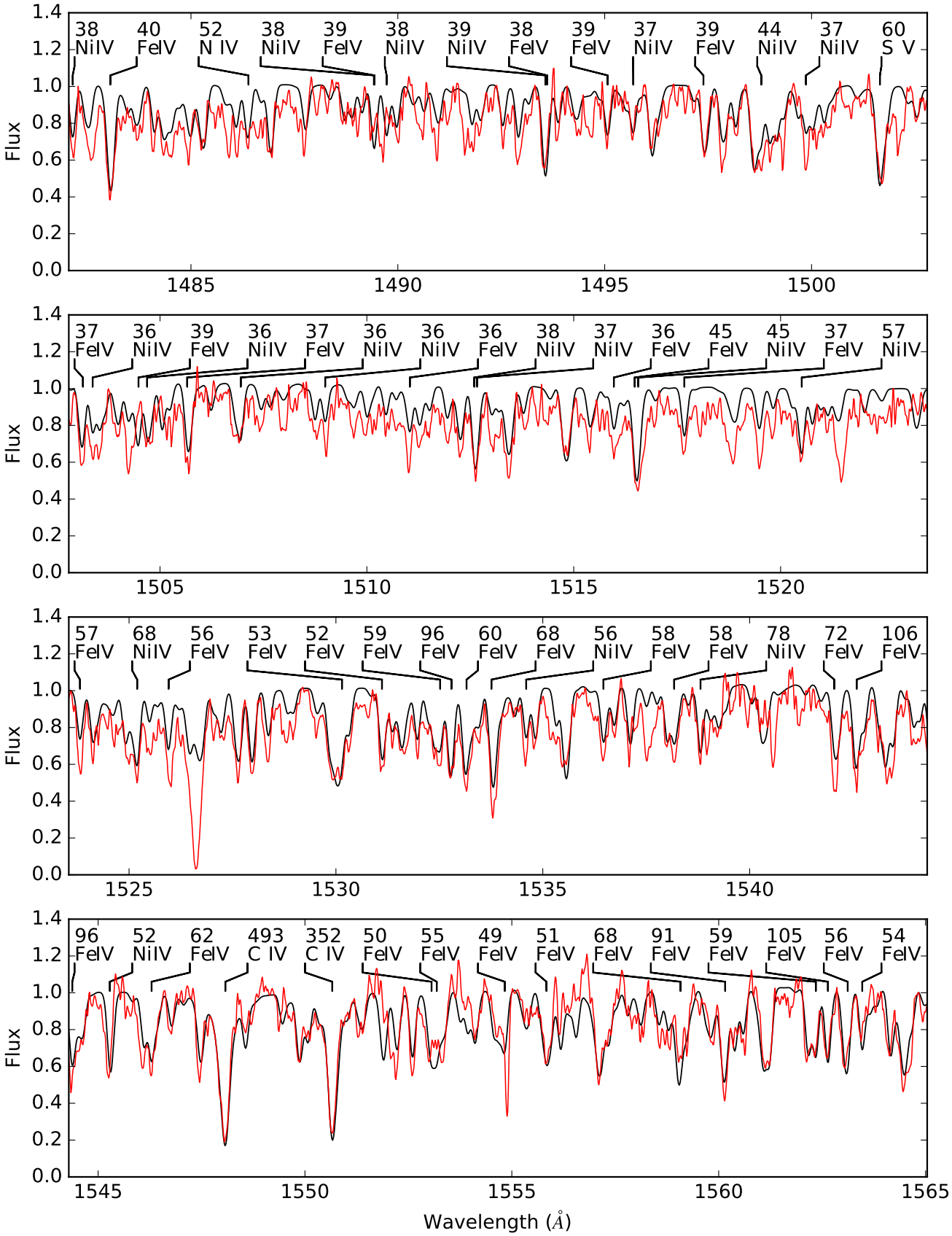
38 NiIV
40 FeIV
52 N IV
38 NiIV
39 FeIV
38 NiIV
39 NiIV
38 FeIV
39 FeIV
37 NiIV
39 FeIV
44 NiIV
37 NiIV
60 S V
37 FeIV
36 NiIV
39 FeIV
36 NiIV
37 FeIV
36 NiIV
36 NiIV
36 FeIV
38 NiIV
37 NiIV
36 FeIV
45 FeIV
45 NiIV
37 FeIV
57 NiIV
57 FeIV
68 NiIV
56 FeIV
53 FeIV
52 FeIV
59 FeIV
96 FeIV
60 FeIV
68 FeIV
56 NiIV
58 FeIV
58 FeIV
78 NiIV
72 FeIV
106 FeIV
96 FeIV
52 NiIV
62 FeIV
493 C IV
352 C IV
50 FeIV
55 FeIV
49 FeIV
51 FeIV
68 FeIV
91 FeIV
59 FeIV
105 FeIV
56 FeIV
54 FeIV
Flux
Wavelength (Å)

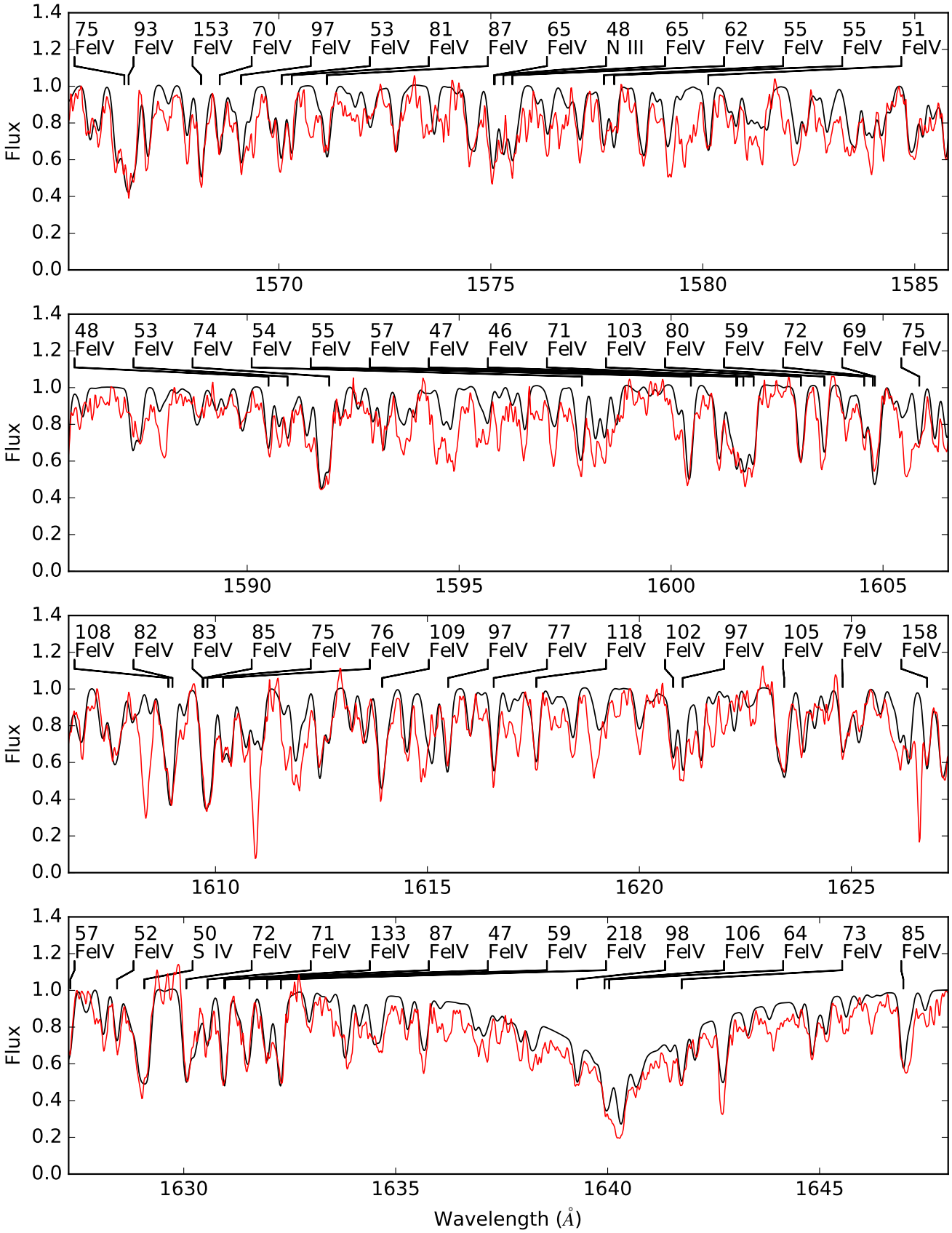
75 FeIV
93 FeIV
153 FeIV
70 FeIV
97 FeIV
53 FeIV
81 FeIV
87 FeIV
65 FeIV
48 N III
65 FeIV
62 FeIV
55 FeIV
55 FeIV
51 FeIV
48 FeIV
53 FeIV
74 FeIV
54 FeIV
55 FeIV
57 FeIV
47 FeIV
46 FeIV
71 FeIV
103 FeIV
80 FeIV
59 FeIV
72 FeIV
69 FeIV
75 FeIV
108 FeIV
82 FeIV
83 FeIV
85 FeIV
75 FeIV
76 FeIV
109 FeIV
97 FeIV
77 FeIV
118 FeIV
102 FeIV
97 FeIV
105 FeIV
79 FeIV
158 FeIV
57 FeIV
52 FeIV
50 S IV
72 FeIV
71 FeIV
133 FeIV
87 FeIV
47 FeIV
59 FeIV
218 FeIV
98 FeIV
106 FeIV
64 FeIV
73 FeIV
85 FeIV
Flux
Wavelength (Å)

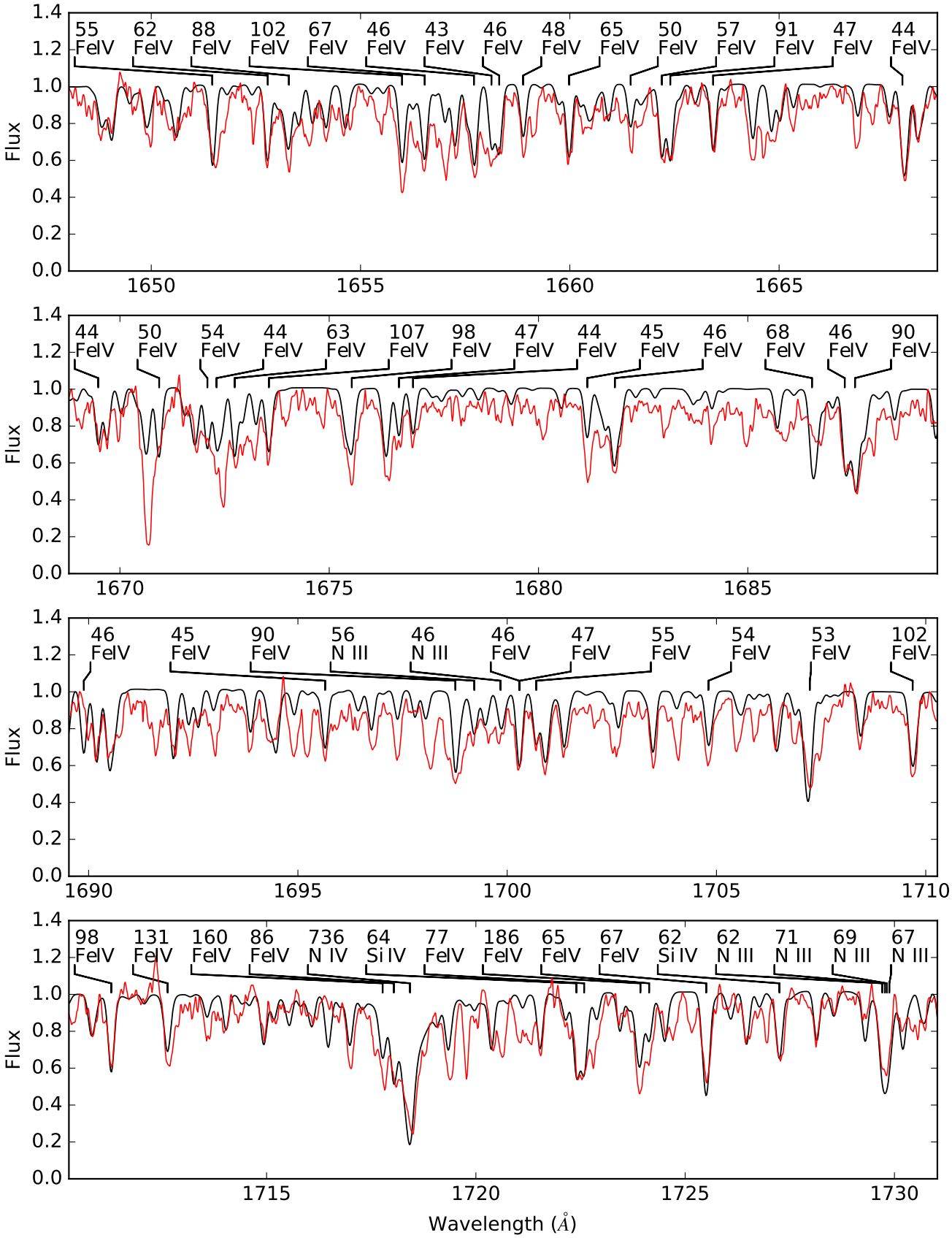
55 FeIV
62 FeIV
88 FeIV
102 FeIV
67 FeIV
46 FeIV
43 FeIV
46 FeIV
48 FeIV
65 FeIV
50 FeIV
57 FeIV
91 FeIV
47 FeIV
44 FeIV
44 FeIV
50 FeIV
54 FeIV
44 FeIV
63 FeIV
107 FeIV
98 FeIV
47 FeIV
44 FeIV
45 FeIV
46 FeIV
68 FeIV
46 FeIV
90 FeIV
46 FeIV
45 FeIV
90 FeIV
56 N III
46 N III
46 FeIV
47 FeIV
55 FeIV
54 FeIV
53 FeIV
102 FeIV
98 FeIV
131 FeIV
160 FeIV
86 FeIV
736 N IV
64 Si IV
77 FeIV
186 FeIV
65 FeIV
67 FeIV
62 Si IV
62 N III
71 N III
69 N III
67 N III
Flux
Wavelength (Å)

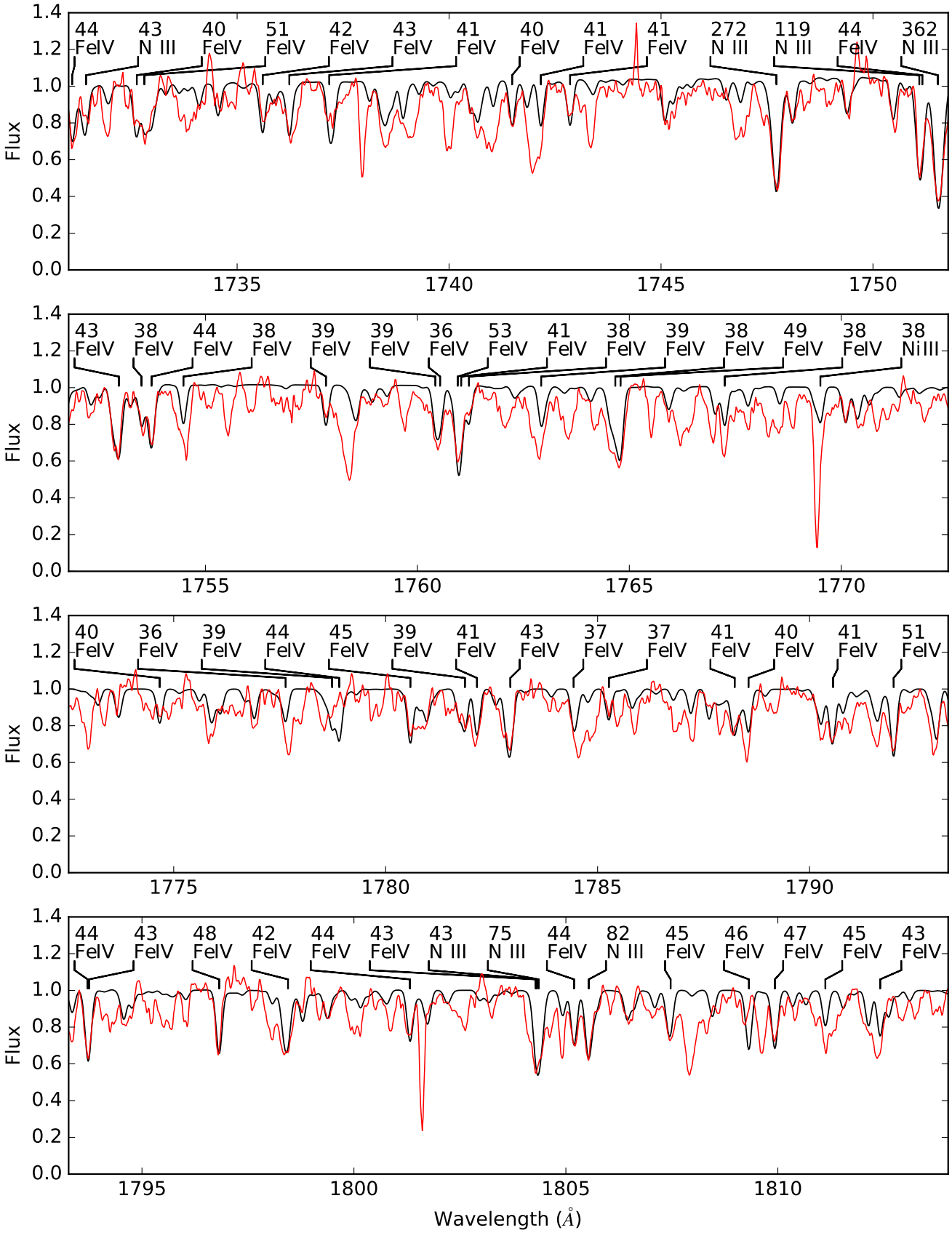
44 FeIV
43 N III
40 FeIV
51 FeIV
42 FeIV
43 FeIV
41 FeIV
40 FeIV
41 FeIV
41 FeIV
272 N III
119 N III
44 FeIV
362 N III
43 FeIV
38 FeIV
44 FeIV
38 FeIV
39 FeIV
39 FeIV
36 FeIV
53 FeIV
41 FeIV
38 FeIV
39 FeIV
38 FeIV
49 FeIV
38 FeIV
38 NiIII
40 FeIV
36 FeIV
39 FeIV
44 FeIV
45 FeIV
39 FeIV
41 FeIV
43 FeIV
37 FeIV
37 FeIV
41 FeIV
40 FeIV
41 FeIV
51 FeIV
44 FeIV
43 FeIV
48 FeIV
42 FeIV
44 FeIV
43 FeIV
43 N III
75 N III
44 FeIV
82 N III
45 FeIV
46 FeIV
47 FeIV
45 FeIV
43 FeIV
Flux
Wavelength (Å)

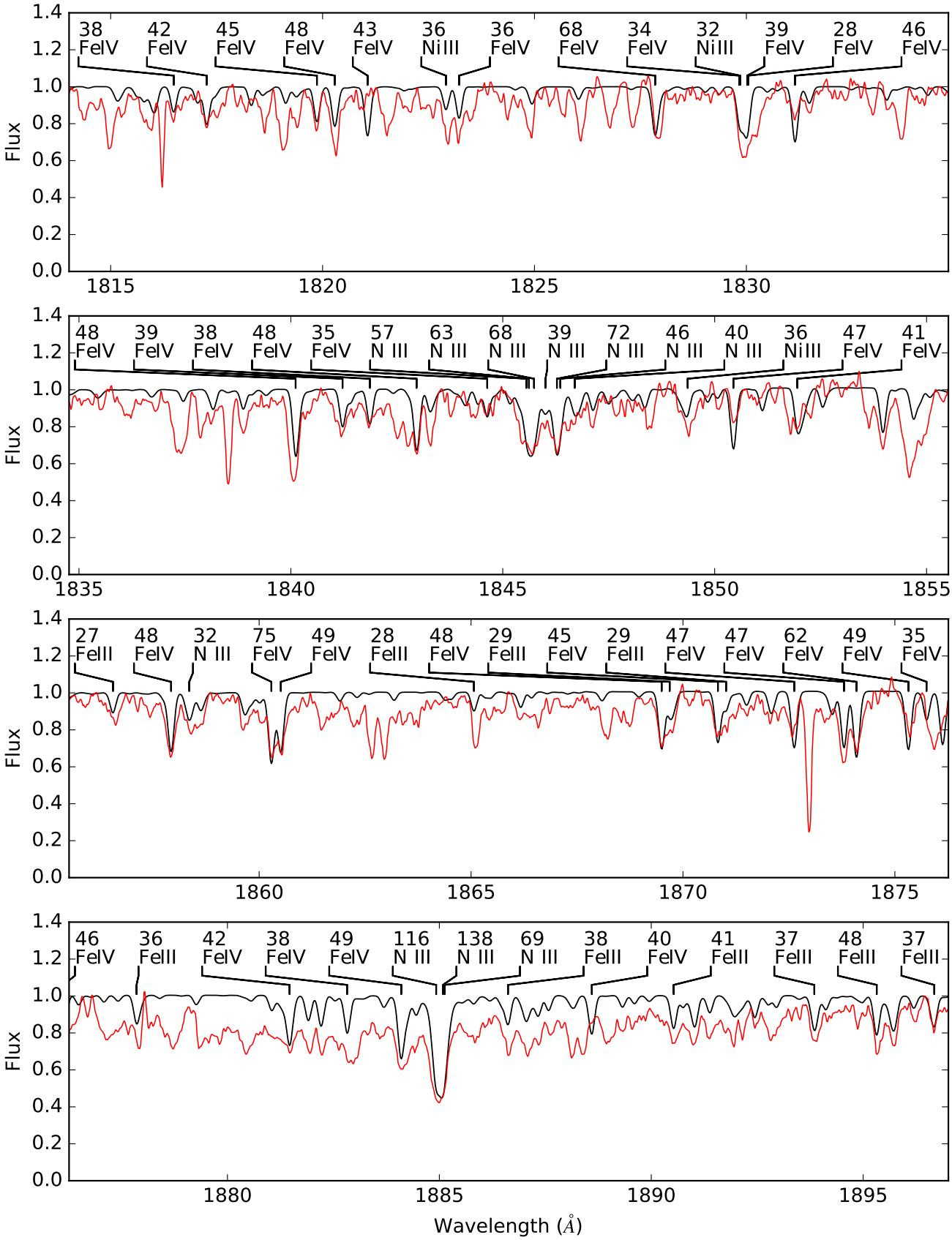
38 FeIV
42 FeIV
45 FeIV
48 FeIV
43 FeIV
36 NiIII
36 FeIV
68 FeIV
34 FeIV
32 NiIII
39 FeIV
28 FeIV
46 FeIV
48 FeIV
39 FeIV
38 FeIV
48 FeIV
35 FeIV
57 N III
63 N III
68 N III
39 N III
72 N III
46 N III
40 N III
36 NiIII
47 FeIV
41 FeIV
27 FeIII
48 FeIV
32 N III
75 FeIV
49 FeIV
28 FeIII
48 FeIV
29 FeIII
45 FeIV
29 FeIII
47 FeIV
47 FeIV
62 FeIV
49 FeIV
35 FeIV
46 FeIV
36 FeIII
42 FeIV
38 FeIV
49 FeIV
116 N III
138 N III
69 N III
38 FeIII
40 FeIV
41 FeIII
37 FeIII
48 FeIII
37 FeIII
Flux
Wavelength (Å)

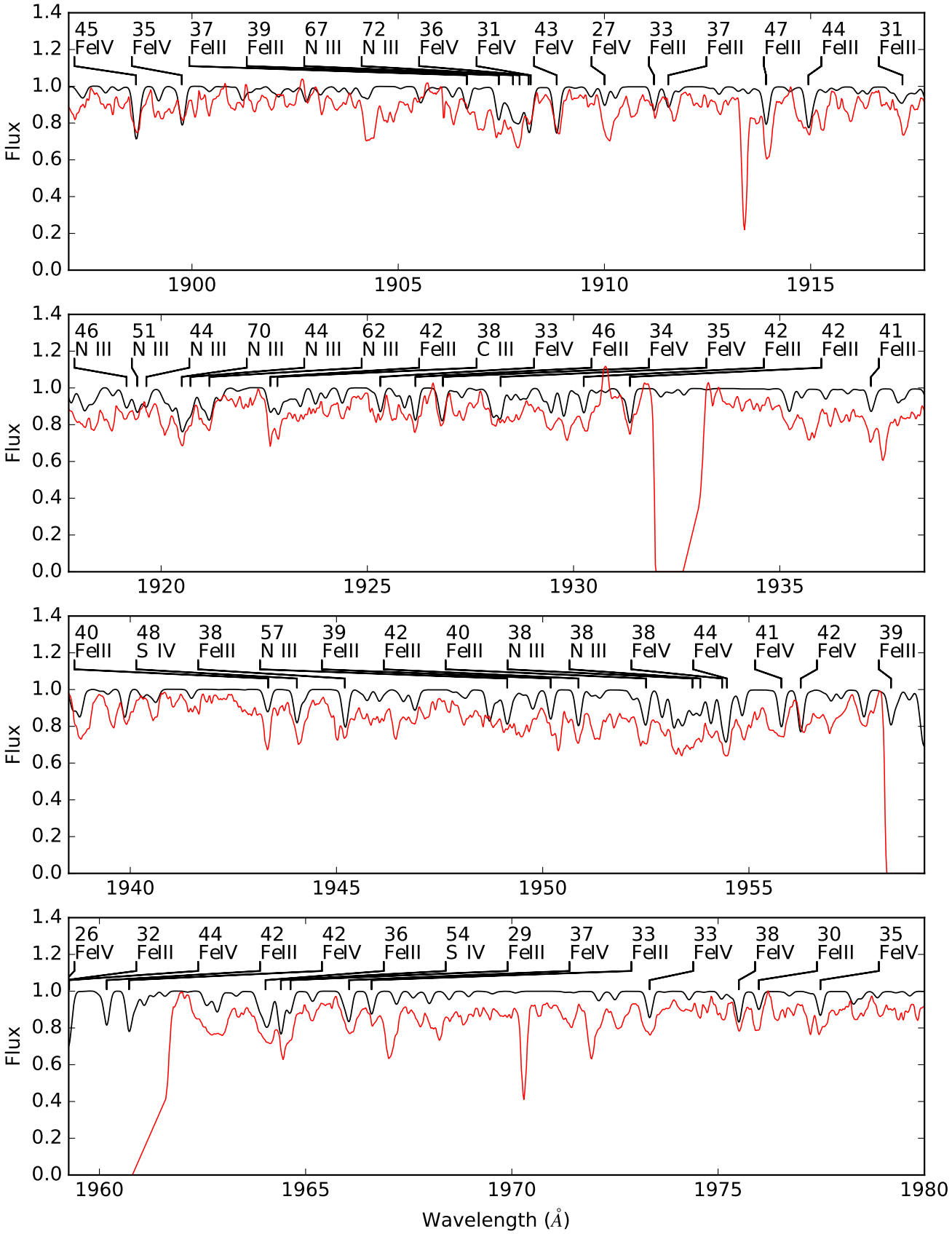
45 FeIV
35 FeIV
37 FeIII
39 FeIII
67 N III
72 N III
36 FeIV
31 FeIV
43 FeIV
27 FeIV
33 FeIII
37 FeIII
47 FeIII
44 FeIII
31 FeIII
46 N III
51 N III
44 N III
70 N III
44 N III
62 N III
42 FeIII
38 C III
33 FeIV
46 FeIII
34 FeIV
35 FeIV
42 FeIII
42 FeIII
41 FeIII
40 FeIII
48 S IV
38 FeIII
57 N III
39 FeIII
42 FeIII
40 FeIII
38 N III
38 N III
38 FeIV
44 FeIV
41 FeIV
42 FeIV
39 FeIII
26 FeIV
32 FeIII
44 FeIV
42 FeIII
42 FeIV
36 FeIII
54 S IV
29 FeIII
37 FeIV
33 FeIII
33 FeIV
38 FeIV
30 FeIII
35 FeIV
Flux
Wavelength (Å)

C FEROS spectra

The complete FEROS spectral range (red) of HD 127493 compared with the fully line-blanketed synthetic spectrum using $T_{\rm eff} = 42484\,{\rm K}$, $\log g = 5.6$ and $\log N({\rm He})/N({\rm H}) = 0.62$, as well as a radial velocity of $-16\,{\rm km/s}$.

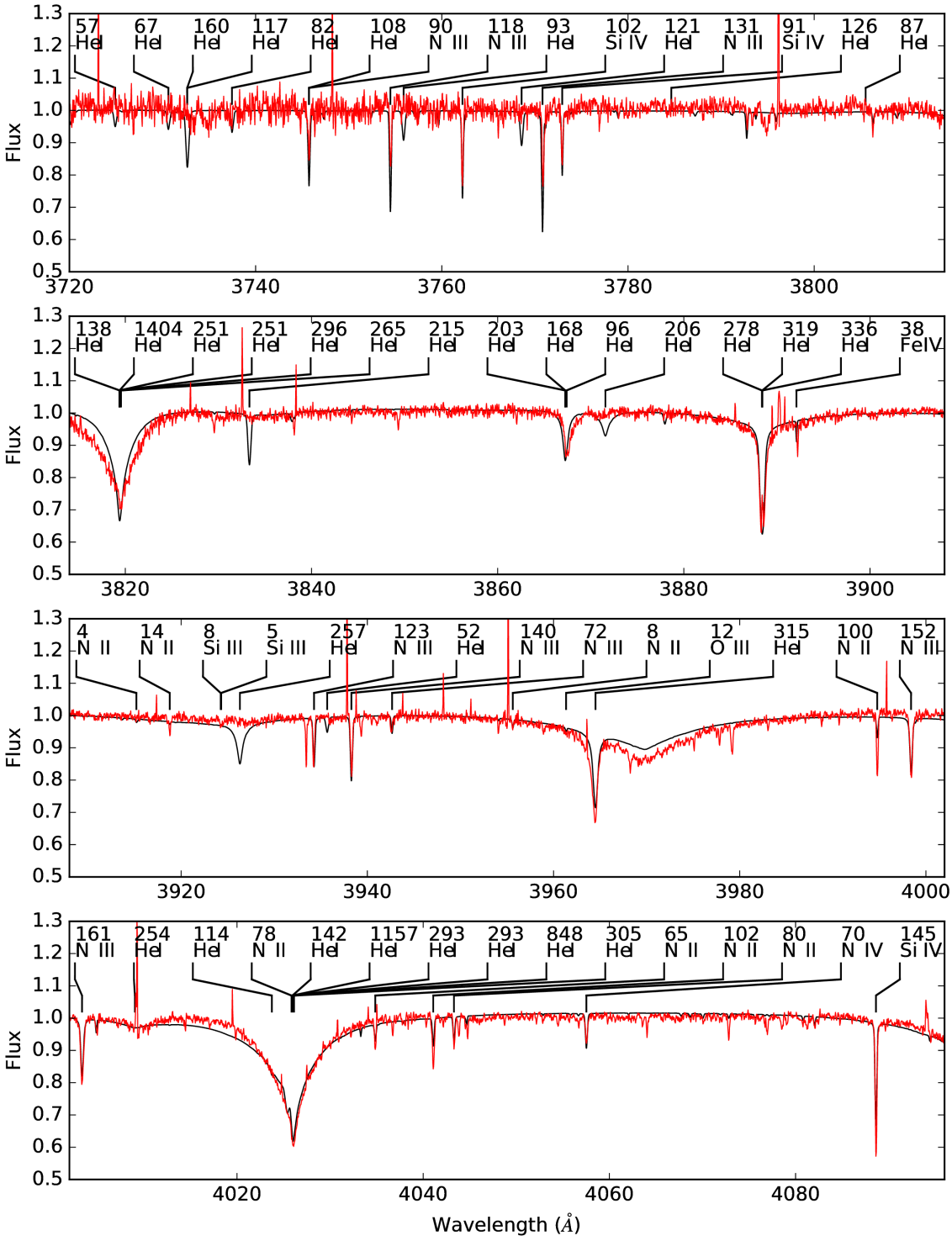

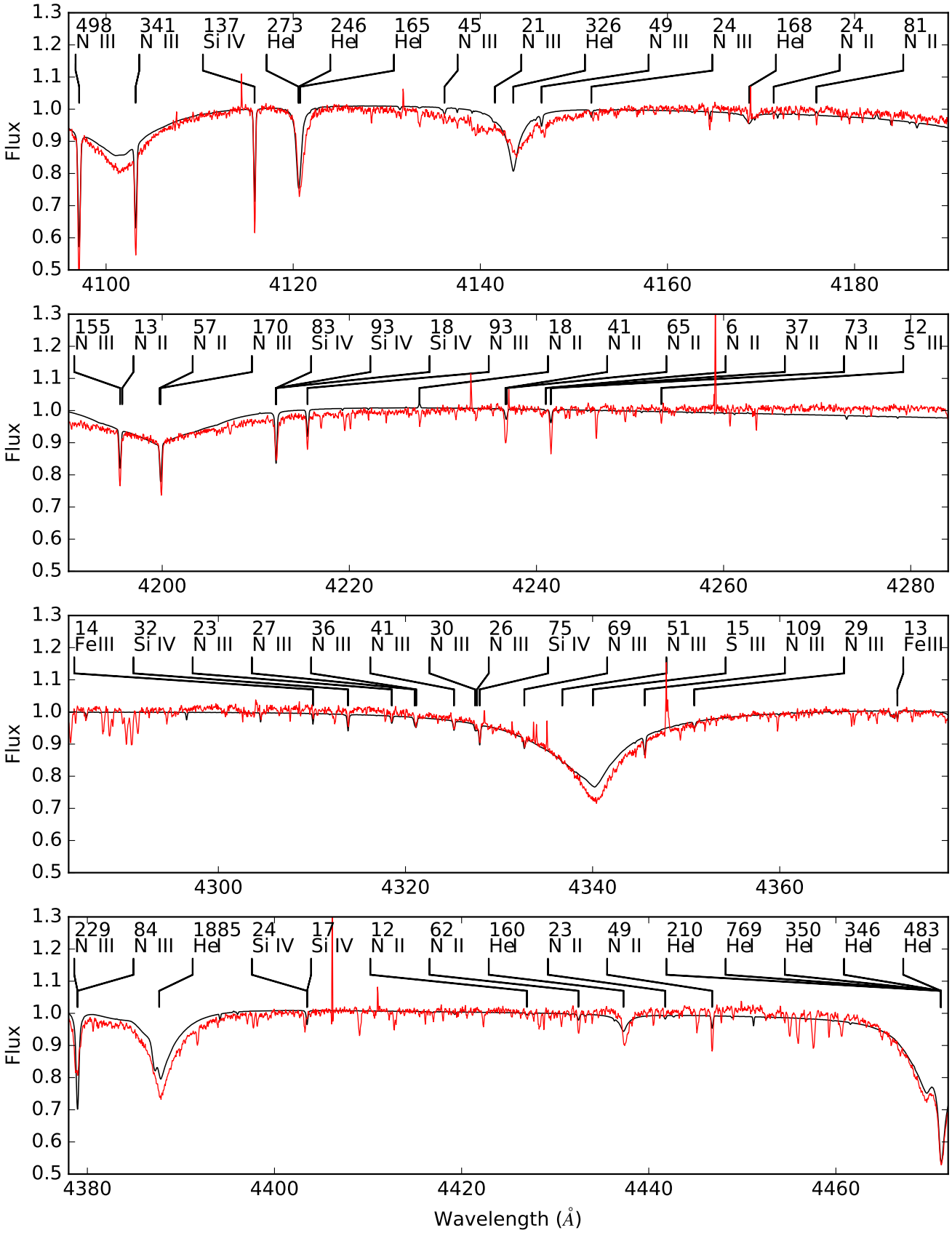
498 N III
341 N III
137 Si IV
273 HeI
246 HeI
165 HeI
45 N III
21 N III
326 HeI
49 N III
24 N III
168 HeI
24 N II
81 N II
155 N III
13 N II
57 N II
170 N III
83 Si IV
93 Si IV
18 Si IV
93 N III
18 N II
41 N II
65 N II
6 N II
37 N II
73 N II
12 S III
14 FeIII
32 Si IV
23 N III
27 N III
36 N III
41 N III
30 N III
26 N III
75 Si IV
69 N III
51 N III
15 S III
109 N III
29 N III
13 FeIII
229 N III
84 N III
1885 HeI
24 Si IV
17 Si IV
12 N II
62 N II
160 HeI
23 N II
49 N II
210 HeI
769 HeI
350 HeI
346 HeI
483 HeI
Flux
Wavelength (Å)

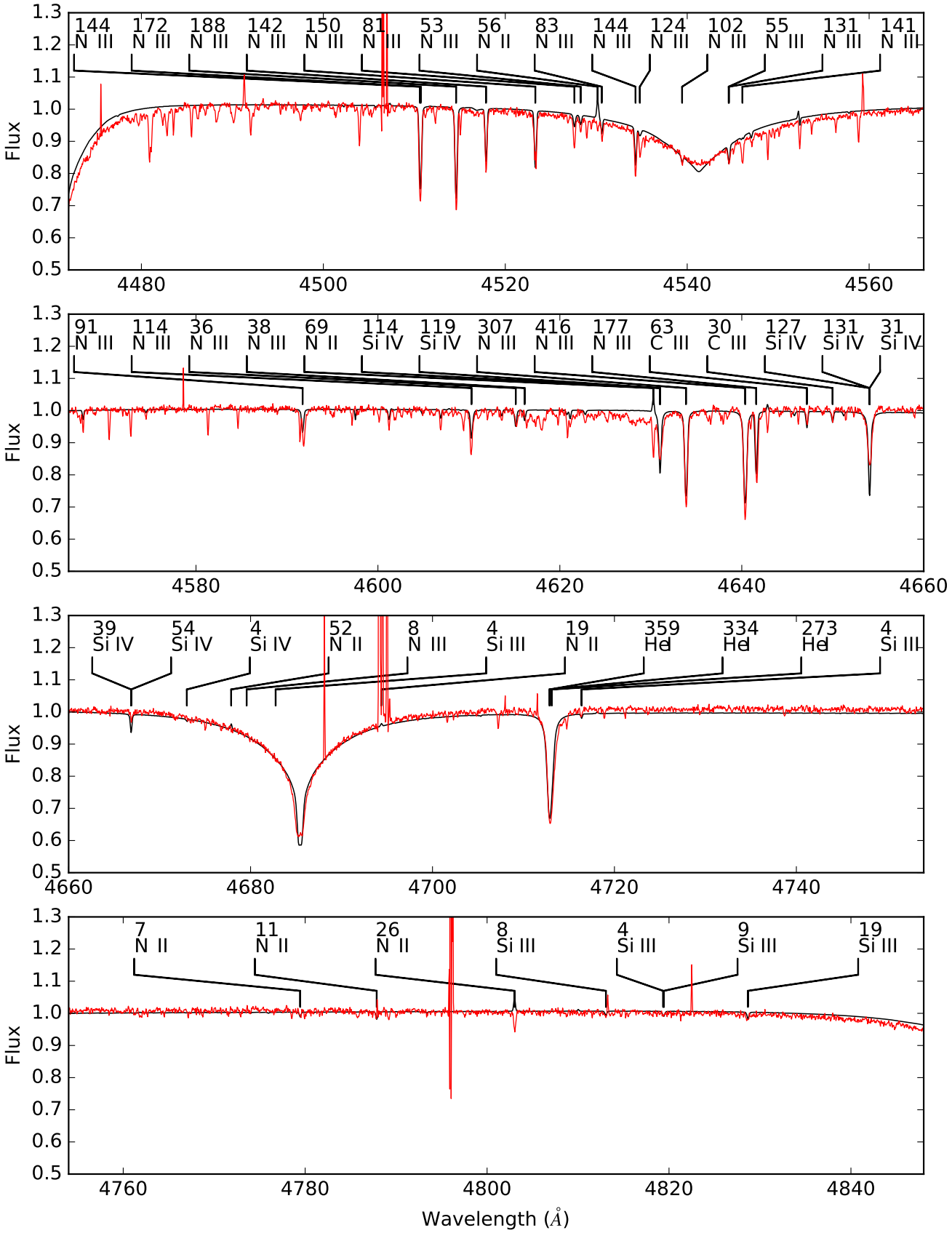
144 N III
172 N III
188 N III
142 N III
150 N III
81 N III
53 N III
56 N II
83 N III
144 N III
124 N III
102 N III
55 N III
131 N III
141 N III
91 N III
114 N III
36 N III
38 N III
69 N II
114 Si IV
119 Si IV
307 N III
416 N III
177 N III
63 C III
30 C III
127 Si IV
131 Si IV
31 Si IV
39 Si IV
54 Si IV
4 Si IV
52 N II
8 N III
4 Si III
19 N II
359 HeI
334 HeI
273 HeI
4 Si III
7 N II
11 N II
26 N II
8 Si III
4 Si III
9 Si III
19 Si III
Flux
Wavelength (Å)

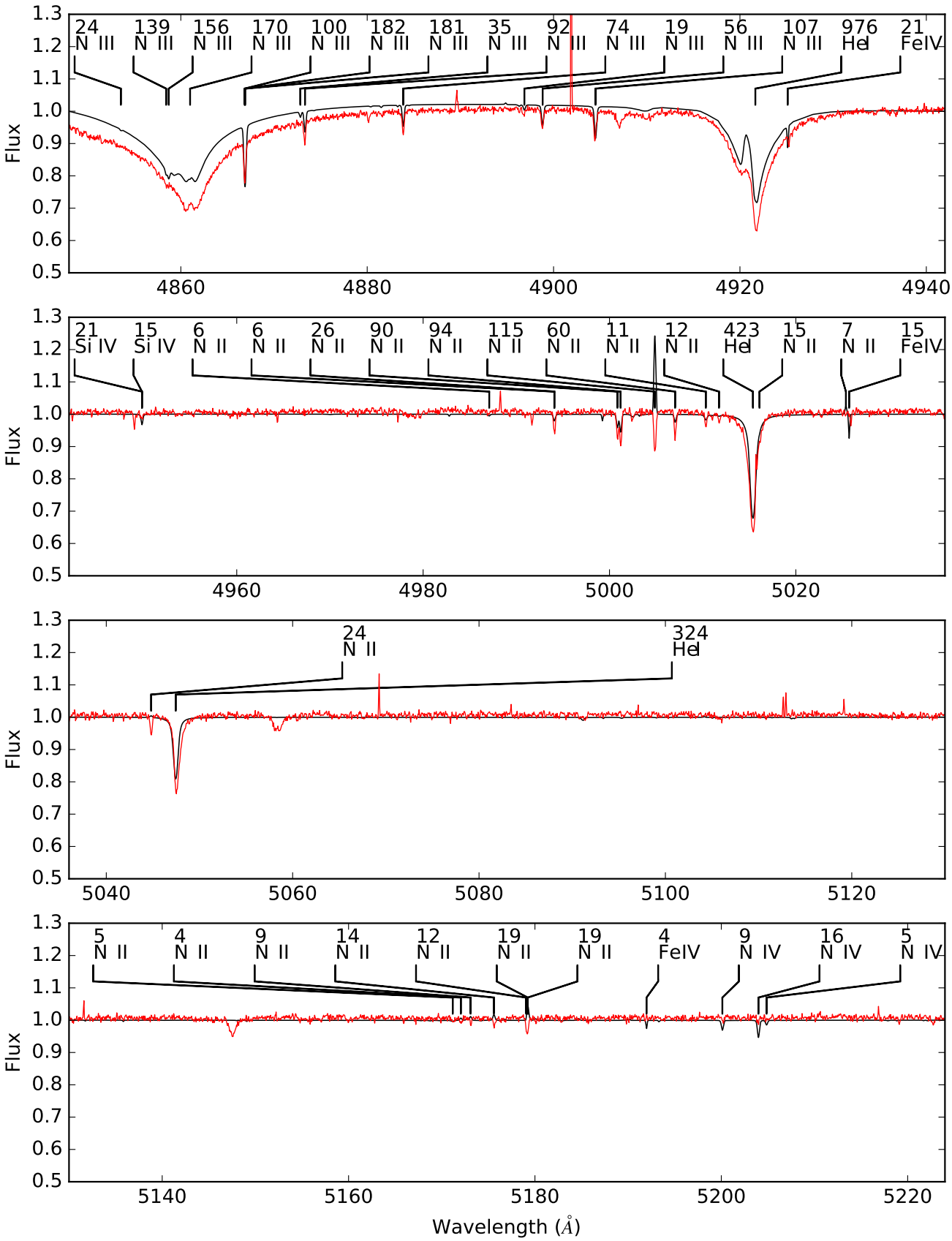
24 N III
139 N III
156 N III
170 N III
100 N III
182 N III
181 N III
35 N III
92 N III
74 N III
19 N III
56 N III
107 N III
976 HeI
21 FeIV
21 Si IV
15 Si IV
6 N II
6 N II
26 N II
90 N II
94 N II
115 N II
60 N II
11 N II
12 N II
423 HeI
15 N II
7 N II
15 FeIV
24 N II
324 HeI
5 N II
4 N II
9 N II
14 N II
12 N II
19 N II
19 N II
4 FeIV
9 N IV
16 N IV
5 N IV
Flux
Wavelength (Å)

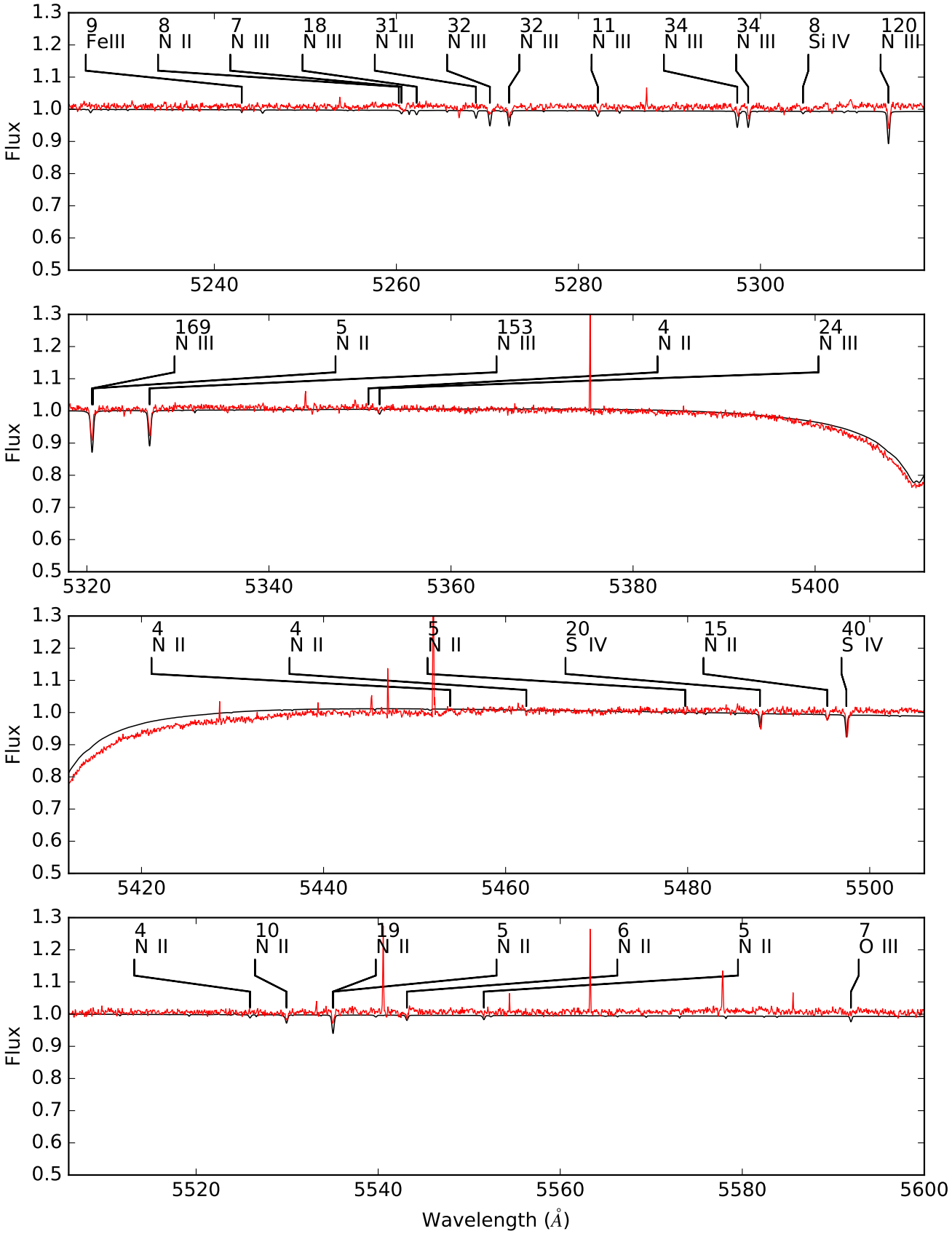
9 FeIII
8 N II
7 N III
18 N III
31 N III
32 N III
32 N III
11 N III
34 N III
34 N III
8 Si IV
120 N III
169 N III
5 N II
153 N III
4 N II
24 N III
4 N II
4 N II
5 N II
20 S IV
15 N II
40 S IV
4 N II
10 N II
19 N II
5 N II
6 N II
5 N II
7 O III
Flux
Wavelength (Å)

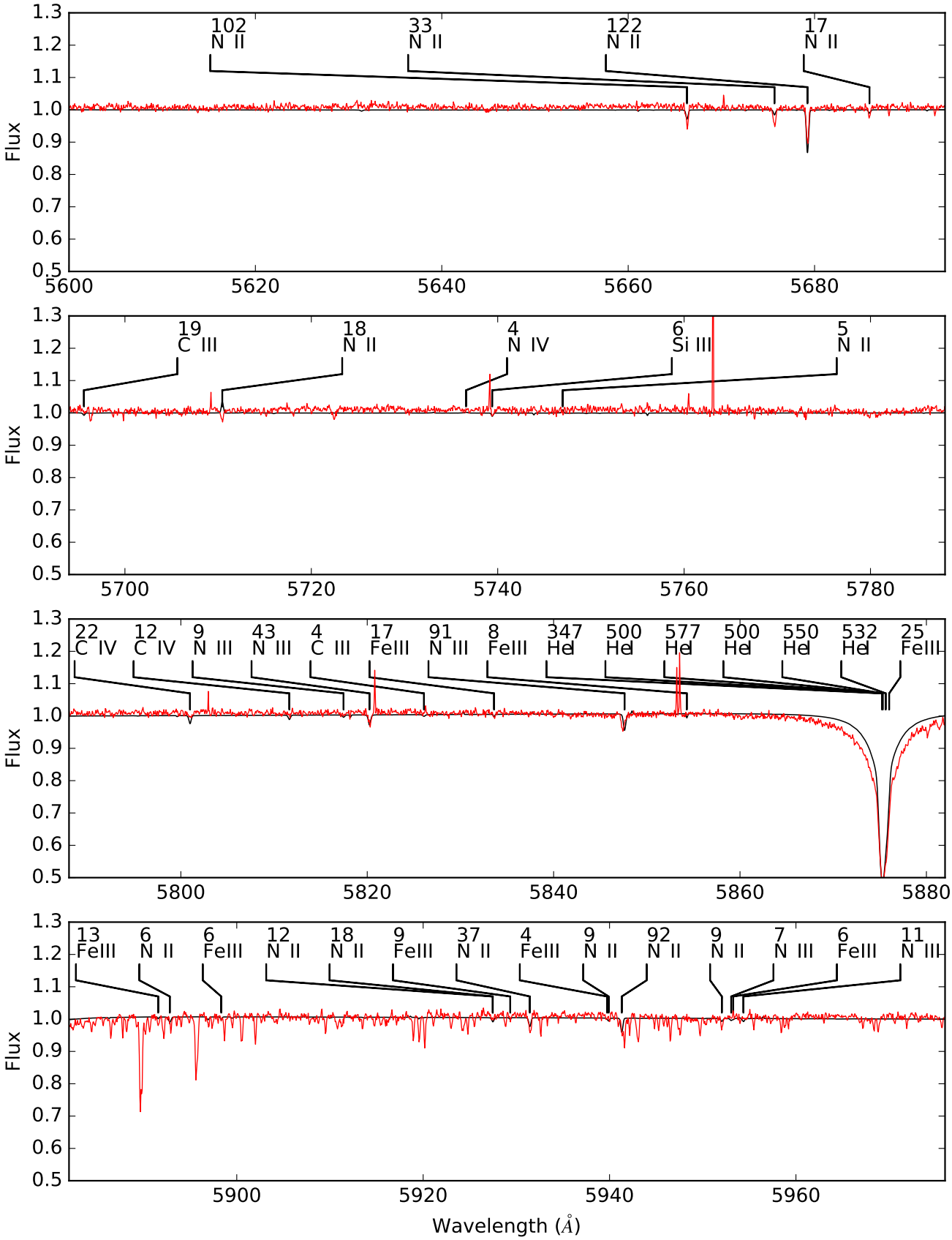
102 N II
33 N II
122 N II
17 N II
19 C III
18 N II
4 N IV
6 Si III
5 N II
22 C IV
12 C IV
9 N III
43 N III
4 C III
17 FeIII
91 N III
8 FeIII
347 HeI
500 HeI
577 HeI
500 HeI
550 HeI
532 HeI
25 FeIII
13 FeIII
6 N II
6 FeIII
12 N II
18 N II
9 FeIII
37 N II
4 FeIII
9 N II
92 N II
9 N II
7 N III
6 FeIII
11 N III
Flux
Wavelength (Å)

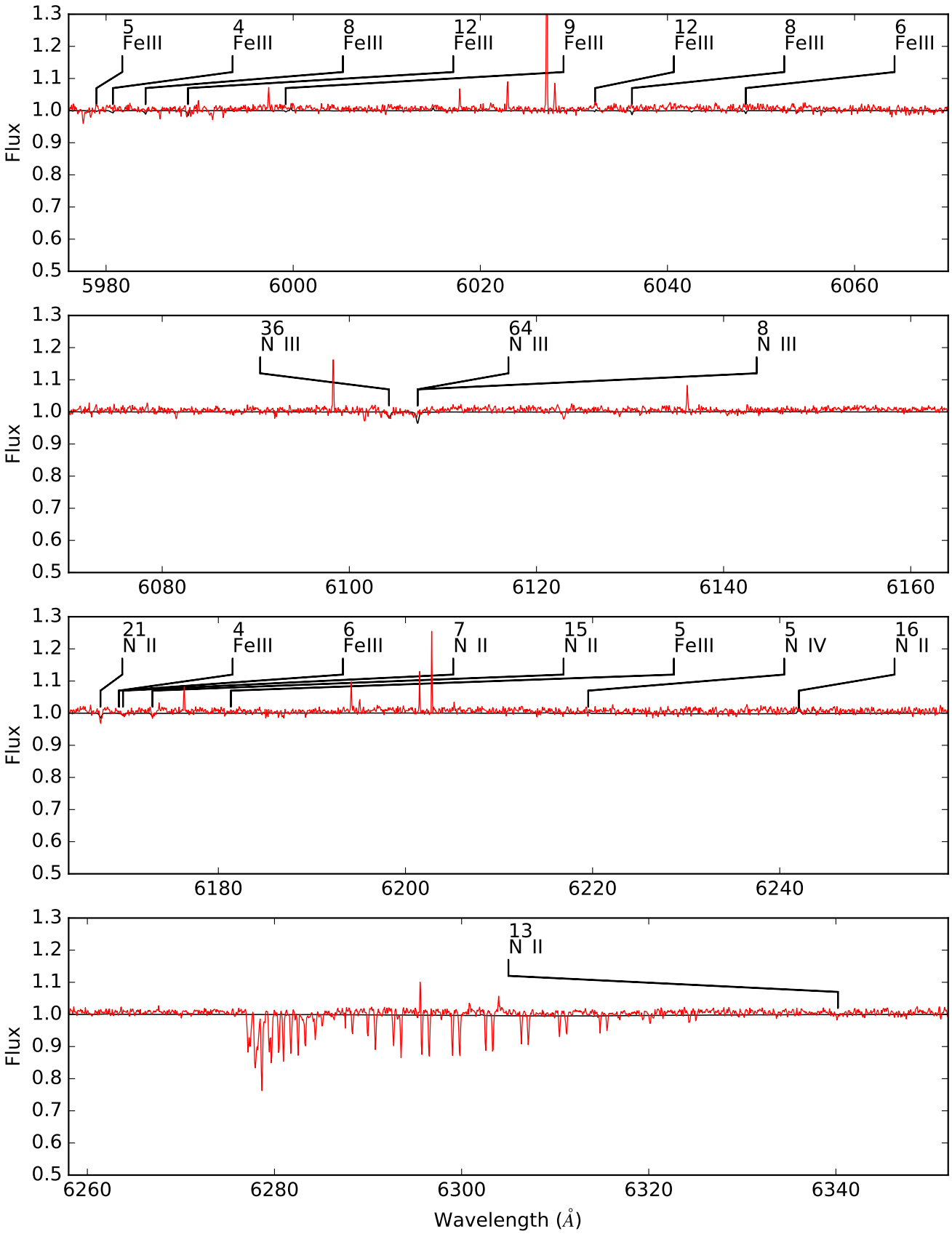
5 FeIII
4 FeIII
8 FeIII
12 FeIII
9 FeIII
12 FeIII
8 FeIII
6 FeIII
36 N III
64 N III
8 N III
21 N II
4 FeIII
6 FeIII
7 N II
15 N II
5 FeIII
5 N IV
16 N II
13 N II
Flux
Wavelength (Å)

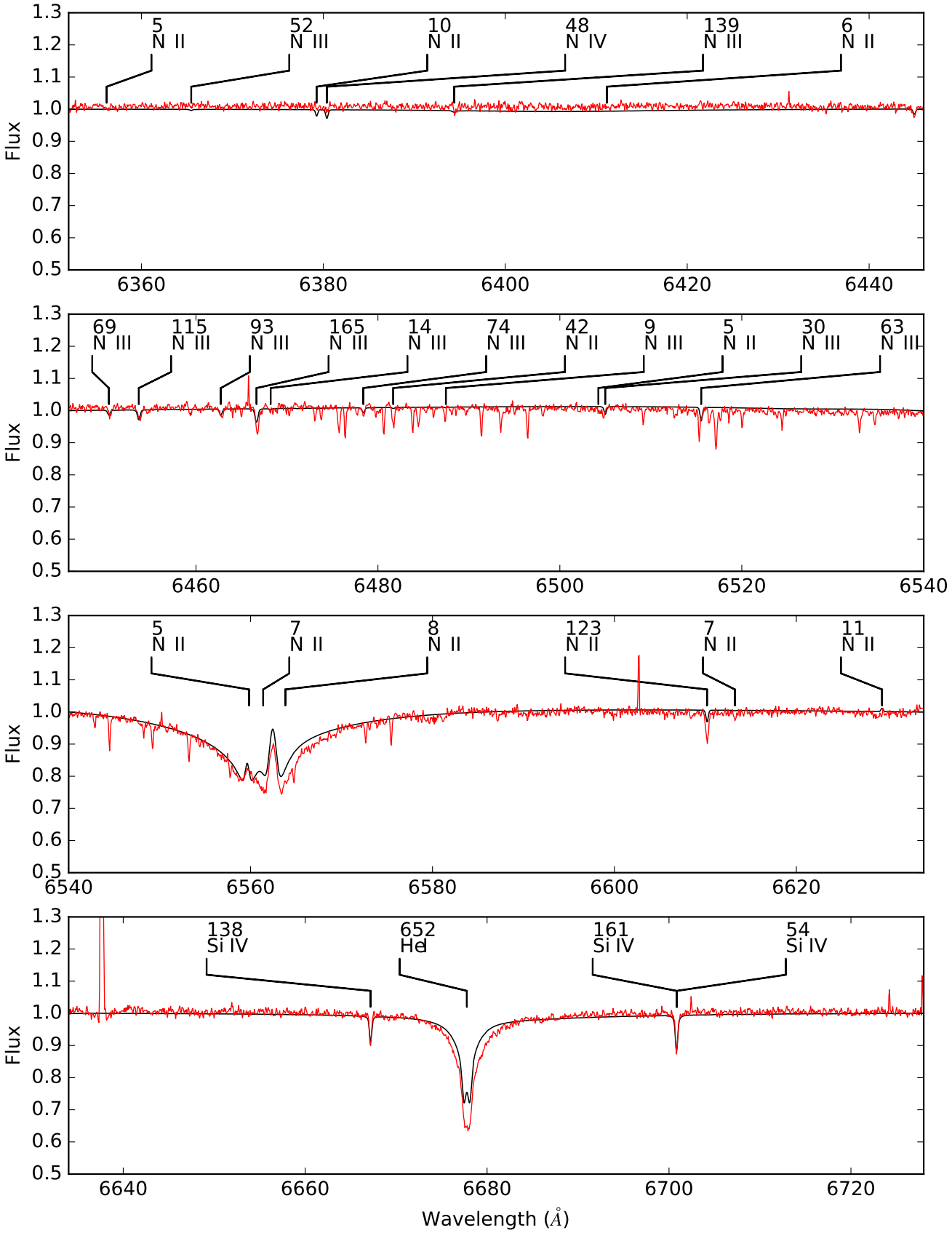
5
N II
52
N III
10
N II
48
N IV
139
N III
6
N II
69
N III
115
N III
93
N III
165
N III
14
N III
74
N III
42
N II
9
N III
5
N II
30
N III
63
N III
5
N II
7
N II
8
N II
123
N II
7
N II
11
N II
138
Si IV
652
HeI
161
Si IV
54
Si IV
Flux
Wavelength (Å)

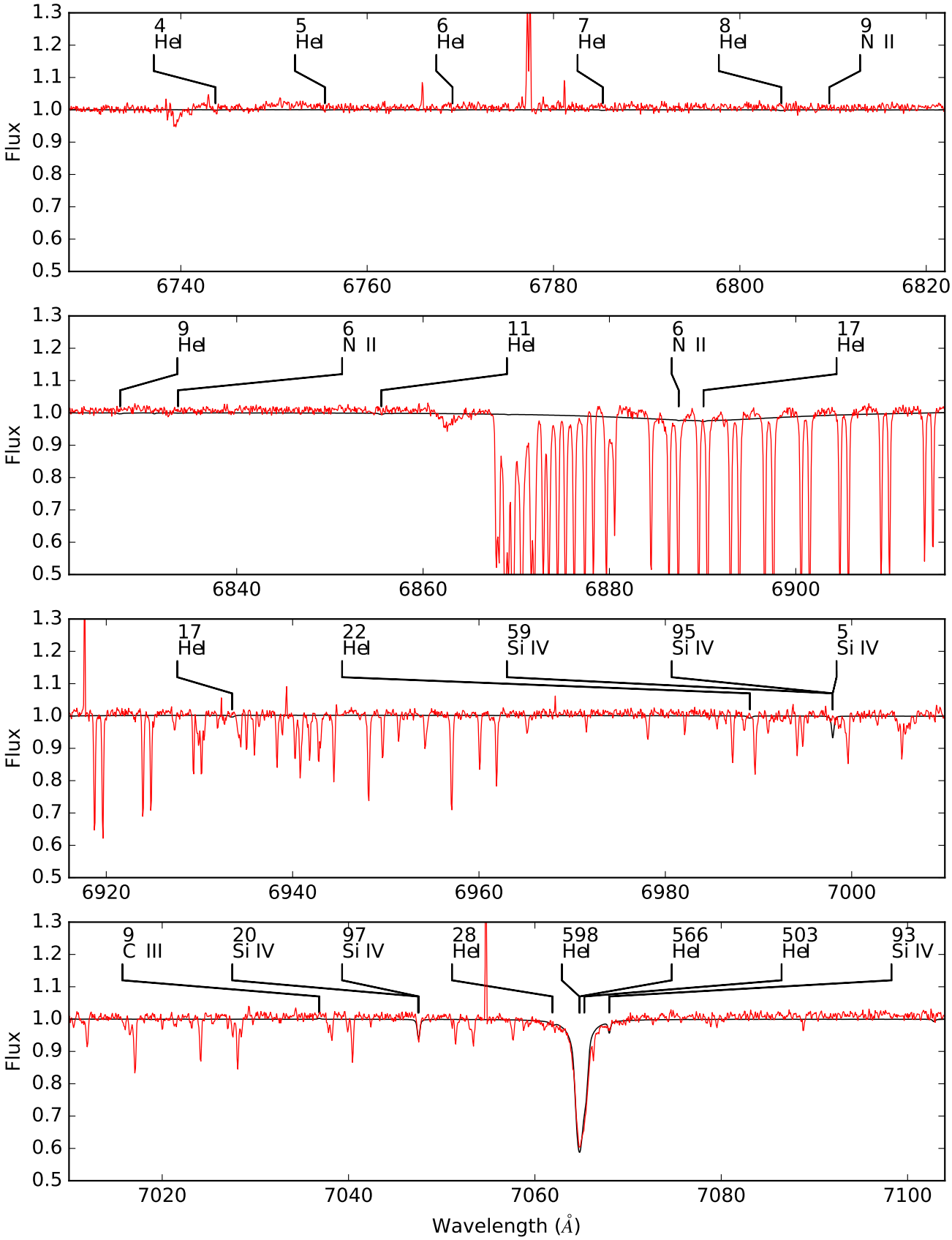
4 HeI
5 HeI
6 HeI
7 HeI
8 HeI
9 N II
9 HeI
6 N II
11 HeI
6 N II
17 HeI
17 HeI
22 HeI
59 Si IV
95 Si IV
5 Si IV
9 C III
20 Si IV
97 Si IV
28 HeI
598 HeI
566 HeI
503 HeI
93 Si IV
Flux
Wavelength (Å)

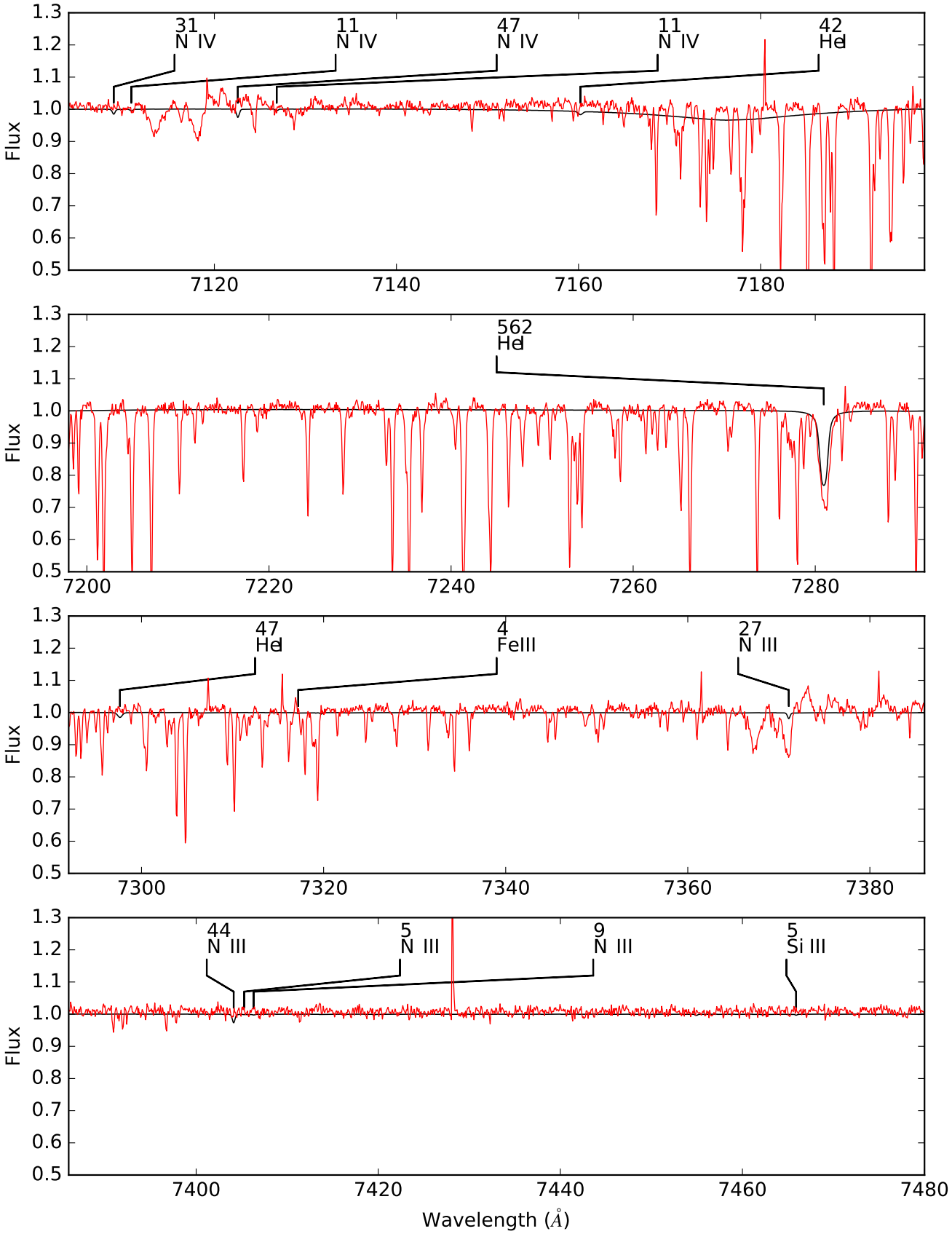
31
N IV
11
N IV
47
N IV
11
N IV
42
HeI
562
HeI
47
HeI
4
FeIII
27
N III
44
N III
5
N III
9
N III
5
Si III
Flux
Wavelength (Å)

D Line list for species analyzed from individual lines

The following tables list which lines were used for deriving the final metal abundances. Errors, when given, are purely statistical and have been determined by `SPAS` using the bootstrapping method. Values for v_{rot} and v_{rad} are not always complete, since some could not be fitted automatically and had to be adjusted by hand (e.g. for weak lines, lines with blends). Since the abundance of iron and nickel was determined by fitting several ranges including many lines and many strong iron and nickel lines exist in the UV range, they are not listed here. The upper limit for oxygen was estimated by visually comparing synthetic models that include oxygen at a fixed abundance with O IV 1338.61 Å, O IV 1342.99 Å and O IV 1343.51 Å in the observed UV spectra. The listed wavelengths are adopted from the NIST Atomic Spectra Database (ASD) (Kramida et al. 2015), preferring observed source wavelengths λ_{s} over theoretical ones if available. If multiple lines from the same ion were fitted at the same time, this is indicated by adding x "number of lines".

D.1 FEROS

Ion	λ_{s} (Å)	v_{rot} (km/s)	Δv_{rot} (km/s)	v_{rad} (km/s)	Δv_{rad} (km/s)
N II	4041.31	4.5	2.8	-16.6	0.3
N II	4236.91	0.0	4.3	-18.3	
N II	4241.78	0.0	2.6	-16.6	0.1
N II x3	5001.13	0.0	1.28	-15.5	
N II	5495.67	4.48	2.9	-17.1	0.7
N II	5676.02	7.1	5.4	-15.6	0.7
N II	5679.56	0.0	2.4	-17	
N III	3934.50	1.9	1.7	-20.5	
N III	3998.63	8.2	3.2	-15.3	0.4
N III	4003.58	10.5	1.1	-16.3	0.3
N III	4195.76	0.1	2.2	-19.8	0.2
N III	4200.10	4.5	3.0	-14.6	0.3
N III	4215.77	0.0	3.0	-17.6	224.9
N III	4510.91	0.0	0.5	-18.5	
N III	4514.86	0.0	1.2	-16.4	0.3
N III	4518.14	0.45	5.93	-16.2	0.2
N III	4523.56	10.7	3.0	-15.5	0.9
N III	4867.15	5.59	1.83	-18	
N III	4884.14	4.9	5.0	-16.9	0.4
N III	5320.82	4.8	5.9	-18.5	
N IV	4057.76	6.2	2.2	-16.1	419.9
Si III	3806.54	3.8	5.9	-18.1	1.2
Si III	4552.62	5.8	2.5	-17	
Si IV	4212.41	10.1	2.3	-15.0	0.3
Si IV	7047.94	5.0	2.0	-17	

D.2 IUE

Ion	λ_s (Å)	v_{rot} (km/s)	Δv_{rot} (km/s)	v_{rad} (km/s)	Δv_{rad} (km/s)
C III x6	1175.71	29	2	-25	
C III	1247.383	0		-25	
C IV x2	1548.202	3.6		-23	
N III	1324.396	11.9	5.3	-33	
N III x5	1387.371	11.9	5.6	-28	
N III x4	1729.945	0		-23	
N III x2	1751.218	0.0	3.1	-20	
N III x2	1885.22	5.7	7.4	-25	
N IV	1718.55	3.2	5.8	-16	
Si III	1298.96	0		-24	
Si IV	1393.755	0		-22	
Si IV	1402.770	0		-24	
S IV	1296.659	3.2	3.9	-24	
S IV	1629.143	0.0	3.5	-24	
S V	1501.760	0.0	16.5	-19	

D.3 GHRS

Ion	λ_s (Å)	v_{rot} (km/s)	Δv_{rot} (km/s)	v_{rad} (km/s)	Δv_{rad} (km/s)
C III	1247.383	0		-15	
C IV x2	1548.202	0		-15	
N III	1324.396	0		-11	
N III x5	1387.371	13.0	3.0	-14	
N III x5	1729.945	5.0	2.8	-11	
N IV	1718.55	0		-14	
N V	1238.821	14.0	3.4	-15.2	1.3
N V	1242.804	15.6	4.2	-16.5	1.2
Si III	1298.96	0		-10	
Si IV	1393.755	0		-12	
Si IV	1402.770	0		-12	
S IV	1296.659	13.7	2.7	-5	
S IV	1629.143	0.0	2.3	-13	

Acknowledgments

Working on my bachelor thesis at the observatory has been a great time. I would like to thank my supervisors Ulrich Heber and Marilyn Latour for giving me the opportunity to work on an interesting topic. They were always open for questions and were helping me a lot throughout the entire project, from the first week to the intensive proofreading in the last days. Especially Marilyn helped me a lot in every part of my work, investing time to answer many spontaneous questions and providing valuable guidance. Amongst many other things, she introduced me to the `TLUSTY/SYNSPEC` codes, helped me learn Python to make most of the figures, and provided me with the very nice ionization stratification plots. I also enjoyed the extremely helpful discussions about my results and hot subdwarfs in general.

I am very grateful to Uli Heber for giving me the chance to attend and present a poster about this thesis at the Eighth Meeting on Hot Subdwarf Stars in Cracow, where I not only learned a lot about many aspects of the broad "hot subdwarf" area, but had a great time in general. Taking part in the diverse excursions organized by the local conference committee and exploring the city, especially in the last days with Marilyn, Simon Kreuzer and Eva Ziegerer was a fun time.

Many thanks to my colleges from the stellar astronomy team for being such a nice and helpful bunch of people. Whenever I had questions and problems concerning `SPAS`, I could ask Markus Schindewolf, who introduced me to the program to begin with. Especially David Schneider, but also Andreas Irrgang provided some valuable programming and `ISIS` support and were always ready to help. Thanks to Eva Ziegerer for some very helpful last-minute proofreading and comments.

The atmosphere at the observatory was great also apart from work, for example going to the cafeteria, or playing tennis with Manuel Castro.

Finally, I would like to thank my parents for their continuous and generous support over many years that allowed me to even begin this thesis in the first place.

Erklärung

Ich versichere, dass ich meine Bachelorarbeit ohne Hilfe Dritter und ohne Benutzung anderer als der angegebenen Quellen und Hilfsmittel angefertigt habe und die aus benutzten Quellen wörtlich oder inhaltlich entnommenen Stellen als solche kenntlich gemacht habe. Diese Arbeit hat in gleicher oder ähnlicher Form noch keiner Prüfungsbehörde vorgelegen.

Bamberg, den _____ _____

Matti Dorsch